SAPIENZA
UNIVERSITÀ DI ROMA

Transport and manipulation of laser driven proton beams for diagnostics and applications

Thesis for obtaining the degree of Philosophiae Doctor (Ph.D.)
University of Rome "La Sapienza"

Scientific advisors:
Prof. Mauro Migliorati
Prof. Sargis Ter-Avetisyan

Evaluators:
Prof. Subhendu Kahaly
Prof. Luca Volpe

Ph.D. candidate
Antonia Morabito

Academic Year 2020/2021

List of Publications

This thesis work is based on the following publications:

I. S. N. Chen, M. Gauthier, M. Bazalova-Carter, S. Bolanos, S. Glenzer, R. Riquier, G. Revet, P. Antici, **A. Morabito**, A. Propp, M. Starodubtsev and J. Fuchs, Absolute dosimetric characterization of Gafchromic EBT3 and HDv2 films using commercial flat-bed scanners and evaluation of the scanner response function variability, Review of Scientific Instruments 87, 073301 (2016)-doi: 10.1063/1.4954921;

II. S. Vallières, **A. Morabito**, S. Veltri, M. Scisciò, M. Barberio, P Antici, Laser-driven proton acceleration with nanostructured targets, SPIE Optics & Optoelectronics, 1024009-6 (2017)-doi: 10.1117/12.2265913;

III. M. Barberio, M. Scisciò, S. Vallières, S. Veltri, **A. Morabito**, P. Antici, Laser-Generated Proton Beams for High-Precision Ultra-Fast Crystal Synthesis, Sci. Rep (2017)-doi: 10.1038/s41598-017-12782-w;

IV. **A. Morabito**, M. Scisciò, Veltri S., M. Barberio, M. Migliorati, P. Antici, Design and optimization of a laser-PIXE beamline for material science applications, Laser and particle beams-1–10 (2019)-doi: 10.1017/S0263034619000600;

V. **A. Morabito**, K.Nelissen, M. Migliorati, S. Ter-Avetisyan, Theoretical study of a new spectrometer design for laser driven ion acceleration diagnostic (manuscript under preparation) (2021).

Attendance at International Conferences and Schools

During my doctoral studies, I have presented this thesis work at the following summer schools and international conferences:

- **A. Morabito**, "Transport and manipulation of laser driven proton beams for application and diagnostics", *talk presentation*, University of Szeged, Hungary, Oct 2019
- **A. Morabito** et. al., "Novel spectrometer design for laser driven ion acceleration diagnostic", *talk presentation*, ELI-ALPS Science Day hosted by ELI-ALPS, Szeged, Hungary, Oct 2019;
- **A. Morabito** et. al., "Novel spectrometer design for laser driven ion acceleration diagnostic", *poster presentation*, European Advanced Accelerator Conference 2019, Elba, Italy, Sept 2019;
- **A. Morabito** et. al., "Design and optimization of a laser-PIXE beamline for material science applications", *poster presentation*, ATTO 2019 hosted by University of Szeged Congress Centre, Szeged, Hungary, Jul 2019;
- **A. Morabito** et. al., "Optimization of a dedicated laser driven proton hybrid beamline for cultural heritage applications", *talk presentation*, ELI-ALPS Science Day hosted by ELI-ALPS, Szeged, Hungary, Mar 2019;
- **A. Morabito** et. al., " Design and optimization of a dedicated laser driven proton hybrid beamline for cultural heritage applications", *talk presentation*, European Conference on Laser Interaction with Matter 2018, Rethymno, Greece, Oct 2018;
- **A. Morabito** et. al., "Dedicated laser driven proton hybrid beamline for cultural heritage applications", *poster presentation*, First summer

school Laser Plasma Summer School Diagnostics techniques for laser-plasma experiments@HRR hosted by CLPU, Salamanca, Spain, Sept 2018;

- **A. Morabito** et. al., "Laser Accelerated Proton Beams as Diagnostics for Cultural Heritage", *talk presentation*, ELI-ALPS Science Day hosted by ELI-ALPS, Szeged, Hungary, Mar 2018;

- **A. Morabito** et. al., "Absolute dosimetric characterization of Gaf. EBT3 and HDv2 films using commercial flat-bed scanners and evaluation of the scanner response function variability", *poster presentation*, The International Science@Free Electron Lasers FELs Conference2016, Trieste, Italy, Sept 2016;

- **A. Morabito** et. al., "Laser-Driven Proton Beam Ablation for Micro-Crystals Synthesis", *poster presentation*, NIF and JLF User Group Meeting 2016, Livermore (California), 31 Jan 2016 - 3 Feb 2016.

Contents

List of Figures

List of Tables

Introduction: scientific context and state of the art

The curiosity to explore and investigate nature is the driving force for development both in science and in technology. In particular, the particle accelerator field has attracted, since the early twentieth century, a great interest for both scientists and engineers.
The need to accelerate particles (ions, electrons) to higher and higher energies, has lead to a progressive evolution and increase in dimensions of particle accelerators, such as the Large Hadron Collider (LHC) [60, 211] (see figure 1).

Figure 1: Large Hadron Collider (LHC), figure reported from [211].

The Large Hadron Collider (LHC) is considered, nowadays, one of the world's most advanced and most powerful synchrotron. It is located in Geneva, at the border between France and Switzerland and it is an underground 27 kilometer ring of superconductive magnets with a huge number of accelerating structures to boost and accelerate the energy of the protons up to 7 TeV and

reach a center of mass energy of 14 TeV.
Over the last decades, new possibilities and new scenarios in terms of particle acceleration have been opened up by the advent of high intense ($I > 10^{18} W/cm^2$) laser systems. High intense laser pulses are capable of generating a high intense electric field in the plasma of the order of TV/m, about three orders of magnitude higher than typical values of RF-based conventional accelerators within short distances (few μm).
Furthermore, in conventional acceleration, the particle sources, the accelerating structures and the focusing elements have a key role. In laser driven particle acceleration [113, 50], similarly, the laser parameters (energy, power, pulse duration, polarisation, contrast), the target features (shape [185], structures [124, 14], thickness[66], material[183]) and the type of mechanisms generated by their interaction are the fundamental elements.
This thesis work deals with laser driven proton sources. At current, laser driven protons have reached experimentally maximum energies of 100 MeV. These compact and energetic proton sources have boosted a strong interest both in diagnostics and applications.
The particle acceleration from laser-plasma interactions is a very complex phenomenon due to the inherently involved non-linear laser plasma interactions. Therefore, suitable instrumentation for the diagnostics of laser accelerated proton beams is vital for increasing the knowledge of the acceleration mechanism itself. As such, the development and the improvement of charge particle diagnostics are essential.
Laser proton beams have unique characteristics, such as (1) a high charge (10^{13} particles/shot), (2) a short bunch duration (ps at the source), (3) high laminarity and (4) extreme broad energy spectrum. Proton sources have the Bragg peak, i.e they deposit most of their energy at the end of their path during their travel inside matter. These features have stimulated interest in a wide variety of applications, in fields like bio-medicine (tumor treatment, PET, radiography), warm dense matter, hybrid acceleration schemes, material science, cultural heritage (CH), etc.
However, laser driven proton beam parameters, such as the large energy spread ($\sim$ 100 %) and the high divergence can obstacle their use for applications. Hence, coupling them with conventional accelerator devices, such as dipoles, quadrupoles, etc has considered a valuable option for tailoring (shaping, transporting, selection, focusing) these beams for the obtainment of reliable and stable sources for applications.
The work presented in this thesis is developed within the current state of the art, both in terms of laser driven proton diagnostics and applications. The properties of these proton sources are the input parameters for the design of a dedicated transport beamline for applications, as well as the final

targets towards the improvement of laser-driven proton diagnostics, which allow a better knowledge of the complexity of the laser-plasma interactions, that drives laser generated proton acceleration.

Object of the thesis and outline

The aim of this doctoral thesis is to study the transport and the manipulation of laser driven proton beams for both diagnostics and applications.
This work is mainly separated into two parts: (1) a theoretical study of a new spectrometer for laser ion diagnostics and (2) a detailed study of a laser Particle Induced X-Ray Emission (PIXE) beamline for material science applications.
It also includes part of the experimental results related to my participation in August 2016 in the TITAN experimental campaign in Livermore, California, and my participation in the first trimester of 2020 in the experimental campaign at Extreme Light infrastructure Attosecond Light Pulse Source (ELI-ALPS) research center in Szeged, Hungary.
A better knowledge of the source of the laser-generated protons is translated in being able to "control" and increase the understanding of the evolution of the acceleration process at the beginning, whereas developing a customized transport beamline is translated in increasing the "control" of the final proton parameters required for a specific application.
The thesis is structured as follows:

- **Chapter 1** introduces the theoretical background of high-intensity laser-plasma interactions, from ionization processes, single-electron dynamics, laser propagation and absorption in plasmas to the main concepts of laser-driven proton acceleration. We focus our attention on the target normal sheath acceleration (TNSA) mechanism. We also describe the main TNSA proton beams properties, core of this thesis;

- **Chapter 2** describes laser driven ion beam diagnostics. We compare several detection (diagnostics) systems, emphasizing similarities and differences in order to portray the current state of the art in this field. In this chapter, the details of my contribution for papers **I** and **II** are reported;

- **Chapter 3** deals with the first experimental observation of low energy (few MeV) laser driven ion beams at ELI-ALPS research center in Szeged, Hungary. They have been accelerated, using in a single shot

mode, the SYLOS Experimental Alignment (SEA) laser (multi-TW-ultra-short milli-joule laser system) hosted by the ELI-ALPS facility. We describe the experimental setup and part of the data analysis results, which is a work in progress;

- **Chapter 4** discusses the theoretical study of a novel type of spectrometer, that aims at investigating the possibility of enhancing the detectable proton and ion energy, compared to existing spectrometer combinations. We describe in detail the methodology and the different schemes that have been implemented. We study the replacement of the constant dipole field of a conventional Thomson parabola spectrometer (TPS) with different not homogeneous field profiles. By not homogeneous field we indicate quadrupoles, octupoles and high order magnetic elements. We consider also the contribution of laser generated sources that include proton and carbon ions. The obtained results are the subject of paper **V** (manuscript under preparation). We show a possible scaling law that compares the different magnetic orders vs the minimum detectable proton energy. In the end, we summarize and emphasize the limits and advantages of the proposed spectrometer designs;

- **Chapter 5** provides an introduction of different proposals for manipulating the laser-generated proton beams downstream the laser-plasma interaction point using conventional accelerator devices, implementing the so-called hybrid beamlines or post acceleration schemes. Magnetic passive chicanes that act as energy selectors (ES), RF cavities, quadrupoles, etc have been coupled with laser-driven proton sources for adapting and customizing them for a specific application;

- **Chapter 6** deals with the detailed numerical study of the design of a compact and versatile laser-driven proton hybrid beamline, implementable for different types of applications in material science, e.g. the one described in paper **III**. They include also the Particle Induced X-ray Emission (PIXE). PIXE is a sophisticated nuclear technique that allows retrieving chemical and quantitative information about the elements that are present on cultural heritage (CH) samples. We describe in detail the context of the study and the numerical tools that have been used in order to compare, in terms of proton features, the performance of a laser-driven hybrid beamline with the typical parameters of conventional facilities for PIXE spectroscopy. The proposed laser driven proton hybrid beamline schemes are composed of an energy selector (ES), that allows selecting proton energies of 1, 3, 5 MeV (typical proton energies used in conventional PIXE), reaching a final energy spread

of ~ 10 %. They also include the addition of the permanent quadrupole magnets (PQMs) that follow the ES, with the aim of obtaining feasibility in final transverse spot sizes, i.e beam vertical dimension from less than 1 mm up to cm scale. The obtained results are subject of paper **IV** and provide useful guidelines for designing and optimizing the elements of a laser-PIXE proton beamline for improving and further investigating the use of laser-generated proton sources for applications.

Finally, we summarize the achieved results, giving an outlook towards the future prospects of this work.

Chapter 1

Proton acceleration driven by laser-plasma interaction

This chapter aims at providing an overview of the steps that characterize the acceleration schemes, that are used in laser driven proton acceleration (LDPA) [113, 176]. We, first, briefly report the main laser driven proton experiments [18, 45, 73, 107, 119] that represent the milestones toward the understanding and the use of these compact and high energetic laser ion (proton) sources [18, 45, 73, 107, 119].
Then, we summarize the fundamentals of high intensity short pulse laser-matter interactions and present basic concepts associated to laser-driven proton acceleration.
Several schemes have been studied, including the target normal sheath acceleration (TNSA) [188, 216] (see section 1.3.1), radiation pressure acceleration (RPA) [115, 153, 167, 59], breakout afterburner [219], collisionless shockwave acceleration[62, 62, 82, 186] and magnetic vortex acceleration (MVA)[29, 143, 185].
Theoretical and numerical investigations suggest also that, for the next generation of lasers with high intensities ($I > 10^{22} W/cm^2$), other alternative hybrid acceleration mechanisms will allow potentially achieving ion energies in the GeV range [58, 162]. Here, we focus our attention on the TNSA, which is relevant for this thesis work.
At the end of the chapter, in section 1.4 we list and describe the TNSA laser driven proton beams features. These properties are important, both for diagnostics (see chapter 2 and 4) and applications (see chapter 6).

1.1 Laser driven proton acceleration

1.1.1 History and state of the art

Starting from the realization of the laser in 1960 [118], great developments [193, 140] have been done in laser technology and allowed studies at ever-increasing intensities.
For a long time, the main limit in terms of focused laser intensity was given by the damage threshold of the optical components of laser systems. This bottleneck was overcome with the breakthrough invention of the key technique of [191] Chirped Pulse Amplification (CPA) (1985) by professors Gerard Mourou and Donna Strickland (Physics Nobel prize 2018). After that, there was an unstoppable progress in high power laser technology [51].
As it is shown in the figure 1.1, this technique consists mainly of three steps. The initial short pulse is first stretched in time, e.g. by the use of pair of gratings (see figure 1.1) in order to be broadened and lower the peak power, then it is amplified, and then recompressed. For further details regarding CPA, we refer to [72, 105, 191].

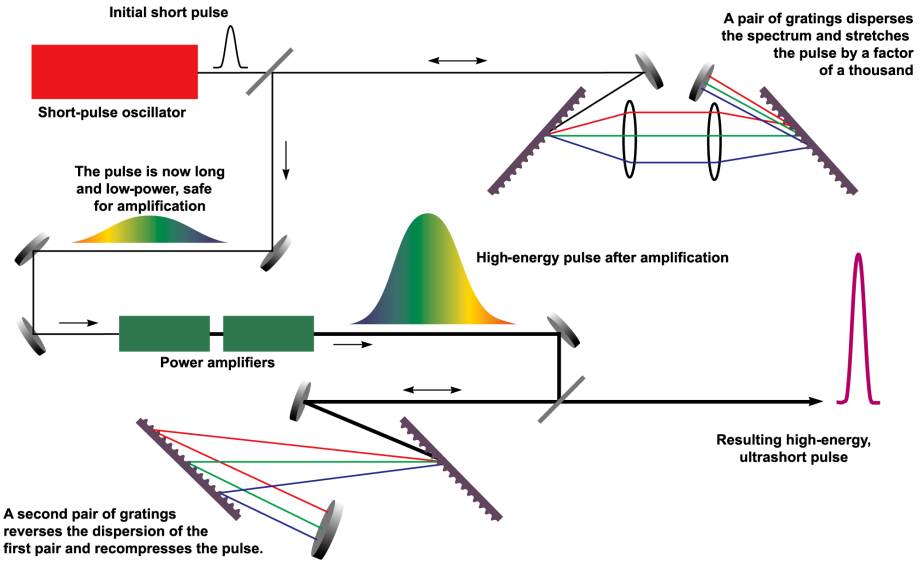

Figure 1.1: The three main steps of Chirped Pulse Amplification (CPA). The figure comes from [215].

This technique enables the possibility to deliver energies ranging from mJ up kJ order while having a pulse duration from picosecond (10^{-12} s) to femtosecond scale (10^{-15} s) and reach peak powers of several TW (10^{12}) up to PW (10^{15}) scale. As it is known, an intensity of 10^{24} W/cm^2 [72] is required for

the direct acceleration of ions by the laser field. Thus, the currently achievable laser intensities (10^{22} W/cm^2) [51] allow the generation of laser driven ions as a consequence of the laser energy transfer to the electrons and then to the ions (see section 1.2.5).
Guverich et al. [80, 79] have investigated the problem of the expansion of the plasma in vacuum and have derived first scaling laws for accelerated ions spectra of different masses and charges. Gitomer et al. [73] were among the firsts, that collected the data related to the energetic laser driven ion sources for a wide range of laser wavelengths, energies and pulse lengths in order to better understand the acceleration of the particles driven by high intensity laser-plasma interactions.
Gitomer et al. included also the experimental evidence of laser generated proton (light ions) beams, observed between the late 1970s and early 1980s, at Los Alamos National Laboratory (LANL) in the USA [18].
During these experiments performed at the Gemini CO_2 laser facility, long pulse (< 1 ns) and not so high intensity (10^{15} W/cm^2) laser pulses were used for the interaction with targets consisted of carbon, titanium and tantalum wire (250 μm) and polyethylene (CH_2) films.
They [18] used as diagnostics a Thomson parabola (TP) coupled with cellulose nitrate film particle detectors. Although the features of the obtained ions, e.g maximum proton energy was of the order of few hundreds of keV with a maximum value of $\sim$ 0.56 MeV, were not so remarkable, these results encouraged studies about the proportion between the temperature of the "hot electrons" and the maximum ion/proton energy reachable driven by laser-plasma interactions, as well as studies about the influence of the presence of hydrogen contamination on the carbon ion acceleration[73, 18].
In 2000, almost simultaneously three different papers were published respectively by Clark[45], Maksimchuck[119]and Krushelnick [107], reporting new evidences of laser generated proton beams, using similar types of targets and laser parameters.
The protons beams detected in these experiments are considered the first ones having beam-like properties because of the high numbers of particles, short pulse and multi-MeV energies observed.
Clark [45] et al. used the VULCAN laser at Rutherford Appleton Laboratory (UK), that reached intensities of $5\cdot 10^{19}$ W $\cdot\, cm^{-2}$ on 125 μm thick aluminum target.
A "sandwich" of several pieces of RadioChromic films (RCF) and CR-39 plastic detectors have been used as diagnostics. The ion signal on the CR-39 exhibited a ring pattern with decreasing diameter for increasing ion energy up to 17.6 MeV. Hence, they assumed that the relationship between the energy of the emitted protons and the angle at which they are emitted is

caused by large azimuthal magnetic fields (line-averaged field of few tens of MG have been observed) [45]) within the solid target material that develops and persists during the few picoseconds after the laser pulse, i.e the source of the energetic protons is originated from the front surface of the target and then they are bent by large magnetic fields which exist inside the target.
Krushelnick [107] et al., using similar laser and target parameters, managed to obtain proton energies of 30 MeV at the VULCAN laser facility (laser energy $\sim$ 50 J at a wavelength of 1.053 μm, laser pulse between 0.9-1.2 ps). They observed up to 10^{12} protons ($>$ 2 MeV) driven by the interaction with aluminum foil targets of a thickness of 125 μm, implementing as detectors CR-39-RCF stacks. They deduced, similarly to Clark et al. [45], according to nuclear activation and track detectors measurements, that the protons are originated from the front surface of the target surface, are bent by large magnetic fields that exist in the plasma, which are generated by a laser-produced beam of fast electrons.
Maksimchuck [119] et al. focused a 10 TW laser (4J, 400 fs, $\lambda \sim 1.054$ μm) with intensity $5{\cdot}10^{19}$ W$\cdot$ cm^{-2}, on aluminum targets of 3 to 25 μm, observing proton beams of about 1.5 MeV. To compare the ion emission in the forward (through the thin film) and backward (through the laser), two CR-39 detectors with sets of Mylar filters, were placed both in front and in the back of the target. The high energy proton emission recorded on the CR-39 at the rear back of the target, made them consider that the protons, which appears from impurities on the front side of the target, are accelerated over a region extending into the target and exit out the backside in a direction normal to the target surface.
Laser accelerated proton beams of significantly better properties were observed in experiments [188] in Lawrence Livermore National Laboratory's (LLNL) Nova Petawatt laser system in Livermore, California (USA). The petawatt and picosecond laser system of $I \sim 3 \cdot 10^{20}$ W/cm^2 irradiated targets such as gold, Ti, aluminum and CH targets.
The detection system of this experiment [188], included only RCFs. Later on, a magnetic spectrometer (see chapter 2) was added in order to distinguish electrons and protons. Furthermore, direct evidence that the beam is protons rather than ions species was obtained from the observation of nuclear reactions. In the figure 1.2 extracted from [188], autoradiographic imagines of the V^{48} activation in the Ti foils shows a one to one correspondence to the RCFs images recorded on the same shot, confirming that RCFs were irradiated by the proton beam. A Boltzmann-like spectrum has been measured and a proton cut-off energy of $\sim$ 58 MeV has been reached[188]. They interpreted the generation of the proton beam as a planar electrostatic acceleration by a dynamic Debye sheath formed at the rear target surface by hot electrons.

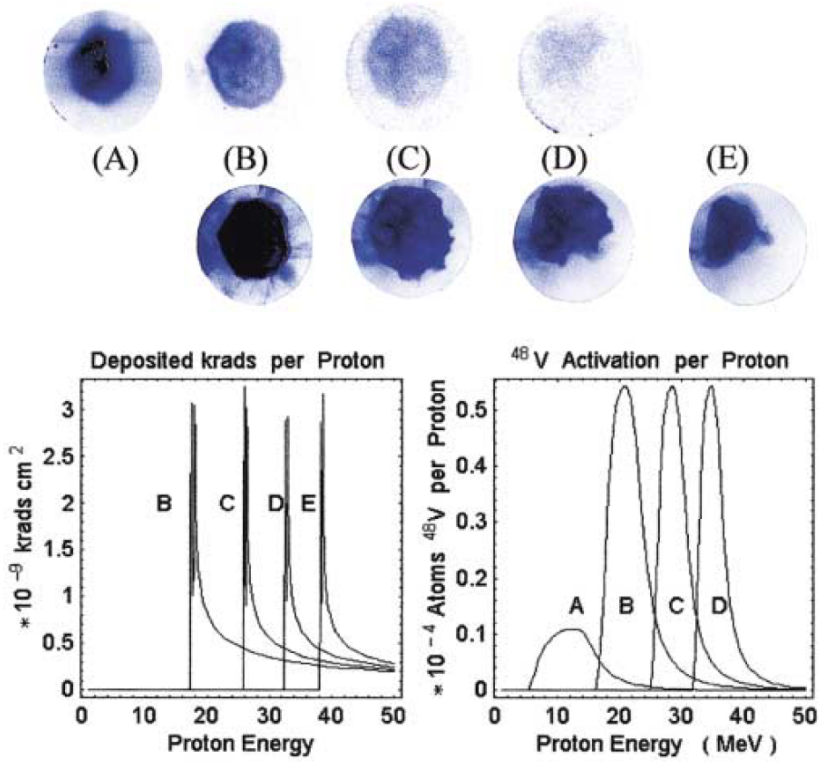

Figure 1.2: RCF images recorded from the interaction of a normal incidence 445 J shot on 100 μm CH from the Ti nuclear activation: Ti foil autoradiographs are reported on the top row, while RCF images are reported in the middle row. The plots show the comparison between Monte Carlo modeling (bottom left) of the RCF detector response in krads cm^2 per proton normally incident in the film layers and the nuclear activation response (bottom right) of the Ti layers to protons through the successive filter layers of the detector. The figure is extracted from [188].

Murakami [141] et al. irradiated with the 50 TW GEKKO MII laser (25 J, $\lambda \sim 1.054$ μm, 0.45 ps, peak intensity of $5 \cdot 10^{18}$ W $\cdot$ cm^{-2}) plastic foils with thickness of 5-10 μm. The obtained proton bunches had energies between 8 and 10 MeV and the experiment results suggested that the energetic protons are dragged away from the rear surface, where the hot electron formed a virtual cathode. Thus, they deduced similar conclusions as [188] (rear back proton acceleration) mostly due to the ring structure observed on the CR-39 film stacks preceded by tantalum filters.
These experiments[45, 119, 141, 188, 107] opened up a debate regarding the origin of the laser-driven proton sources. Allen et al. [5] have reported the

observation of laser driven proton beams from the back and the front side of the target. They irradiated Au foils with a 100-TW, 100 fs laser at intensities greater than 10^{20} W $\cdot$ cm^{-2}, producing proton beams with maximum energy greater than 9 MeV and a number of protons of $\sim 10^{11}$. They removed the contaminants on the targets by means of an Ar-ion sputter gun. They repeated the experiment, using different targets: Au foil, Au foil with the removal of contaminants on the front surface (laser-interaction side) and Au foil with the removal of contaminants on the back surface. The detected proton beams, measured with RCF film stacks, have been compared. No effects have been observed for the removal from the front surface, whereas the back contaminants removals reduced the total yield of 1% compared to the case of Au foil without any removing contamination. Thus, their results were consistent with back-surface acceleration mechanisms[5].
Later on, Fuch et. al [67] confirmed the same experimental results of [5]. They presented the first and quantitative comparison between Front Surface Acceleration (FSA) and Rear Surface Acceleration (RSA) proton beams under identical laser conditions. The obtained spectra, using RCF stacks and nuclear activation techniques, showed that the quality of the ion beams from the back dominates compared to the front surface. The RSA produces higher energy particles with smaller divergence, higher efficiency compared to FSA. Furthermore, Fuchs et al. explained that the ring patterns observed by Clark et at. [45] (FSA) and Murakami et al [141] (RSA) arose most from saturation effects and artificial response in the CR-39 at high proton fluences and it is not a signature of high-energy protons. Therefore, the differences observed were misinterpreted [67, 9].
Despite the numerous efforts in optimizing target and laser conditions the maximum achievable laser driven proton energy was 58 MeV for almost a decade [188, 50]. In 2016, Wagner et al, [209] reached a newly maximum proton energy value of $\sim$ 85 MeV. In this case, laser driven proton acceleration has been investigated with micrometer and sub-micrometer thick plastic targets and relatively long ($\sim$ 0.5 ps) laser pulse with high energy ($\sim$ 200 J) obtained from a combined Ti:sapphire Nd:glass laser system, the Petawatt High Energy Laser for heavy Ion eXperiments (PHELIX) [209] in Darmstadt, Germany. These laser pulses were focused on the target surface under different angles of incidence from 0° to 30° (tilted target as it was done in ref. [67]) using an f/1.7 focusing parabola. The diagnostics were RCFs in a stack configuration. Furthermore, copper and nickel foils have been used as intermediate layers in the stack for nuclear activation measurements, as reported in [78]. The direction of the accelerated beam allows discriminating the different acceleration mechanisms. In this case, the center of the imprint of the beam on the RCF stacks corresponded to the target normal

direction, which is an indication of the TNSA mechanism. The maximum proton energy observed was 50% more than before [188]. They ascribed this improvement to the reduction of the shot-shot aberrations of the laser beam that led to a higher actual intensity. Their results, hence, are coherent with the previous findings[188].
Nowadays, the maximum proton energy experimentally observed is near 100 MeV. This value has been detected with RCF stacks and it is theoretically associated to a new hybrid laser driven transparency-enhanced hybrid acceleration scheme, as reported in [90].
In conclusion, the initial misunderstanding regarding the origin of laser proton source acceleration has been gradually solved with simultaneous front-back detection experiments[5, 67].
Numerous scaling laws have established consolidated dependencies between laser intensity, laser energy, laser pulse duration and maximum achievable proton energy [25, 114, 113] (see section 1.4).
At current, the common directions for improvements in LDPA are target engineering optimization, e.g. nano-structured targets, that will be briefly discussed in section 1.3.2, ultra thin foils [159], the use of mass-limited targets (target with transverse dimension that is of the same order of the laser focus (10-20 μm)) [184], cryogenic hydrogen micro-jets [183, 104], nanowires[161], low density foams[155, 161, 21], the enhancement in laser temporal contrast and intensity [209] and the investigation of "new" acceleration schemes [90, 128, 219, 153].

1.2 Basic concepts associated to laser driven ion acceleration

The physics of ultra-intense laser-matter interactions is a very complex topic, that has been widely studied. In this section, we aim at providing a brief summary of the fundamentals of high intensity short pulse laser-matter interactions, relevant for laser-driven proton acceleration.
We refer for a more complete and exhaustive description of these topics, to recent reviews and books reported in [72, 105, 38, 75, 50].

1.2.1 Ionization of matter

The first step related to LDPA is the ionization. The ionization physics includes multiple processes, such as multi-photo ionization [72]. When a laser pulse with sufficiently high intensity interacts with a material it ionizes the atoms and the molecules, creating a global quasi-neutral plasma that consists

of positive ions and electrons. A plasma is a state of matter in which a major fraction of the atoms has been ionized, it is globally neutral and it can be subjected to collective effects (see section 1.2.4).
The needed laser intensity depends on how strong is the bound of the electrons to the atoms and it strongly depends on the target material. However, with the high intensity laser used in LDPA, the ionization process that mainly occurs is named barrier suppression [72]. The Coulomb potential barrier of the atom or ion that bounds the electrons is suppressed by the strong laser electric field.
The laser intensity that allows this suppression is the appearance intensity [72]:

$$I_{app} = \frac{c\epsilon_0^3 \pi^2 E_{ion}^4}{2Z^2 e^6} \tag{1.1}$$

where c is the speed of light, ϵ_0 is the permittivity of free space, E_{ion} is the ionization energy of the atom/ion, e is the charge of the electron and Z is the charge state of the created ion.
In the majority of the LDPA experiments, the main laser pulse is preceded by pre-pulses, and can have a pedestal, a radiation coming from the amplified spontaneous emission (ASE) of the active mediums or by the leakages in the CPA chain. The ratio between the pre and main pulse intensity is the contrast ratio and its value is usually of the order of 10^{-6}. Therefore, the main laser pulse is preceded by a pedestal, that can be sufficient to ionize the target and create the plasma.

1.2.2 A single electron in an electromagnetic wave

Before describing the main parameters that characterize the laser-plasma interaction, it is useful to have an insight into the motion of a single electron in a laser field.
The dimensionless laser amplitude a_0, which is the ratio of electron quiver velocity to the speed of light, allows to quantify when the laser is considered to be relativistically intense and it is defined as[72]:

$$a_0 = \frac{v_{osc}}{c} = \frac{eE_L}{m_e c \omega_L} \tag{1.2}$$

where E_L is the peak electric field and ω_L is the frequency of the laser.
The dimensionless parameter $a_0 = \sqrt{I\lambda^2/1.37 \times 10^{18}}$ where I is expressed in W cm^{-2} units and λ is expressed in μm. Thus, it can be seen that the relativistic regime is reached when $a_0 \sim 1$, e.g I $\sim 1.38 \times 10^{18}\ Wcm^{-2}$ and $\lambda \sim 1\ \mu$m.

The motion of a single electron, in an electromagnetic (EM) field (e.g the laser field), is subjected to the Lorentz Force:

$$\frac{d\vec{p}}{dt} = \frac{d(\gamma m\vec{v})}{dt} = -e(\vec{E} + \vec{v} \times \vec{B}) \tag{1.3}$$

where e is the charge of the electron, $\vec{E}$ is the electric field, $\vec{v}$ is the velocity of the particle, $\vec{B}$ is the magnetic field, $\gamma = (1+ \mathrm{p}^2/\mathrm{m}^2\mathrm{c}^2)^{1/2}$ is the Lorentz factor.
We can consider as an example for describing it, an elliptically polarized plane wave, that travels in the positive x-direction. In this case, the vector potential has only y and z contributions that depend on the phase of the wave, the dimensionless amplitude a_0 and the polarization[72].
According to the energy and momentum conservation [72], we can derive the relationship between the parallel p_x and perpendicular momenta $p_\perp$, that is $p_x = (1 - \alpha^2 + p_\perp^2)/2\ \alpha$, where $\alpha = \gamma$ -p_x is a constant of motion.
In the laboratory frame, the electron is initially at rest before the EM wave (laser pulse) arrives and the constant α is equal to 1[72]. Thus, the electron lab-frame trajectories for an EM field propagating along x and linearly polarized along the y axis are:

$$x = \frac{a_0^2}{4}(\phi + \frac{1}{2}\sin(2\phi)) \tag{1.4}$$

$$y = a_0 \sin(\phi) \tag{1.5}$$

$$z = 0 \tag{1.6}$$

where $\phi = k_L x - \omega_L t$ [204]. From these solutions, we can see that the longitudinal motion in x (the laser propagation direction), caused by the $\vec{v} \times \vec{B}$ has a linear term in time (see eq. 1.4) in addition to the oscillatory term, which scales quadratically with a_0, whereas the transverse motion in y is only oscillatory and linearly proportional to a_0 [96].
In the lab rest frame, as it is shown in figure 1.3 (A), the electrons oscillate due to the electric field of the laser. They have an oscillation frequency equal to that of the laser field and moves in the laser propagation direction. In the presence of the EM wave, the electron starts immediately to drift with an average momentum $p_D = a_0^2/4$ and correspondent velocity [72]:

$$\frac{v_{drift}}{c} = \frac{a_0^2}{4 + a_0^2} \tag{1.7}$$

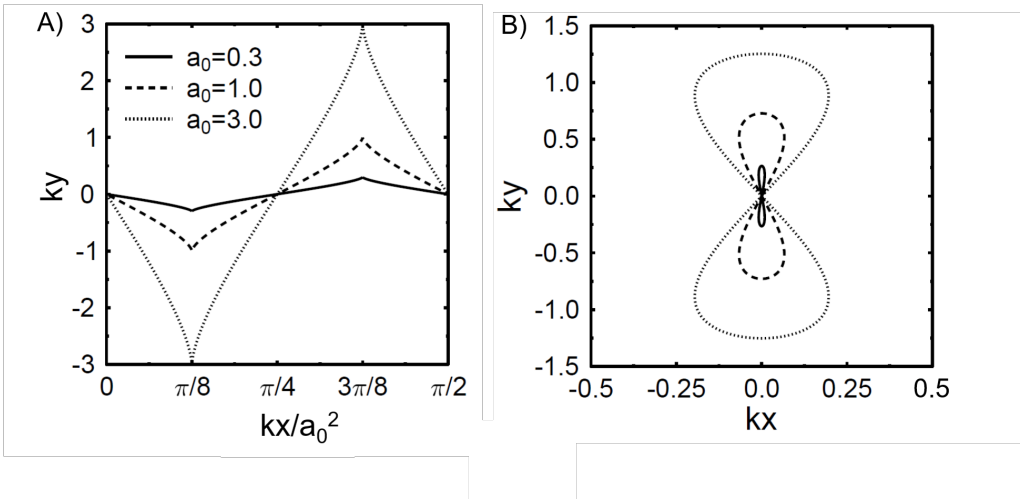

Figure 1.3: For laser wavelength $\lambda = 1$ μm, the three values of a_0 correspond approximately to intensities of 10^{17}, 10^{18}, 10^{19} W/cm^2 respectively. (A) Electron trajectories for linearly polarized EM plane wave in the x-direction in the lab rest frame; (B) characteristic "8 shaped" electron trajectories in the average rest frame. Figures reported from [72].

The drift depends on the normalized amplitude a_0. For the average rest frame, this movement is translated in the characteristic "8 shaped" trajectory in the x-y plane, as illustrated in figure 1.3 (B). This means that, for small a_0, the motion is initially oscillatory, while for large a_0, it acquires a longitudinal component as the field grows [157, 72].
However, as reported in [72], the electron energy, after the passage of the EM field (laser) is the same as before the EM field arrival, i.e the free electron cannot gain energy from the laser. This happens only in the case of a single electron in vacuum, while in a more realistic case scenario, the spatial profile of the laser pulse needs to be taken into account. Therefore, we will introduce the ponderomotive force.

1.2.3 Ponderomotive force

A real laser pulse cannot be described with a plane wave because it is finite in space and time and it has a fast varying intensity envelope i.e a strong radial intensity gradient.
As illustrated in figure 1.4, we consider as a starting point a not-relativistic electron positioned on the laser axis (x direction), where the laser field has the strongest value. During one half of the laser field oscillation, it experiences a strong transverse force, that pushes it away from the original position (laser

axis), as well as a drift due to $v \times B$ component.
In a plane wave with no spatial profile, the electron would return to its initial position, with no energy gain (Theorem of Woodward [72]). In the case of the laser pulse, instead, the restoring force that the electron experiences due to the spatial intensity beam profile, in the second half of the laser field oscillation, is weaker compared to the first half. Hence, the electron does not return to the initial point at the end of the laser cycle and as result, it has an energy gain. The force acting on the electron and average over the laser period moves the electron towards a region of lower laser intensity. This force is named the ponderomotive force.

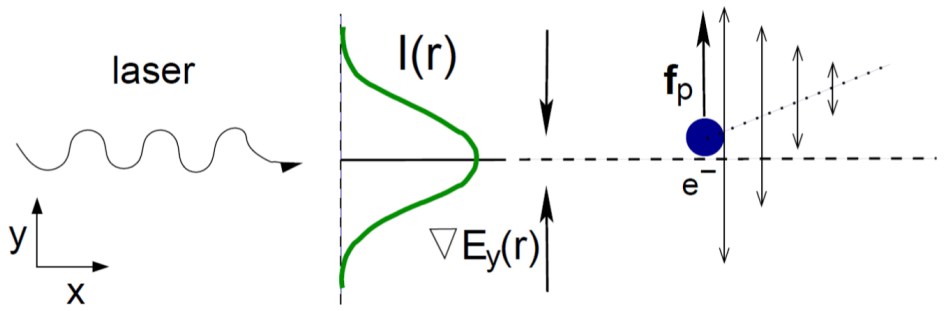

Figure 1.4: Schematic view of the ponderomotive force. A not relativistic electron (big blue dot in the picture) is initially near the center of the laser axis (x-axis). It experiences a transverse force (displacement) due to a spatially varying laser intensity profile. The laser electric field varies in the y-direction and in time. The figure comes from [72].

The ponderomotive force, in the not relativistic case (v $\ll$ c), is defined as the gradient of the time-averaged ponderomotive potential $\overline{\Phi_{\text{pond}}}$ [72]:

$$\mathrm{F}_{\text{pond}} = -\nabla\overline{\Phi_{\text{pond}}} = -\frac{e^2}{4m_e\omega^2}\nabla\mathrm{E}^2 \tag{1.8}$$

However, as soon as the transverse velocity approaches c, with increasing intensity, not only the spatial intensity distribution, but also the relativistic motion in the laser field contributes.
The time averaged ponderomotive force, for a linearly polarized laser, in the relativistic regime, becomes [72]:

$$\mathrm{F}_{\text{pond}} = -mc^2\nabla\sqrt{1+\frac{a_0^2}{2}} \tag{1.9}$$

The laser magnetic component becomes not negligible for relativistic velocities, i.e. the electron has two components perpendicular and parallel with

respect to the laser propagation's direction. Details of these calculations can be found in ref. [72].
Once we described the interaction of laser pulse with a single electron and the target ionization, we consider the interaction of laser beam with a plasma.

1.2.4 Key parameters of laser-plasma interactions

The physics processes involved in laser-plasma interactions are quite complex, but useful information can be retrieved by considering the interaction of a laser beam propagating in a plasma and the plasma key parameters [38, 96].
The Debye length is the characteristic length of a charge screening in plasma and it is defined as:

$$\lambda_D = \left(\frac{\epsilon_0 k_B T_e}{n_e e^2} \right)^{1/2} \tag{1.10}$$

where k_B is the Boltzmann constant, T_e is the electron temperature and the n_e is the electron density.
The Debye length is the shielding distance over which mobile charge carriers (e.g. electrons) screen out electric fields in plasmas. In a system with dimension L_{system}, outside of a volume of radius equal to the Debye length λ_D, whenever any external fields or local charge concentration are introduced, the created electric fields are shielded, i.e $\lambda_D \gg L_{system}$.
Another important aspect is the collective nature/behaviour of the plasma. The number N_D of particles in the "Debye Sphere" is calculated as [38, 44].

$$N_D = n \frac{4}{3} \lambda_D^3 \pi \tag{1.11}$$

For $N_D \gg 1$ the thermal motion of the particles is more relevant and coupling among the particles is eventually weak, i.e. the greater the number of particles within the Debye sphere, the less probable the collisional effects. For $N_D \ll 1$, the coupling between the particles is strong and the trajectories are strongly affected by the near neighbour interaction.
The propagation of an electromagnetic wave in plasma can be derived, using the Maxwell equations, under the assumption of small amplitude plane waves, colds electron-ions and not relativistic effects, i.e the following dispersion relationship is obtained [38, 72]:

$$\omega_L{}^2 = \omega_p{}^2 + k^2 c^2 \tag{1.12}$$

where ω_L is the frequency of the laser, while ω_p is the electron plasma frequency and it is defined as:

$$\omega_p = \sqrt{\frac{n_e e^2}{\varepsilon_0 \gamma m_e}} \tag{1.13}$$

where n_e is the plasma electron density and γ is the cycle averaged relativistic factor given by [38]:

$$\gamma = \sqrt{1 + a_0^2/2} \tag{1.14}$$

Furthermore, the eq. 1.12 can be also written as:

$$\omega_L^2 - \frac{n_e e^2}{\epsilon_0 \gamma m_e} = k^2 c^2 \tag{1.15}$$

From equations 1.12 and 1.15 it can be seen that the laser cannot propagate when the plasma frequency ω_p exceeds the laser frequency ω_L. i.e the plasma is opaque to the laser light[96].
The electron density at which the transition between opaque to transparent occurs, i.e. $\omega_p = \omega_L$ is known as critical density n_c and it is expressed as:

$$n_c = \frac{\omega_L^2 \epsilon_0 \gamma m_e}{e^2} \tag{1.16}$$

The critical density discriminates two kinds of plasmas: the *underdense* plasma when $n_e < n_c$ and the *overdense* plasma when $n_e > n_c$ [72]. The region for which $n_e = n_c$ is the critical surface. In this part, the laser light is both reflected and absorbed (see section 1.2.5). However, an evanescent component of the wave, penetrates the plasma beyond the critical surface into the overdense region. The characteristic length from the critical surface to where the laser electric field (evanescent component) has dropped to 1/e is called the skin depth l_s and is proportional to:

$$l_s \propto \frac{c}{\omega_p} \tag{1.17}$$

Another quantity has to be introduced in order to fully characterize this type of interaction: the plasma scale length L. When the leading edge of an intense laser pulse interacts with a solid target in vacuum, it ionizes it. This generates a plasma, that starts to expand, creating a density gradient.
The plasma scale length L is defined as[38]:

$$L = c_s \tau_L \approx 3\sqrt{\frac{T_e}{[\text{keV}]}}\sqrt{\frac{Z}{A}}\left(\frac{\tau_L}{[\text{fs}]}\right)\dot{A} \tag{1.18}$$

where τ_L is the laser pulse duration, c_s is ion sound velocity defined as [38]:

$$c_s = \sqrt{\frac{Z T_e k_B}{m_i}} \tag{1.19}$$

T_e is the temperature of the electrons, Z and A are the charge and the mass number of the plasma ions. The scale length is commonly used as a measure of the plasma steepness. The steepness and the electron density of the plasma allow to distinguish the dominant processes of laser absorption[96], that are described in the following section.

1.2.5 Electron heating mechanisms

The direct laser driven acceleration is not accessible with the currently available laser intensity[72]. Thus, the energy of the laser is transferred to the electrons in a plasma by means of different heating/absorption mechanisms. They are classified in *collisional* and *collisionless* absorption mechanisms.
When the laser intensities were low (less than 10^{14} W/cm^2) compared to today's standards (10^{18} W/cm^2 – 10^{20} W/cm^2) collisional processes were prevalent. According to the current laser intensities, *collisionless* processes are considered the main laser light absorption mechanisms. They include resonance absorption, Brunel heating and relativistic $\vec{j} \times \vec{B}$ heating. In the following, we will describe them and their differences.

Collisional absorption

The laser light absorption mechanisms can be discriminated by the collisionless ones, introducing the collision ion-electrons frequency, that is given by [106] :

$$\nu_{ei} \approx 3 \cdot 10^{-6} \ln \Lambda \frac{n_e Z}{T_e^{3/2}} \tag{1.20}$$

where n_e is the electron density in cm^{-3} units, while T_e is expressed in eV.
As it is clearly visible, high density plasmas, i.e high Z, even on a subpicosecond timescale, at low temperatures are mainly characterized by collisional processes. They include also the *inverse Bremsstrahlung*.
The *inverse Bremsstrahlung* radiation is the radiation produced when an electron is de-accelerated by charged particles. An electron is accelerated by the laser field because of the transfer of energy from the laser photons to the electrons. However, as mentioned before, the increasing laser intensities and higher electron temperatures have made the collisional absorption processes more and more ineffective. Thus, for short and intense laser pulses, collisional absorption is, in general, less predominant with respect to collisionless absorption mechanisms.

Resonance Absorption

The most known collisionless absorption mechanism is the resonant absorption, which is illustrated in figure 1.5. It is relevant for laser intensities between 10^{14} W/cm^2 and 10^{17} W/cm^2, short pulses and steep ($L/\lambda \leq 1$) plasma gradients. At higher intensities, the resonant absorption mechanism is still present, but it is not the dominant absorption process.

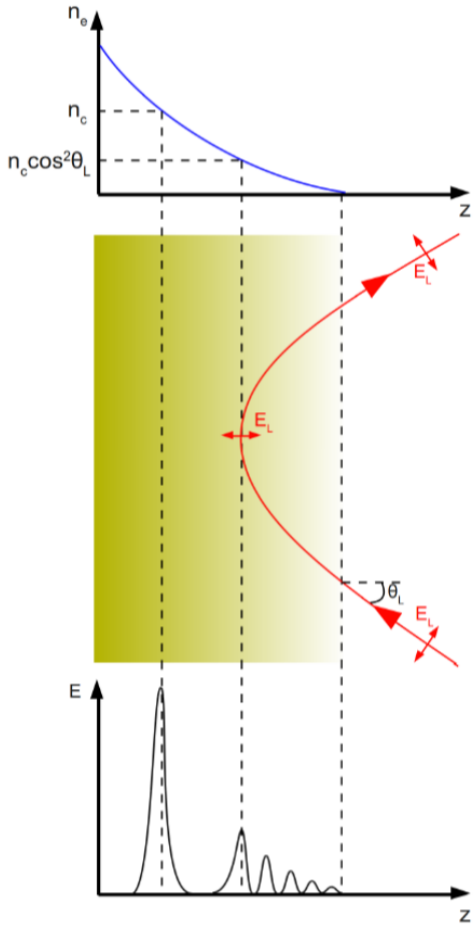

Figure 1.5: The illustration of resonance absorption mechanism: The laser (p-polarized) is propagating through a density gradient. As soon as the laser reaches the density of $n_c \cos^2(\theta_L)$, a plasma wave is resonantly excited in the over-dense plasma. Figure reported from [203].

The resonance absorption occurs when the laser pulse has an incidence angle θ_L with respect to the target normal axis [151] and is p-polarized, i.e the laser light is directed in the incident plane. The laser pulse first propagates

through the plasma density gradient, which is underdense. The laser pulse is initially deflected and then eventually reflected, as it is shown in the figure 1.5, reaching the electron density value [106]:

$$n_e = n_c \cos^2(\theta_L) \tag{1.21}$$

The evanescent electric field component, which is normal to the target, due to the p-polarization, can tunnel into the plasma up and resonantly excites an electron plasma wave at the critical surface at the plasma frequency ω_p. The energy is transferred from the laser pulse to the plasma, by dumping this wave, e.g. trapping of the particle or with the wave breaking [106, 217]. This results in a fast electron population that is injected into the target at the laser frequency.

Vacuum heating or Brunel heating

The main difference between the resonance absorption and the Brunel heating or not-so resonant absorption is given by the steepness of the plasma gradient[72].
The electrons are initially pulled out into the vacuum by the electric field component orientated normally to the plasma boundary (p-polarization) in one half-cycle of the laser field. In this scenario, the plasma is overdense, i.e the laser can penetrate up to the skin depth (see section 1.2.4).
As the laser field changes sign (in the other half-cycle of the laser field), the electrons that have been accelerated beyond the critical surface, are rejected back to the plasma but they are screened from the laser field itself. Therefore, they can continue to travel the plasma, propagate normally to the target and transfer the energy to the plasma by collisions. Since the laser pulse repeats this process every cycle, electron bunches are accelerated into the target at the frequency of the incident laser pulse ω_L.

Relativistic $\vec{j} \times \vec{B}$ heating

For high intensity laser pulse ($I > 10^{18}\ Wcm^{-2}$) and short pulses, another electron heating mechanism is the relativistic $\vec{j} \times \vec{B}$ heating [106]. It relies on the magnetic force component $v \times B$ of the Lorentz equation, i.e it is very effective for an angle of incidence of the laser near or at the target normal, while for the previous absorption mechanisms the laser is p-polarization and has an oblique angle of incidence.
The heating mechanism is due to the nonlinear oscillation components driven by the magnetic force, that provide oscillatory motion of the electrons. For

linearly polarized laser pulse, the ponderomotive force term is expressed as [106]:

$$f_p = -\frac{m}{4}\frac{\partial v_l^2(x)}{\partial x}[1 - \cos(2\omega_L t)] \tag{1.22}$$

where ω_L is the laser frequency and v_l is the electron quiver velocity[106]. The first term is related to the density gradient of the electrons in the forward direction, while the second term, due to $\vec{j} \times \vec{B}$ components, causes the longitudinal oscillations of the electrons at twice the laser frequency along the direction of the laser propagation.
However, the oscillation term of eq. 1.22 is suppressed for circular polarization laser light because of the absence of the oscillatory components in the longitudinal electron motion. This aspect is favourable for a specific acceleration mechanism, known as Radiation Pressure acceleration (RPA) [115, 153, 167].

1.3 Laser driven proton acceleration

In LDPA, numerous have been the acceleration scenarios have been intensively studied and investigated, using a great variety of laser and target parameters.
Nowadays, the majority of the LDPA experiments are performed with laser intensities between 10^{18} W/cm^2 to 10^{20} W/cm^2 i.e a_0 (eq. 1.2)$>$ 1, laser energies between few mJ up to hundreds of Joules, laser pulses from few tens of fs up to ps and target (typically metallic foils) with a thickness that goes from few nm up to few μm.
The energetic ions observed as a consequence of the laser-plasma interactions. The plasma fields are created due to the laser heated electrons. Plasma electrons mediate the forces of laser fields on ions by generating quasi-static electric fields which arise from local charge separations. These quasi-static fields are responsible for the ions acceleration [72].
The laser energy can be efficiently transferred to the plasma electrons by various mechanisms (see subsection 1.2.5) leading to different ion acceleration regimes [72]. The most studied schemes in laser driven ion acceleration include the target normal sheath acceleration (TNSA) [188, 216], breakout afterburner (BOA) [219], radiation pressure acceleration (RPA) [59, 167, 153, 115] to name a few. In the next section, we will describe in detail the TNSA [216, 188, 136], that is the acceleration mechanism relevant for the topics of this work.

1.3.1 Target normal sheath acceleration (TNSA)

When a laser with intensities between 10^{18} W/cm^2 to 10^{20} W/cm^2, pulses from few tens of fs up to ps interacts with the foil target of few μm, atoms on the front side are already ionized by the leading edge pulse (see section 1.2.1) and form an expanding plasma, as illustrated in figure 1.6. When the main pulse reaches the plasma, it is partially absorbed at the plasma critical surface (i.e. surface with density at which laser and plasma frequencies are the same), heating up the surface electrons to energies of several MeV.

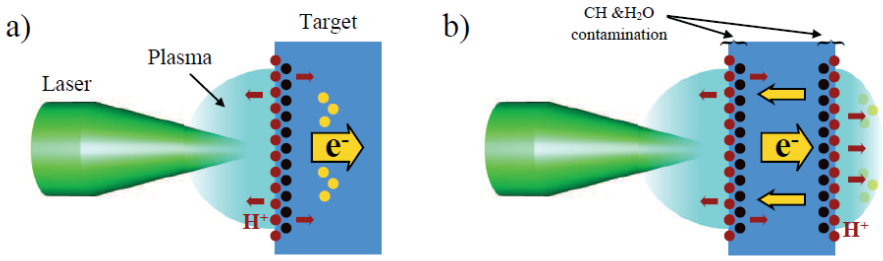

Figure 1.6: The illustration of the steps of the Target Normal Sheath Acceleration (TNSA) scheme. Figure extracted from [96].

There is not a dominant heating absorption process, but according to the angle of incidence between the laser and the target, one mechanism can be favourable compared to the others, e.g a normal angle of incidence favours more the relativistic $\vec{j}\times\vec{B}$ heating respect to the resonance absorption and/or the Brunel heating (see section 1.2.5).
The plasma electrons are the mediators for the laser energy because the heavy masses of the protons impede their direct acceleration by the laser field.
The target thickness, in this case, plays an important role because it must be thick enough so that the back surface remains unperturbed by the laser pre-pulse and thin enough so that the electrons manage to cross it. These energetic electrons manage to cross the target and eventually leave it at the back surface, creating a strong charge separation electric field E_s between the positive ionized target and the set-up electron sheath.
The extension of this field is given by the Debye length of the hot electrons:

$$\lambda_D = \sqrt{\frac{\epsilon_0 k_B T_h}{e^2 n_h}} \tag{1.23}$$

it scales as $E_s \sim k_B T_h / e\lambda_D$ (typically few μm), and it has an intensity of the order of TV/m.

This field is considered quasi-static because the electrons are continuously pulled back into the target by the field and replaced by re-circulation of the hot electrons from the front side.
The generated ions (both carbon ions and protons) are pulled off from the target and accelerated normally to it due to the quasi-static electric field. Thus, the name of this acceleration mechanism is Target Normal Sheath Acceleration (TNSA). The proton and ion beams come from the hydrogen layers of the contaminants, ever-present on the targets, due to the vacuum imperfection condition and the vacuum pump oil.
There are several models that have been studied for analyzing this acceleration scheme. We briefly report a few of them, including the assumptions and the theoretical results.
Wilks et al. [216] assume that the electrons from the front side are directly transported to the back of the target surface.
However, the fluid model of Mora [136] is considered the most accurate and studied for the TNSA scheme. It assumes that the electron temperature follows a Boltzmann distribution and that the cold ions are at rest. Starting from a set of fluids equations (i.e Poisson's equation, the equation of motion and continuity equation), the ion position and velocity can be deduced. The final ion position and velocity are given by:

$$z_f = 2\sqrt{2e_N}\lambda_D[\tau \ln(\tau + \sqrt{\tau^2+1}) - \sqrt{\tau^2+1} + 1] \tag{1.24}$$

$$v_f = 2c_s \ln(\tau + \sqrt{\tau^2+1}) \tag{1.25}$$

where $\tau = \omega_p t_a/\sqrt{2e_N}$ and t_a is the acceleration time.
The maximum energy, estimated using this model, is expressed as:

$$E = 2ZT_e(\ln\tau + \sqrt{\tau^2+1})^2 \tag{1.26}$$

where E indicates the ion energy, Z is the ion charge number, T_e is the electron temperature. Furthermore, the exponential decrease in the energy spectrum (Number of particles per MeV) is calculated as:

$$\frac{dN}{dE} = (\frac{n_i c_s t_a}{\sqrt{2ZT_eE}})exp(-\frac{2E}{ZT_e}) \tag{1.27}$$

where n_i is the ion density, c_s is the ion sound velocity (see subsection 1.2.4). However, this model showed an overestimation of the maximum energy cut-off for long pulse duration laser compared to the experimental results. This is probably due to the need of a proper hot electron temperature estimation and the approximation of quasi plasma neutrality ($qn_{ion} \simeq n_e$) [44]. Hence, other models and approaches have been investigated.

Starting from eq. 1.24 and 1.25 it is possible to deduce that, when $t_a \to \infty$ i.e $v_f \to \infty$, we obtain not physical results. An upper limit must be imposed to t_a. The obvious choice is t_a equal to the laser pulse duration τ_L. However, Fuch et al [67] have proved that for laser intensities greater than $3 \cdot 10^{19}$ W/cm^2, the acceleration time t_a can be approximated to:

$$t_a \simeq 1.3\tau_L \tag{1.28}$$

Scheiber et. al. [175] have proposed the "quasi-static" field approach, that takes into account the surface charge created by the hot electrons on the rear back of the target. It also assumes that the electron bunch length is equal to $c\tau_L$ at the rear side of the target and they spread transversely over a circle area with radius r_{sheath} [176]:

$$r_{sheath} = r_L + l\tan(\theta/2) \tag{1.29}$$

where r_L is the laser focal spot radius, l is the thickness of the target and θ is the expansion cone angle.
Furthermore, the average electron density at the back ($n_{(e,0)}$) becomes:

$$n_{(e,0)} = \frac{N_e}{c\tau_L \pi r_{sheath}^2} \tag{1.30}$$

where N_e is the electron density and $N_e \approx \eta E_L / \ k_B T_e$, where T_e is the electron temperature, E_L is the laser energy, while η indicates the conversion efficiency (laser-target interaction).
The ions energy ε_{ion}, in this case, can be expressed as:

$$\varepsilon_{ion} = q_i 2mc^2 (\frac{\eta P_L}{P_R})^{\frac{1}{2}} \tag{1.31}$$

where P_L is the laser power and $P_R \simeq 8.17$ GW is the relativistic power.
This model is suitable for describing experiments with laser intensities between 10^{18} W/cm^2 and 10^{19} W/cm^2. These model results provide useful guidelines for introducing the TNSA proton beams properties.

1.3.2 Targets engineering design for LDPA optimization

This short description regarding the field of the target engineering optimization aims at offering an insight on one of the "direction", i.e the design and the application of sophisticated manufacturing techniques [104, 70, 123] that is followed in LDPA for improving the final proton features.

In the following, I will discuss some nanostructured engineering targets, that have been studied during my PhD activities [123, 205, 206].
Many efforts [155, 123] have been done in order to increase the laser-to target absorption, which is strongly related to the increase both in mean energy and number of the "hot" electrons, responsible for the proton acceleration process.
Margarone[123] et al, were among the first, that experimentally implemented nanostructured thin plastic foils as targets. They [123] showed that the irradiation of a 100 TW femtosecond laser on a target with an addition of a monolayer of polystyrene nanospheres on the front side, can lead (optimum spheres' diameter of 535 nm [123]) to an enhancement in both final maximum proton energy and proton numbers (charge).
The enhancement in proton cut off, observed experimentally using time of flight (TOF) and Thomson Parabola (TP) measurements, was about 60% for a proton beam with a maximum energy of the order of 4.7 MeV, as well as the improvement in total proton number of the order of 5 times for proton energy above 1 MeV[123].
According to this, they deduced that the presence of the nanostructured particles can act as a shield for the incident laser and it offers the possibility to heat a larger surface, i.e the irradiation of a high number of particles. It is also assumed that the optimum laser-to target absorption (collective motion of the electrons) can be reached when the spheres' diameter is larger or comparable with the half of the laser wavelength ([192]).
The experimental evidence that we observed in [205, 206], show that an enhancement in maximum proton energy and proton numbers can be achieved by depositing on the target surfaces, different types of nanoparticles, such as silver, gold, aluminium compared to the planar cases (conventionally gold or aluminium solid foils). We have mainly attributed these results to the different electron density given by the heterogeneity of the target materials. It was pointed out that, not only the spheres' diameter [123, 192] of the nanoparticles, but also the gap between them can provide an improvement in maximum energy of the generated proton beams because the gaps' space parameter favours the transition through the target bulk of the hot electrons. More details regarding the spectra measurements are reported in chapter 2.

1.4 TNSA ion (protons) beams properties

We describe in details the properties of the TNSA (see section 1.3.1) ion beams.
One of the first problems of the TNSA ion beams is the origin of their ac-

celeration. Some measurements proved that the acceleration of the ions can come from the front side [45, 119, 144], others proved that they can be accelerated from the rear side of the target [188, 116, 86] (see section 1.1.1).
Both protons and carbon ions are ever-present contaminants on the target surface. As reported in [188], the dominant species in the TNSA mechanism are the protons, because of their high charge-to-mass ratio and the low ionization potential of the hydrogen. By this, we mean that they are accelerated first and more efficiently compared to the ions. However, the acceleration of the heavy ions can be favoured, compared to the protons, with other techniques, such as removal of the contaminant on the targets before laser irradiation [88, 87] or by using an ion gun [5].
We also list and analyze the following features of generated TNSA protons, i.e. the proton sources parameters, that are:

- Energy spectrum
- Beam divergence
- Beam emittance and laminarity
- Proton source size

All these properties have been subject of different theoretical studies [136] and experiments[47, 24], that are summarized in the following.

1.4.1 Energy spectrum

One of the most important features in LDPA is the proton spectrum, i.e. numbers of protons dN/dE for a certain energy within a certain energy interval dE. In some cases, the normalization to the solid angle within the protons are generated, is taken into consideration. In this case, the spectra units become number of protons/MeV/ster.
Proton spectra can be measured with different types of detectors, such as Radio chromic films (RCF) [89], Thomson parabola spectrometers (TPS)[198], Image plates (IP) [134], CR-39[69], etc. A detailed description of them is presented in chapter 2.
TNSA proton spectra have a typical Maxwellian energy distribution, as it is shown in figure 1.7.
The use of the following fitting formula allows an estimation of the average temperature of the beam:

$$\frac{dN}{dE} = N_0 e^{-\frac{2E}{k_B T}} \tag{1.32}$$

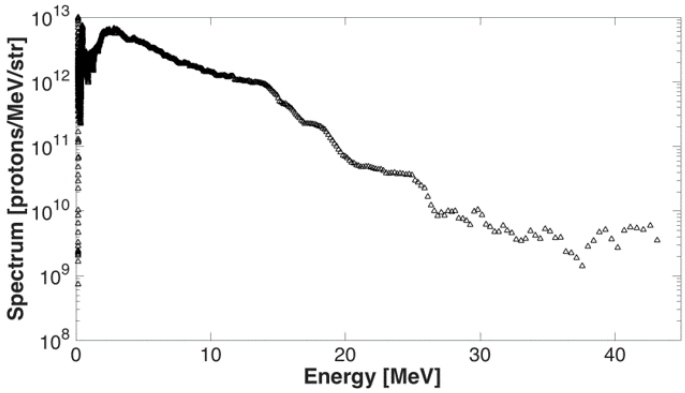

Figure 1.7: Typical TNSA spectrum. Proton energy spectra measured, using as source the Jupiter Laser facility ($\lambda \sim 1064$ μm, intensity I $\sim 10^{20}$ W/cm^2 Energy E $\sim$ 250 J, laser pulse $\sim$ 700 fs). Figure reported from [180].

where N_0 is the fitting parameter related to the initial hot electron density, T is the initial hot electron temperature and E is the proton energy.
From the proton spectra reported in [180], we can deduce the important features that make laser driven proton beams attractable candidates for applications.
They are characterized by a broad energy spectrum, that usually goes from a few keV up to few tens of MeV. The spectrum has a maximum energy cut-off. The maximum proton energy observed experimentally is 100 MeV, as reported in [90]. The high number of particles ($\sim 10^{13}$ particles/shot) corresponds to high charge (nC) and high current (kA) per bunch. Furthermore, the proton bunch length is of the same scale as the laser pulse duration (see section 1.3.1).
There have been also numerous parametric studies and experiments in which proton spectra features in terms of maximum energy cutoff and particle numbers have been investigated and linked to the laser (e.g. intensity and pulse duration) and targets parameters (see section 1.3.2).
Different scaling laws for proton energies as a function of irradiance and in correlation with the pulse duration have been obtained by Borghesi et al. [23], comparing and collecting many experiments results with a wide variety of laser systems. They assumed that the maximum proton energy scaled varies with the target thickness and with the laser pulse intensity I, increasing roughly as $\sqrt{I}$ for laser pulse duration in the range 300 fs–1 ps, and as I for a shorter laser system. More details related to these parametric studies of the dependence of the maximum proton energy achievable, respect to laser pulse duration, irradiance[113, 23], energy [66], power, the influence of laser

prepulse [99] and target thickness can be found in the ref. [50] and references therein.

1.4.2 Beam divergence

The second proton source parameter, that we consider, is the beam divergence. The typical divergence of the generated laser driven proton beams depends on the shape of the accelerating electric shield that guides them (see section 1.3.1).
Romagnani et al. [168] were among the first that measured in a pump-probe experiment, this shape. The observed shape has a Gaussian distribution in the transverse direction, as shown in figure 1.8.

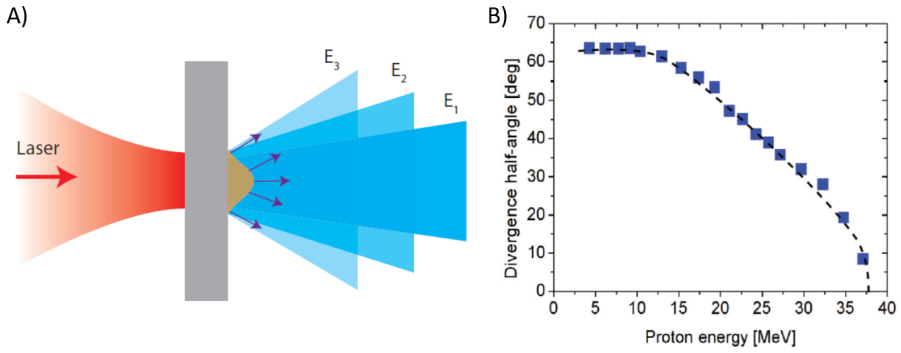

Figure 1.8: (A) The illustration shows the divergence of the TNSA accelerated protons for different energies ($E_1 > E_2 > E_3$). (B) An example measurement of the TNSA proton energy vs divergence half angle (energy-divergence dependence of a laser driven proton beam). Figure extracted from [159].

Due to this, the protons from the center are accelerated more than the ones located on the sides. Hence, the ion (proton) front has a Gaussian shape. The protons accelerated along the normal direction of the ion front, i.e in the central part of the sheath field, are accelerated with a smaller divergence compared to others. As a consequence, the divergence of the proton beam is a function of the proton energy (see figure 1.8).
The effect of the beam divergence of a typical TNSA proton spectra [77, 121] in a laser driven hybrid beamline for cultural heritage applications will be also discussed in the simulation results of chapter 6.

1.4.3 Beam emittance and laminarity

The laser driven proton beams, accelerated at the rear part of the target, have also good property in terms of laminarity.
In general, a flow is considered laminar if the streamlines are parallel and do not overlap with each other, while flow is considered turbulent in the opposite case, i.e the streamlines cross multiple times [165].

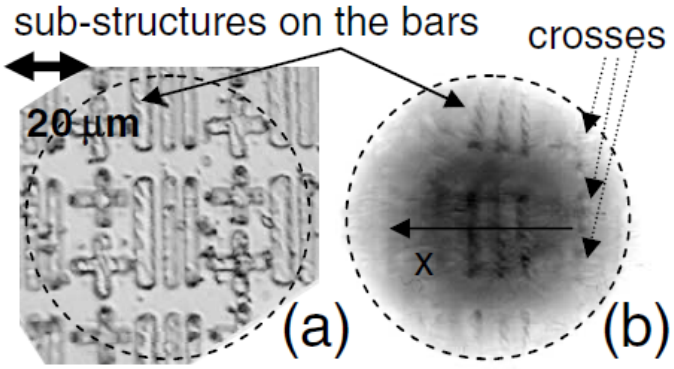

Figure 1.9: The figures (a)-(b) show the grooved target details and the corresponding RCF detection. Figure reported from [47].

The main difference between long pulse, moderate intensity lasers and short pulse, ultra-intense lasers experiments is attributed to the fact that the latter can produce short bunches of fast electrons. These electrons can form a dense sheath on the unperturbed rear surface because they can propagate through thick targets without much energy loss. Hence, the accelerating field is higher than on the front surface where there is the direct interaction with the laser and the acceleration is also more laminar since the process starts from a cold unperturbed surface[9].
In the case of the laser driven proton beams, the use of grooved targets irradiated by high intense laser has been investigated[47]. Small details of the target surface on a μm scale have been distinguished on the detector (RCF stacks) (see figure 1.9).
This indicates that it is possible to find a good correspondence point to point between a proton coming from the grooved target and the detector, i.e the proton trajectories do not overlap and the proton beam is highly laminar.
The laminarity of a beam is closely linked to the concept of emittance. The area occupied in the phase-space by a beam is used to describe the quality of a beam. This quantity is called geometrical emittance and it is usually

indicated as ϵ_x in the phase space (x-x'), ϵ_y in the phase space (y-y') and ϵ_z in the phase space (z-z'). In a Cartesian system (x-y-z), if z axis indicates the propagation direction, the emittance is called longitudinal one, while on the x and y, it is called transverse.
The transverse emittance is evaluated, using the source size and the angle of emission of the proton beam [165]. It is correlated with the laminarity of the proton beam, i.e the smaller is the transverse emittance, the higher is the laminarity of the beam. In ref. [47], a measurement of the transverse emittance for laser proton beam of 10 MeV is presented. Its value is less than 0.004 mm mrad, which is almost 100 times better than that of conventional RF-based accelerators.
For the longitudinal emittance, the longitudinal phase space is usually referred to an ideal particle, named synchronous particle [165]. Hence, the coordinates z' are replaced by the energy relative to the synchronous particle and z by the phase or distance relative to the synchronous particle. The area, therefore, is measured in eV·s. In ref [47], an estimation of the longitudinal emittance is also investigated and its value is $\sim 10^{-4}$ eV·s.
The concept of beam emittance reported in this section will be furthermore explained in chapter 6, where the evolution in the phase-space of a laser driven proton beam along a transport beamline will be investigated.

1.4.4 Proton source size

Cowan et al [47] were the first that, through the laser irradiation of a target with equally spaced grooves on the back surface and using as detector RCF stacks, retrieve information about the spot size from where laser generated protons are originated (see figure 1.9).
Moreover, due to the stopping power of the RCF stack (see chapter 2), they were able to distinguish the spot sizes for different proton energies.
For example, if the grooves are spaced by a distance of 3.6 μm, as reported in [47] and on the RCF 10 groves are detected, then the proton spot size is $\sim$ 36 μm.
Roth et. al [171], used as well the same grooved target of ref [47]. They also found, in their experiments, using laser intensities between 10^{18} W/cm^2 and 10^{20} W/cm^2 and pulse duration of the order of $\sim$ ps, that the size of ion sources is energy dependent [171, 47] and it is of the order of few hundreds of μm for target thickness that goes from few μm up to 100 μm.
A second technique for measuring the ion source size is to use a metallic mesh, placed between the target and the detector, as it is was done in refs. [24, 67].
Borghesi et al, [24] have performed measurements of the magnification of a

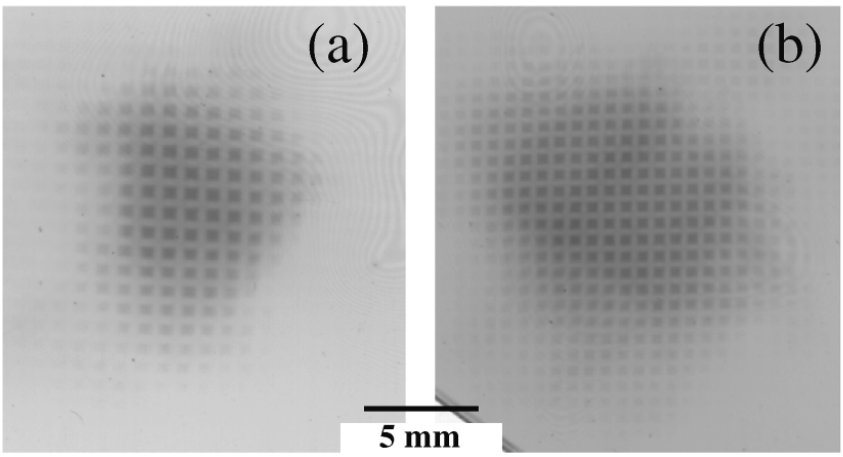

Figure 1.10: The figures (a)-(b) are collected, using RCF diagnostics and show the shadow of grid meshes (period: 31 μm, line width: 10 μm, line thickness: 5 μm) impressed in the proton beam profile, with the grid placed, respectively, at 0.6 and 1 mm from the Al foil producing the protons. Figure extracted from [24].

mesh, using RCF as diagnostics. We reported in figure 1.10 the images of the RCF placed at 23.8 mm from the Al foil, irradiated with the VULCAN laser ($\lambda \sim 1054$ μm, 1 ps, energy up to 100 J, laser intensity of $\sim 7\ 10^{19}\ W/cm^2$) The magnification expected for a point-projection imaging scheme is the ratio between the source-to-detector distance and the source-to-object distance.
From the proton source size measurements, they [24] found out that there was an overestimation between the expected magnification and the measured one. These differences can be explained if the magnification is estimated for protons originated from a virtual point source located not at the target surface, but at hundreds of μm in front of it.
From the source size measurements [47, 24, 171] reported, it has been seen that the protons do not stem out from a single point of the target surface but from a surface. The protons are also laminar, i.e correlation between angle and transverse position. This implies that protons are accelerated as if they would come from a virtual point source (VPS). In [24], the size of the VPS has been calculated using numerical codes [24] and it was of ~ 80 μm, located few hundreds of μm in front of the target.
Different measurement systems for estimating the VPS, using a copper mesh [67] or a knife-edge configuration [177] have been also performed and values for the proton virtual source of the order of few tens of μm, situated a few μm behind the target, have been calculated.

1.5 Summary and conclusions

In this chapter, we summarized the basic concepts regarding the laser-plasma interactions, that enables the generation of laser driven proton beams.
In section 1.1.1, we reported the main experimental results, that represent important steps for the investigation of laser driven proton sources.
We introduced and described the main parameters for defining the plasma behaviour under the irradiation of high intense laser system ($I > 10^{18}\ W/cm^2$).
Furthermore, we briefly explained the electron heating mechanisms, that characterize the laser-plasma interaction, e.g. vacuum heating and relativistic $\vec{j} \times \vec{B}$ heating.
They play an important role in laser driven proton acceleration, as well as the target features (see section 1.3.2). Then, we focused our attention on the TNSA scheme.
In section 1.4, we listed and described the TNSA proton beam properties, that represent the core of this work.
Their features are the starting point in the development of a hybrid beamline for applications (see chapter 6), as well the objectives towards the improvement of the laser driven proton diagnostics (see chapter 4), which allows a better understanding of the complexity of the laser-plasma interactions, which guide the ion (proton) acceleration.

Chapter 2

Laser driven ion diagnostics

Multi-MeV laser driven ion beams [90, 113] contain different variety of ion species and ion charges.
In the last decades, numerous have been the techniques and the charged particle diagnostics [22] that have been adapted, studied, developed and tested in order to diagnose and better understand the mechanisms of laser driven ion acceleration discussed in chapter 1.
In this chapter, we aim at providing an overview of the most commonly used laser driven ion beam diagnostics [22].
Thomson Parabola spectrometer (TPS)[198, 166], Radio Chromic Films [89, 150] (RCFs), Image Plates (IP)[134, 121], Columbia Resin #39 (CR-39) [69, 63], nuclear activation [188], fast scintillators coupled to a CCD or a photo multiplier tube (PMT) [22], Micro-channel plates (MCP) [213] coupled to a phosphor screen and CCD, time of flight spectrometers[131, 182] belong to the current state of the art for the detection and the characterization of laser driven ion beams.
In the following sections, we describe in detail the characteristics of RCFs, IPs, CR-39, MCPs, emphasizing for each of them advantages and disadvantages. These measurement detectors have been used in this thesis work.
Most of these diagnostics don't provide the measurements' results online, because they are passive detectors [22]. By this, we mean that they don't allow to characterize the beams in a direct way and they need post-processing that, in some cases, is very complex, such as that for the CR-39 (see section 2.6).
We describe also in detail the Thomson parabola spectrometer (TPS) [198] relevant for the purpose of the study of chapter 4.

2.1 Charged particle diagnostics: context and state of the art

Nowadays, there is a great variety of charge particle detectors/diagnostics [22] used for recording high energy laser driven ion beams.
Among them, there are the RCFs [69, 89] and the Thomson Parabola Spectrometer (TPS) [198, 1]. The TPS is usually coupled with one or more types of measuring instruments (detectors), such as:

- Micro channel plates (MCP);
- Image plates (IP);
- CR-39 (polyallyl diglycol carbonate);

The use of these diagnostics is not mutually exclusive, therefore, it is possible that combinations or sequences of them are implemented together in the same experimental setup, for example, for calibration purposes [95, 128].

2.2 RadioChromic Films (RCFs)

Radiochromic films (RCFs) [89] are multilayered dosimetry films, that were originally designed for medical applications [146] and are sensitive to different types of radiations (electrons, photons, protons). However, in the last few years, they have become as well valuable detectors for laser driven proton acceleration[89, 150]. They enable the measurements of the spatial and spectral characteristics of the beams [89].
There is a great variety of RCFs with different structures and different sensibility regarding the incident particles. They are made out of one or two active layers laminated between polyester film substrates and they are typically GAFCHROMIC EBT-type, MD-type, HV-type, as shown in figure 2.1. When the monomer contained in the active layer is exposed to ionizing radiation, it undergoes a polymerization and forms a dye of colour of darker blue or darker green, according to the batch of RCF used.
The GAFCHROMIC EBT2 types, for example, are characterized by a transparent substrate (the unexposed colour is transparent) and upon radiation, they appear blue, while in the latest version of RCFs, such as HD-v2 and EBT3, the substrate is blue-absorbing (the unexposed colour is yellow)[40], and upon radiation, they appear green.
The darkening of the RCFs is proportional to the dose the films are exposed to. After the exposure to the radiation, the RCFs can be read out using many

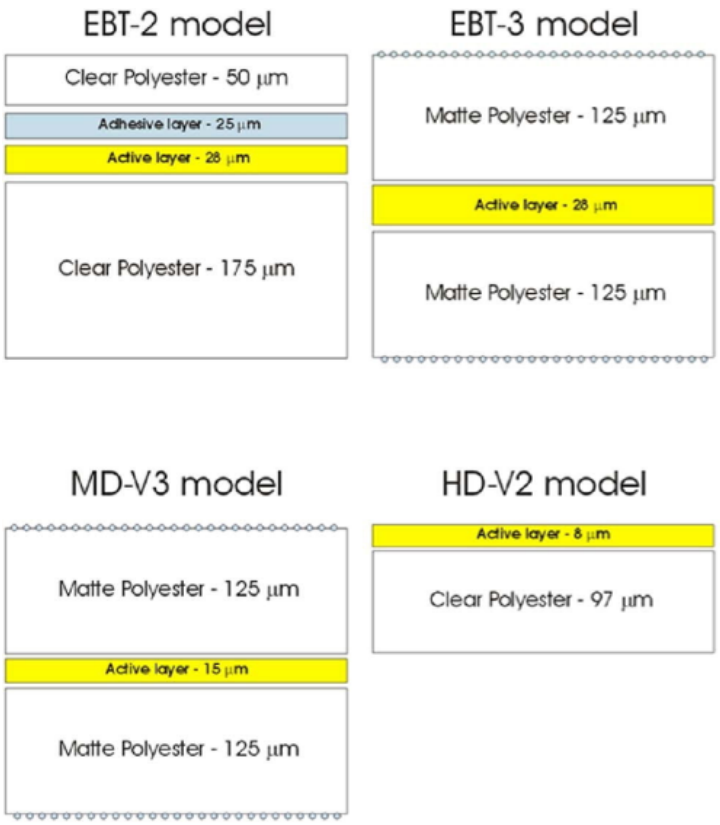

Figure 2.1: The structures of most used GafChromic RCF models: EBT-2, EBT-3, MD-V3 and HD-V2. Figure adapted from [54].

techniques and procedures or even simply using a flatbed color scanner in transmission mode [53].
However, different types of calibration measurements with a well defined dose are needed beforehand in order to obtain the correspondence between optical density (OD) and absorbed dose.
During my research activities, I collaborated on the first published calibration curve (OD vs Dose) of the RCF HD-v2 type. As reported in [40], the main goals of this work were two: (1) investigate and retrieve the calibration curves OD vs Dose for the RCF types EBT3 and HDv2 and test the variation of the response function utilizing different types of scanners; (2) provide an absolute calibration of EPSON 2450 scanner, using commercially available absorptive neutral density filters.
The EBT3 and HDv2 films have been calibrated, irradiating them with 10 MeV photons with know doses at the Stanford Medical LINAC[40]. After

that, the transmission of the films was measured in terms of optical density, scanning them using three different EPSON Precision 2450 scanners, three independent EPSON V750 scanners and two independent EPSON 11000XL scanners, both in the RGB channel and in gray-scale modes.
The scanners were located both in North America and Europe. Therefore, the first films scans have been performed more than 48 hours after the irradiation, time after which no variation over time of the film response, when stored in an appropriate envelope (not exposed to light), are observed [127, 117].
The net OD is calculated as OD_{net}=-log(signal$_{film}$/signal$_{film\ not\ exposed}$) , for each batch. This enables to take into account that they have been scanned in different moments and also to remove from the OD of the irradiated film the background accumulated overtime.

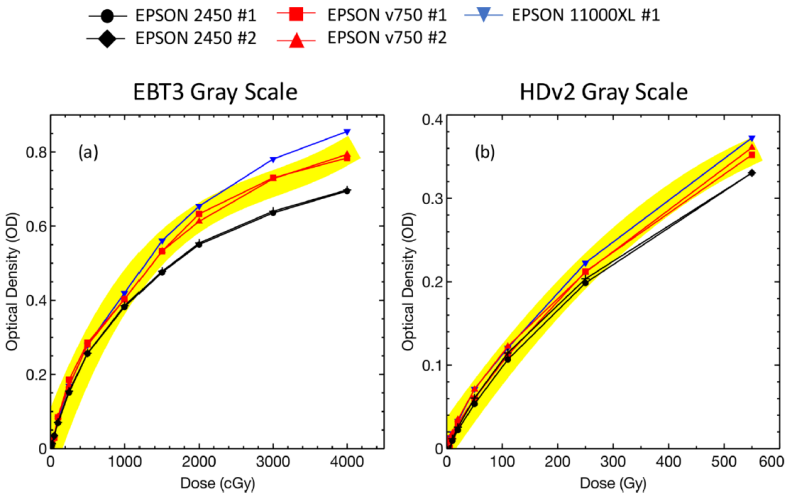

Figure 2.2: The Optical density versus deposited dose is shown for irradiated RCF EBT3 (a) and irradiated RCF HDv2 (b). On the top of the figures, the different types of used scanners are indicated. Both are scanned in grayscale. The yellow width of the fitting functions is not associated with quantitative values, but it is only represented for illustration purposes. Figure extracted from [40].

I have contributed to the curve calculations OD vs Dose related to the scanning measurements, that have been performed in North America in order to obtain the calibration fitting functions. They have been evaluated both in RGB channels and in grayscale. We reported as an example one the results, related to the scanning of both the EBT3 and HDv2 in grayscale. The figure 2.2 shows the optical density (OD) versus deposited dose with the fitting functions, whose detailed equations are indicated in ref. [40]. It was observed

that the variations of the response curves between the various models of the scanners are only of few percent.
In ref. [40], further details regarding the scanning in RGB channels are described. In particular, the green channel of the scans in RGB of both types of film shows, as in the case of the grayscale, that the OD measurements remain consistent with a variation of 16%, while the red and blue channels present more variations according to the type of used scanner.
In conclusion, in this case, it was found, that according to the needs of the use of the RCFs, the calibration curve of both the EBT3 and HDv2 may need to be done for the type of used scanner.
However, in the same ref [40], the optical density of know absorptive neutral density glass filter scanned in black and white has been provided, using one of the types of the scanner, the model EPSON2450. These calibration curves are useful because they allow any user to convert the same film calibration curve to any other scanner, using the same set of filters.

2.2.1 RCFs in stacks

RCFs are used in stacks and are considered suitable diagnostic for laser driven proton beams[89, 150]. As the protons travel inside the stacks, they deposit most of their energy at a given depth, i.e. the Bragg peak (see figure 2.2.1). Much energetic are the protons, the more they penetrate inside the RCF stack.
This property enables to obtain information regarding the spatial profile of the beams or/and to reconstruct the energy spectrum, at discrete intervals because each layer of RCF stack corresponds to a specific energy component of the total beam.
They are usually wrapped in an aluminium foil (see figure 2.2.1) in order to stop the heavy ions and to prevent their exposure to the light and/or some debris coming from the laser. This is also needed because RCF films are sensitive to the sunlight.
Usually, the stack can be composed of different type of RCFs and the first one can have high sensitivity (such as HD-v2, that has one single active layer) compared to the others in order to increase the lower detectable energy, as shown in figure 2.2.1.
The deposited dose of the protons can be calculated by resolving the equation of the stopping power, that depends on the incident energy, the material composition and the distance that the particles crossed inside the stacks. This is done typically with the software Stopping and Range of Ions in Matter (SRIM) [223].
The first step in order to retrieve the proton energy spectra is to calculate the

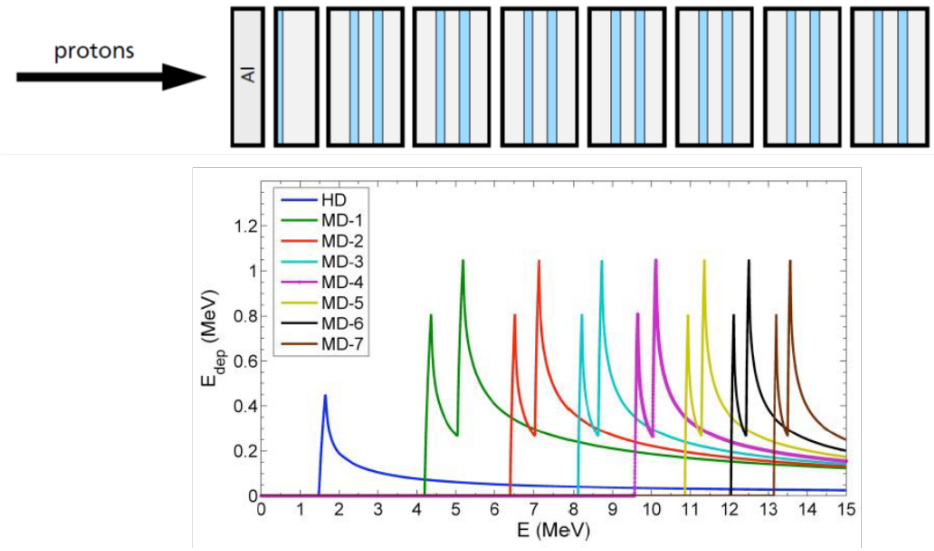

Figure 2.3: (a) Illustration of a typical stack of RCF irradiated by a proton beam and shielded by an Al foil (b) RCF stack with energy response due to the Bragg peaks, energy response vs energy deposited. Figures reported from [221].

deposited energy of the protons for the different active layers located within the RCFs. It is necessary to know, therefore, the correspondence between the OD and the energy dose that the protons deposit in each element that composes the stack.
As described before, it is possible, according to the batches of used RCF, to have the calibration curves. This can be provided by the supplier [121, 9] or using the procedure described in the previous section[40].
Then, it is possible to convert the full deposited dose in energy, considering that the RCFs are near-tissue equivalent dosimetric films, i.e. their density is similar to the density of human body $\rho \sim 1.3$ g/cm^3.
The full deposited energy can be calculated as E= ρ d$_l$ $\sum_{i=1}^{N}$ (D$_i$ A$_i$), where d$_l$ is the depth given by the thickness of the active layer, while D_i and A_i indicate the dose and the area of the pixel i respectively (resolution at which we scanned the films). At this point, we can plot the different energies contained in the RCFs and have the dependency between the deposited energy and the film numbers. This plot has a trend similar to the proton spectra.
However, for a more accurate estimation of it, we want to obtain dN/dE i.e the number of incident protons on the RCF, for a specific proton energy and within a certain energy interval dE.
This can be done, using a "posteriori" approach, such as the one described in

[121, 9]. The initial quasi- Boltzmann distribution that characterizes typical proton spectra [136] is simulated and then compared with the measured data (for each film that composes the RCFs stacks, we can calculate the deposited energy).
This iteration procedure is repeated, tuning the important spectral parameters of the distribution, i.e. the temperature of the hot electron and the cutoff in order to find the best fit with the measured data.
In this way, we can take into account how much energy one proton with certain incident energy deposits in each film. This approach, therefore, provides the correct correspondence of the numbers of protons vs energy.
Alternatively, it is possible to obtain the corresponding number of protons per MeV (N_{prot})[203], assuming that the protons stop in the layer where they deposit all their energy and neglecting the higher energy protons contributions. This number can be calculated as:

$$N_{prot} = \frac{\epsilon_{tot}}{\epsilon_{Bragg}\delta\epsilon} \tag{2.1}$$

where ϵ_{Bragg} is the Bragg peak energy of the considered RCF, while $\delta\epsilon$ is the energy width of the layer, considering, in the RCF stacks, the proton stopped at the front of the active layer and the one stopped at the back.
In conclusion, RCFs are a useful tool for retrieving information regarding laser driven proton beams. However, for the upcoming high repetition rate high intense laser systems, RCF stacks don't represent a valid option because they need to be replaced for every measurement and can be used only once.

2.3 Thomson parabola spectrometer (TPS)

The Thomson Parabola Spectrometer (TPS) is considered one of the most used and reliable charge particle detectors[198].
In figure 2.4, we illustrate a sketch of a typical Thomson parabola structure[2]. It consists of : 1) a pinhole, that has a typical size of few tens of μm [95, 94]; 2) a bending magnet[84, 165] for dispersing the particles in the direction perpendicular to the magnetic field according to their velocities, 3) a capacitor plate with field strengths (suitable to avoid breakdown or discharge) and that allow discriminating the particles' species and 4) Ion Detector (e.g., Micro Channel Plate (MCP), phosphor screen with CCD camera [95, 2]) (see figure 2.4).
In figure 2.4, we also introduce the reference system: the z axis represents the propagation direction (beam axis), both the magnetic field and electric field are directed on the x axis. The two fields are therefore parallel to each

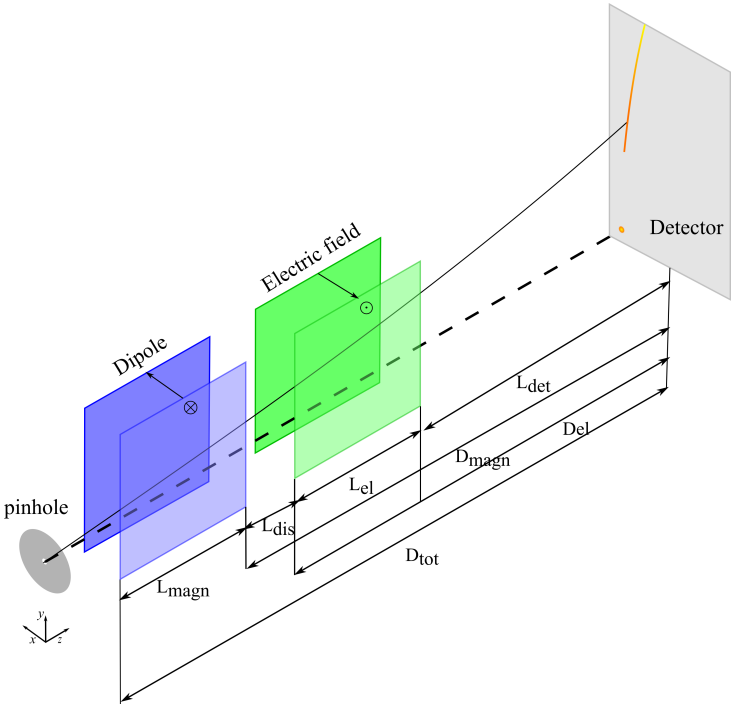

Figure 2.4: Thomson parabola spectrometer structure. It consists of a pinhole, a dipole, an electric field and an ion detector. Figure adapted from [2].

other and normal to the propagation direction.
The initial ion beam passes through the pinhole, then it is dispersed by the magnetic field, according to the particles' velocity due to the Lorentz's force. The static electric field, instead, allows to discriminate the multi-species particles of the source, according to ratio between charge and mass (q/m).
We report the main equations of the particles' motion, considering the magnetic and electric sections of a Thomson parabola spectrometer separated by the distance L_{dis} and use the reference system, illustrated in figure 2.4.
We refer for more details to appendix A in which we present all the calculation' steps.
The particle's motion (see figure 2.4), can be expressed by the following equations:

$$x = -\frac{qET_E^2}{2m_0} + L_{det}\tan(\beta)$$

$$y = \frac{v_0}{\omega}\left\{1 - \cos\left[\arcsin\left(\frac{L_{magn}\omega}{v_0}\right)\right] + 1\right\} + D_{tot}\tan\left[\arcsin\left(\frac{L_{magn}\omega}{v_0}\right)\right];$$

$$z = L_{magn} + L_{dis} + L_{el} + L_{det};$$

where q, m_0, v_0 are respectively the charge, the mass and the velocity of the ions (protons or carbon ions), E is the electric field value, B is the magnetic field, L_{magn}, L_{dis}, L_{el} and L_{det} are respectively the length of the magnetic field, the distance between the electric and magnetic sections, the length of the electric field and the distance between the electric field and the detector screen, ω is the ratio between qB and m_0, i.e ω=qB/m_0, T_E is the time related to the particle's motion inside the electric section which is linked to the time of the particle's motion inside the magnetic field T_B, by:

$$\begin{cases} T_E = \frac{L_{el}}{v_0 \cos(\omega T_B)}; \\ \\ T_B = \frac{1}{\omega} \arcsin(\frac{L_{magn}\omega}{v_0}) \end{cases} \tag{2.2}$$

Furthermore, $\tan(\beta)$ allows us to take into account the drift between the electric field and the detector and can be calculated as $\tan(\beta) = \frac{qEL_{el}}{m_0(v_0 \cos(\omega T_B))^2}$. The before mentioned equations can be expressed, using the small angle approximation and considering, as it is conventionally done, the magnetic and electric field in the same section.
The particles' deflections due to the electric field is directed on x, while the particles' deflection due to the magnetic fields is on y :

$$x = \frac{qEL_{el}^2}{2m_0 v_0^2} + \frac{qEL_{det}L_{el}}{m_0 v_0^2}; \tag{2.3}$$

$$y = \frac{qBL_{magn}^2}{2m_0 v_0} + \frac{qBL_{magn}D_{magn}}{m_0 v_0} \tag{2.4}$$

For not relativistic speeds ($v << c$), the kinetic energy E_{kin} is introduced and the previous equations 2.3 and 2.4 are further simplified. Hence, it is possible to obtain the commonly used equations:

$$x = \frac{qEL_{el}}{2E_{kin}} \left(L_{el}/2 + L_{det}\right); \tag{2.5}$$

$$y = \frac{qBL_{magn}}{\sqrt{2m_0 E_{kin}}} \left(L_{magn}/2 + D_{magn}\right) \tag{2.6}$$

These equations allow us to calculate the particle (ion) traces as follows:

$$y^2 = \frac{q}{m_0}\frac{B^2}{E}\frac{L_{magn}^2 \left(L_{magn}/2 + D_{magn}\right)^2}{L_{el}\left(L_{el}/2 + L_{det}\right)} x \tag{2.7}$$

According to the parameters of the TP and the particle species, the particle (ion) traces correspond to different parabolas (different charge/mass) on the

detector screen.
In the next section, we describe the different contributions for calculating the energy resolution of a TPS, whose details are relevant for chapter 4.

2.3.1 Thomson Parabola energy resolution

The main contributions for calculating the energy resolution of a TPS for a specific trace (protons or carbon ions) are geometrical. They are given by the drift length (L_{det} in figure 4.1), by the pinhole size and by the properties of the magnetic field, i.e. the strength B and length L_{magn} along the propagation direction (in our case z axis).
The intrinsic energy resolution $\Delta E_{kin}/E_{kin}$, in the not relativistic case, can be estimated as reported in [97]. In this case, it is obtained by calculating the energy range covered by the beam spot on the detector divided by its center energy:

$$\frac{\Delta E_{kin}}{E_{kin}} = \frac{2s}{y(1-(\frac{s}{2y})^2)^2} \approx \frac{2s}{y} \tag{2.8}$$

where s indicates the ion beam spot size on the detector and y is given by the equation 2.7. Its value depends on the pinhole size, the distance between the ion source and the pinhole and the distance between the pinhole and the detector [97].
The magnification of the particle source on the detector screen and the resulting spot size s are given by the ratio between the distance pinhole-to-detector L_1 (D_{tot} in figure 4.1) and the distance between the source-pinhole L_2, the diameter of the pinhole d and the source size x. Hence, the spot size s is calculated as:

$$s = d + \frac{L_2}{L_1}(d+x) \tag{2.9}$$

These distances are related to the geometry of the experimental setup, and in most of the cases, because d $\gg$ x, the equation 2.9 can be simplified to s $\approx$ d(1+ L_2/L_1), where the ratio L_2/L_1 indicates the magnification.
As it is known, the increase of both the strength and the length of the magnetic field increases the resolution, providing a higher dispersion (better separation between the particle energies), increasing the size of the pinhole d, instead, decreases the resolution because this is translated in an increase of the ion beam spot size on the detector screen.
It is possible to decrease the size of the pinhole and increase the drift L_{det}, but this can lead to a decrease in the ion flux. Therefore, usually, the increase of the resolution is mostly related to the features of the magnetic field, as discussed in the following references [97, 103, 194].

Regarding the electric section of the TPS, instead, the uncertainties are related to the separation of the traces of the ions (q/m) that belong to different species. We report the formula of the merging energy E_m of two neighbour ion signals having the charge q_i , from ref. [98]:

$$E_m = \frac{q_i E L_{el}(D_E + 0.5 L_{el})}{s R_Q} \tag{2.10}$$

where $R_Q = Q_1 + Q_2/Q_1 - Q_2$ where $Q_1 = q_1/m_1 > Q_2$ [98]. It is clear from the equation 2.10, that, in this case, the energy merging of two ion species is related to the electric field parameters (length and strength), the drift is to the detector D_E and the pinhole size s. According to equation 2.10, three different options can be considered in order to increase the resolution: (1) increase the length of the electric field [36], (2) increase the strength of the electric field and (3) increase the drift D_E.
There have been in the last decades, numerous research groups[36, 81, 1], that have modified the original TPS, starting from the considerations mentioned before. The context and state of the art regarding the TPS modifications will be further presented, in detail, in chapter 4 that deals with a novel spectrometer for laser ion diagnostics.
TPS are usually employed with numerous types of detectors, such as image plates (IPs) [134], CR-39[94], MCP[213] and/or combinations of them[121, 95, 128], whose features will be reported and summarized in the following sections.
Although some of them allow obtaining a raw ion spectrum, starting from the signal of the detector, an absolute calibration is needed in order to retrieve in a proper way the proton and ion spectra, such as was described in the case of the RCFs (see section 2.2.1).

2.4 Micro Channel Plate (MCP)

The micro-channel plates (MCP)[213] are closely linked to an electron multiplier. They are sensitive to many types of radiation (photons, electrons and ions).
They are matrices of thin glass capillaries with diameter from 4 to 25 μm , fused and sliced into thin plates, with typical thickness from few hundreds of microns up to few tens of millimeters [22]. A scheme of the structure of a MCP is illustrated in figure 2.5.
A primary charged particle or photon can interact with the channel wall, generating secondary electrons. The number of the secondary electrons is amplified in subsequent collisions with the channel wall, while drifting in an

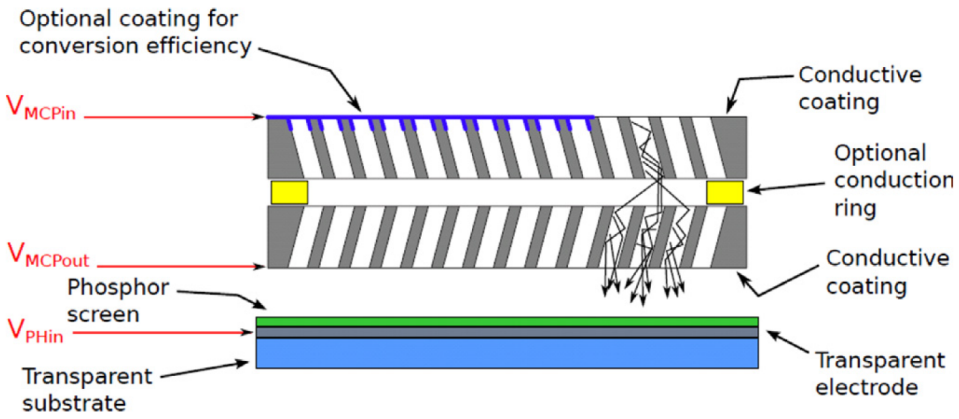

Figure 2.5: Image of the structure of a micro channel plates. Figure extracted from [22].

electric field applied between the front and the back sides of the MCP (see figure 2.5). The final electron charge that exits the back of the surface of the MCP, is drifted to a phosphor screen, where the electrons are converted to photons, which are collected by a camera system.
Many factors such as the thickness of the plates, the angle between the channel axis and MCP surface (typically between 4° to 12° [22]), the value of the drift of the electric field and the channel coating material, contribute to the overall amplification in a single channel of one plate.
The spatial resolution of a single plate mainly depends on the capillary diameter, which has a size of a few μm.
MCP can be used, due to their sensitivity, for the detection of different types of particles and/or photons. In a laser driven ion experiment, they are usually implemented with magnetic and electric spectrometers, such as TPS, in order both to allow to distinguish the desired ion signals compared to unwanted ones, as well as to avoid the saturation of the detector.
An adequate calibration is needed for the ion counting with an MCP detector. Calibration measurements can be done with conventional particle accelerators, such as it was done for the RCFs calibration, described in section 2.2. Otherwise, the comparison of the MCP signal with a known calibrated detector, such as slotted CR-39 [95, 128], can be used. We describe, in the following sections, the details of the calibration method in which slotted CR-39 is used in combination with an MCP plate. The main advantage of the MCPs is that, compared to the other passive detectors, they allow ion online measurements of the ion, without post-processing.
Therefore, they are considered suitable for high repetition rate systems. How-

ever, they are sensitive to electromagnetic noises, more expensive and require high vacuum conditions (10^{-6}-10^{-7} mbar).

2.5 Image plates

Image plate detectors were originally developed and used as diagnostics for X-ray medical imaging systems [134]. However, within the last decades, they have become a useful diagnostic, usually implemented after a magnetic spectrometer in LDIA [205, 9, 121].

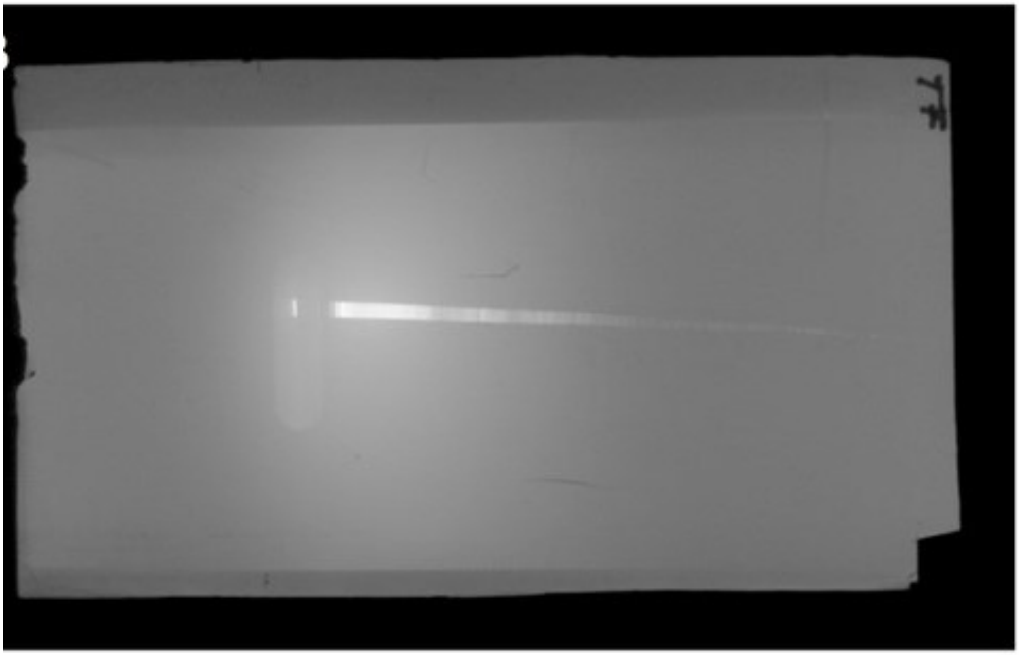

Figure 2.6: Picture of the scan of an image plates, located after a magnetic spectrometer. In this case, it is clearly visible the sign of the slit that represents the reference point and the trace of the proton deflected by the magnetic field. Figure reported from [205].

They are sensitive to a broad range of radiations, such as UV, ions, electrons, gamma rays, etc. They are usually reusable detectors commercially available by Fuji-film and are categorized as BAS-SR (high resolution), BAS-MS (high sensitivity) and BAS-TR (used also for tritium ^{3}H detection) [134].
They are film-like radiation image sensors, that have, as active component phosphor crystalline BaFBr:Eu^{2+}, coated onto a support layer. They work, absorbing the energy of the incident radiation (X-rays or charged particles)

and exciting electrons of the Europium (active layer) into the metastable state.
The latent and stored energy can be retrieved by photo stimulating the metastable excited state using a scanning laser beam at a visible wavelength. This is done using commercial scanners, typically designed for medical purposes.
The energy released by the photo-stimulation is emitted in form of light that is collected and amplified by a photo-multiplier and converted to an electric signal which is then digitized, leading to a photo-stimulated luminescence value (PSL) for each pixel. IPs have a good spatial resolution, usually set by the scanning system used for the PSL, that it is typically 25 μm and 50 μm per pixel.
When all the metastable states decay, the signal disappears. Thus, one disadvantage is their fading time after which information loss can happen. Hence, it is important to scan them after the exposure within few tens of minutes[121, 96, 9].
This also means that they can be reused after erasing the signal. This is usually done by scanning them multiple times or exposing them to a uniform, intense visible light.
Another advantage is their insensitivity to EM noise. They also are also versatile as radiation detectors because of their sensitivity to a wide range of emissions (X-rays, electrons and ions). As a consequence, they can be used in combination with numerous diagnostics, such as X-ray spectroscopy [16] or a TPS spectrometer[121]. For example, the use of BAS-TR type as a detector for X-ray spectroscopy is described in detail in chapter 6, which deals with the applications of laser driven proton beam for cultural heritage [16].
However, this sensitivity can be also seen as a disadvantage because in some cases it makes it difficult to distinguish the signal of interest and they are also sensitive to the ambient light, such as in the case of the RCFs.
In figure 2.6 it is reported a scanned image of an IP BAS-TR type, used as diagnostic and implemented, after a magnetic spectrometer in the experiment of ref. [205].
As previously described for the case of the RCF films (see section 2.2.1), a calibration procedure is needed in order to obtain the final energy spectra, i.e final correspondence between the number of protons/MeV vs energy. I participated in the elaboration of a Matlab routine code described in ref. [205] for the BAS-TR IPs calibration.
The PSL information stored in the IPs is obtained, using the following for-

mula, starting from the raw data (QL):

$$PSL = (\frac{p}{100})^2 \frac{4000}{s} 10^5 (\frac{GV}{2^{bits}} - 0.5) \tag{2.11}$$

where s, which indicates sensitivity and p, which indicates pixel size, both depend on the scanner features. We can also convert the pixel information in μm, taking into account the spatial resolution of the scanner, which typically is few tens of μm. After this step, for calibrating the dispersion of the magnetic spectrometer, multiple shots on the target, that was 15 μm of gold [205], were taken, putting different low energy cutoff filters (i.e Al plates of varying thickness ranging from few tens of μm up to 1 mm) directly in front of the IPs.

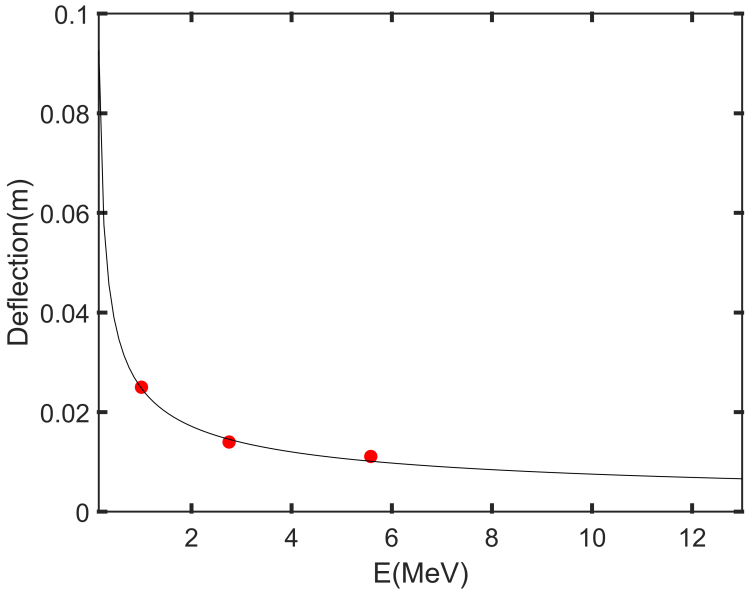

Figure 2.7: Fit of the analytical calculations (see eq. A.24) for the magnetic spectrometer.

We can choose the thickness of the filters, using the SRIM program [223] or tables in which the energy cutoff values are recorded according to the different types of radiation [9](in this case protons). In the experiment of ref. [205], we choose Al filters of thickness of 15 μm, 77.5 μm and 253 μm for stopping respectively $\sim$ 1 MeV, 3 MeV and 6 MeV. This enables to determine the position on the IP of the lowest energy protons.
Comparing these positions with the analytical formula of proton deflection proton in the magnetic field and knowing the features of the experimental

setup (see equation A.24), that are $L_{magn} \sim 0.071$ m, $L_{dis} \sim 0.04$ m and B=0.64 T, it is possible to retrieve the correspondence between the position of the signal on the IP and the incident proton energy, i.e. the dispersion curve of the spectrometer, as reported in figure 2.7. Then, we use the spatial resolution conversion for the pixels and the interpolation with the dispersion curve of the magnetic spectrometer to find the correspondence between PSL and energy (horizontal calibration). We measured two final spectra dN/MeV/ster (proton/MeV/ster) vs E(MeV), using the calibration curve (see figure 2.7), the fitting functions of ref. [121] and the solid angle, that has been calculated according to the geometry of the experimental setup. More details can be found in ref. [205].
The next step is to find the correspondence between the signal on the IP and numbers of protons (vertical calibration). This is usually done, using different fitting functions, such as the ones reported in ref. [121], in which other types of detectors (RCF) have been used as reference (see section 2.2.1).

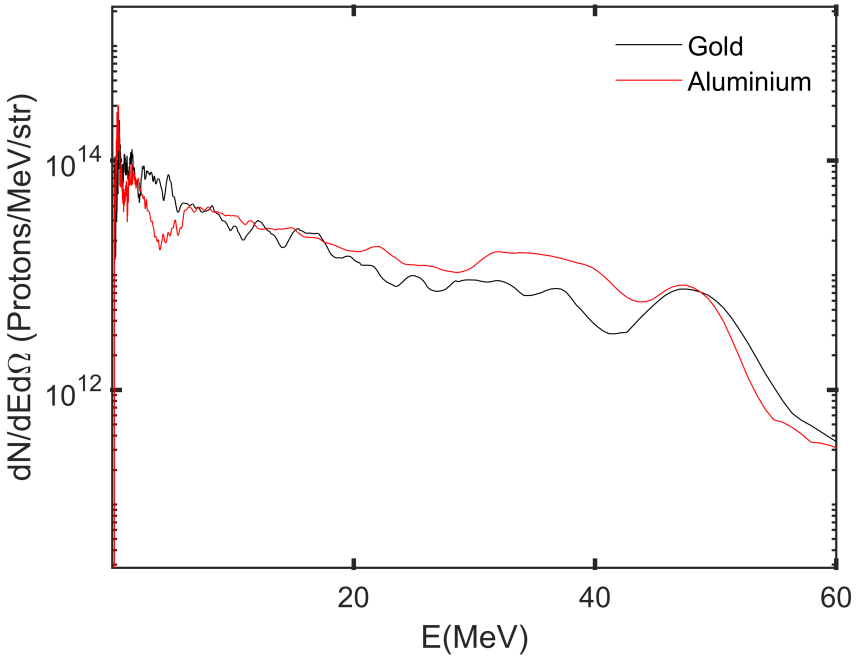

Figure 2.8: Proton spectra obtained by the interaction of 230 J, 700 fs Jupiter laser with 15 μm gold target (black) and 15 μm aluminum target (red). Energy cutoff is around 52 MeV for Al and 55 MeV for Au, similar to what is reported at Trident, a laser that has a comparable scale in terms of energy per pulse and pulse duration[64]. Figure re-adapted from [205].

The fitting function FIT(E)= PSL(E)/number of protons (E) is then derived, in this case, for the proton energy range between 5 and 20 MeV [121]. The IP calibration curve can be obtained for various particle sources. They allow to correlate a PSL value to the particle number N for a given energy E (PSL/N=f(E)) and enable to obtain the final particle spectra.
We reproduced the same spectra results, that we published in ref. [205], obtained from the described spectra analysis. We measured two final spectra dN/MeV/ster (proton/MeV/ster) vs E(MeV), using the calibration curve (see figure 2.7), the fitting functions of ref. [121] and the solid angle, that has been calculated according to the geometry of the experimental setup. More details can be found in ref. [205].
Proton spectra obtained with 15 μm gold target (black) and 15 μm aluminum target (red) using the Jupiter laser with the energy of 230 J per shot with a pulse duration of 700 fs are shown in figure 2.8.

2.6 CR-39

CR-39 (i.e Columbia Resin #39) or polyallyl diglycol carbonate, is a plastic polymer with chemical formula $C_{12}H_{18}O_7$. It is widely used as a solid-state nuclear track detector and it is typically employed after the TPS, in combination with other detectors such as microchannel plates [95, 128] and/or Image plate [121, 134].
CR-39 has the advantage, compared to the other detectors, to be insensitive to X-rays, photons and electrons, therefore, it allows the detection of different types of ions, including protons and heavy ions. CR-39 is also not affected by electromagnetic pulses.
It is usually manufactured with a thickness of 1 mm, which is sufficient to detect protons up to 10-11 MeV and carbon ions up to 15 MeV [223]. Above the aforementioned energies, it becomes transparent, respectively to protons and carbon ions.
CR-39 provides single particle detection through the latent tracks left on the plastic material because of the interaction with the incident ions, that break the molecular structures and damage the plates. After the beam irradiation, the latent tracks in CR-39 are revealed through an etching procedure in a caustic alkaline solution, which is typically sodium hydroxide (Na-OH).
During this etching process, the damaged parts dissolve faster than the unaffected surrounding material, making accessible the single particle information in observable pits[63].
CR-39 has to be carefully exposed to the etching for the appropriate time in order to avoid over etched and/or exposition, where the single ion impact

(pitch) cannot be counted anymore. The limit factor is given by the pit density, that if it is too high can compromise the detection, creating overlapping or if it is too low, it impedes to distinguish the signal from the background. After the etching procedure, ion tracks can be read out by an optical microscope. The microscope allows to scan the CR-39 in a defined area with the chosen magnification (see figure 2.9).

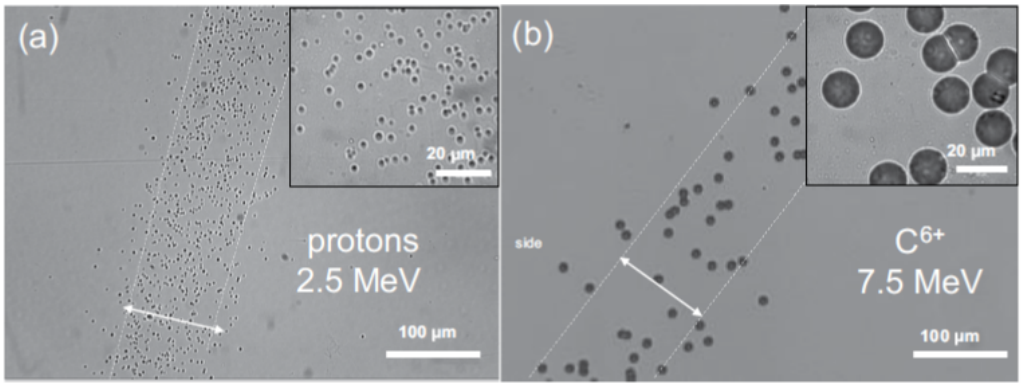

Figure 2.9: Microscopic images of the ion traces with magnification 20x have been used for detecting (a) protons with energy 2.5 MeV and (b) ions with energy 7.5 MeV. The distance between the white dashed line is equivalent to the pinhole size. The inset images have a magnification of 100x. Figure reported from [94].

The zoomed microscope images allow to distinguish the different types of species based on the geometry of the pits (dimension and shape) and the particle energy as well as to count the absolute number of particles that interact with the plate.
As an example of CR-39 analysis, we reported the experimental results of ref.[94], in which a methodological approach for characterizing the track formation on the surfaces of CR-39, has been used. Further details are presented in ref. [94].
In figure 2.9, microscope images (20x magnification) of protons with energy 2.5 MeV and carbon C^{6+} with energy 7.5 MeV are shown[94]. The details of the insets clearly show the difference between the size of the pits of the proton, that is $\sim 2\mu$m, with respect to the size of the pits of the carbon ions C^{6+}, that is around $\sim 18\mu$m.
Furthermore, the use of Atomic Force Microscopy (AFM), instead of an optical microscope, has been also proposed for a more precise and high accurate analysis of the tracks [100].

Despite its insensitivity to electrons and photons, CR-39 can be used only once. Therefore it needs to be replaced for new measurements and doesn't provide real-time measurement. It needs a complex and elaborated post-processing (in some cases multiple etching is needed for ions stopped deeply in the CR-39). For all the mentioned reasons, they are not easily usable for a day-by-day ion characterization, as well as not suitable for laser systems with high repetition rates.

2.7 Absolute calibration for MCP assembly with a TPS

The absolute calibration of the detectors is important for characterizing the laser driven ion spectra.
In this section, we describe the absolute calibration procedure of a detection system, that includes an MCP, used in combination with a TPS and slotted CR-39 [95].
The calibration curve, similarly to the IPs, has been found, starting from the parabola ion traces detected simultaneously on the MCP and CR-39. The signal recorded by the CCD camera in the region between the stripes of the CR-39 was compared with the number of particles counted on the CR-39 stripes after the etching procedure. Furthermore, the relative calibration was done by considering the correlation between the CCD integrated counts and the numbers of particles on the adjacent CR-39 stripes, assuming that they belong to the same ion traces.
The energy calibration of the segmented ion traces, thus, was elaborated using Matlab routines and using the features of the experimental setup (geometry). Hence, the calibration factors have been obtained by dividing the MCP fitting function curves to the ones of the CR-39.
Their values can be applied to the sum of the pixel values across the ion traces for every energy to produce an absolute number of particles, using a procedure similar to the one of the IPs (see section 2.5). By knowing the experimental setup it is possible to calculate the value of the solid angle, i.e produce the calibrated spectrum in number of particle/ MeV steradian.
We report, as an example of this calibration procedure, the details of the first experiment, in which this assembly has been implemented [95].
The laser driven ion sources were generated using the Ti: Sa laser beam of the Center for Relativistic Laser Science (CoReLS) [220, 95] that has laser energy of $\sim$ 14 J, laser pulse 30 fs. The laser pulse was focused with an off-axis parabola f/3 onto Al targets with thickness 0.4 μm with the intensity of

$\sim 2 \times 10^{20}$ W/cm^2 and angle of incidence of 30° to the target normal. The scheme of the experimental setup is shown in figure 2.10, reported from [95].

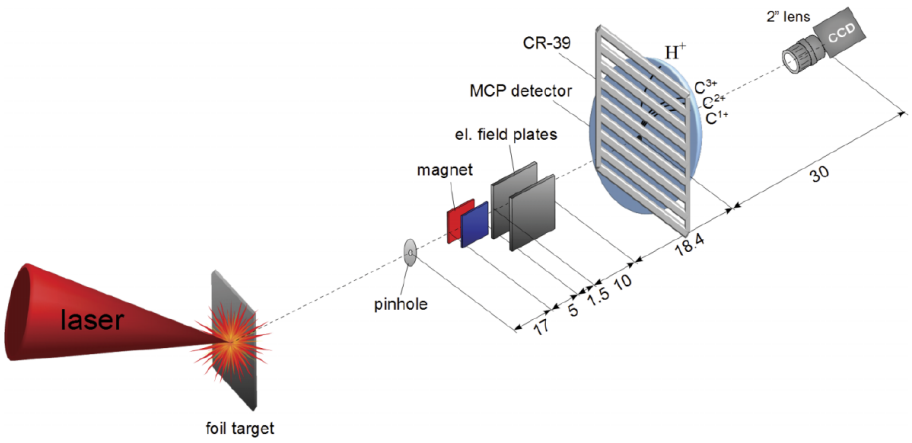

Figure 2.10: Experimental setup scheme: the distance between the elements that compose the detection system is in cm units. It includes a TPS assembled with an MCP detector and slotted CR-39. Figure extracted from [95].

We focus our attention on the detection system. It is composed of a TPS with an ion pinhole of size 100 μm, a magnetic field of B= (0.9 $\pm$ 0.1 T) and an electric field of 22 kV/cm. The length of the magnetic field is 5 cm, while the length of the electric field is 10 cm. The two fields are separated by a distance of 1.5 cm. The drift between the exit from the electric field to the detector is 18.4 cm. The MCP detector is coupled with a phosphor screen and imaged onto the CCD camera. As it can be seen from figure 2.10, slotted CR-39 plates in double or single layer configuration were installed in front of the MCP.
For calibration purposes, the comparison was between three consecutive shots for the CR-39 and one shot for the MCP, due to the use of a small pinhole (high TPS resolution) that can reduce the numbers of observable particles.
In this experiment, the proton calibration was of particular interest in the energy range between 10 and 12.3 MeV, because the stopping range of the protons [223] with $E_{prot} > 10$ MeV is larger than the thickness of the CR-39 plate.
Most of the low energy protons $E_{prot} < 4$ MeV are stopped by the first CR-39 plate, while in the energy range between 10 MeV $< E_{prot} <$ 12.3 MeV, the use of two CR-39 plates was used. In detail, the formation of pits of equal

amounts was observed on the rear of the first CR-39 and the front of the second CR-39 plate. This result indicated that, although the first layer is not able to stop the protons, the energy deposited is still enough for creating the pits on the second CR-39. Furthermore, particles that create the pits on the first CR-39 are slowed down and are fully stopped in the second CR-39 layer. Therefore, in this transition between the CR-39 plates, each proton creates a pit in both of the CR-39 layers. Hence, for the calibration procedure, the protons that are slowed down due to the passage inside the CR-39 cannot be assigned to the MCP calibration at high energies. However, they can be used as confirmation of the counts of the particles, i.e. calibration in that particular interval.
For the higher proton energy range $E_{prot} > 18$ MeV the CR-39 becomes transparent to the signal, while the MCP detector, although the thickness of the detector is smaller than the stopping power of the particles (0.6 mm), recorded a sufficient signal for this particular part of the spectra.
In ref. [95] a good agreement between the experimental data with a theoretical model of ref. [160] has been found for the calibration factors.
This allowed measuring the response of the MCP (counts/particles) both for protons with an energy range between 2 MeV and 17.8 MeV and for the carbon ions with an energy range between 5 and 58 MeV [95].
The limit of this calibration procedure is given by the stopping power of the particles (protons or ions) that can be larger than the thickness of the detectors. However, it is possible to overcome it and extend the analyzed energy range, using e.g multiple CR-39 stacks.
Recently, the same calibration procedure of MCP assembly with TPS and slotted CR-39 of ref. [160, 95] has been used for carbon 6+. In this case, [128], the response of the MCP was measured for absolute numbers per steradians for carbons up to 21 MeV/nucleon, i.e 252 MeV.

2.8 Summary and conclusions

In this chapter, we summarized the main features of the widely used laser driven ion beam diagnostics.
In the different sections, we reported the structure, the advantages and the disadvantages and described the use of RCFs, MCP, CR-39, TPS and IPs in LDPA. Some of them can be used in a stack arrangement, such as RCFs and CR-39, or, for example, in the case of IP and CR-39, in combination with a TPS.
In these experiments, most of these detectors are passive and need post-processing procedures, after breaking the vacuum condition. Furthermore,

in some cases, they have to be replaced for each measurement. The MCPs are considered, instead, the most favorable detectors for the upcoming high repetition rate high intensity laser systems, because they can provide real-time measurements.
Absolute calibration curve has been derived, using IP coupled with a magnetic spectrometer (see section 2.5), as well as using the assembly MCP, slotted CR-39 with TPS (see section 2.7).
My contributions for papers I and II are reported in sections 2.2 and 2.5, emphasizing the RCF and IP calibration measurements. At current, calibration for these detectors exists up to few tens of MeV for the protons [95, 121] or heavy ions[95, 128].
We also described in detail the features and the equations of the particles' motion inside a TPS, because they provide useful indications for the model system, presented in chapter 4, in which the design and the optimization of a novel spectrometer have been studied and proposed.

Chapter 3

Ion acceleration driven by multi-TW-few-cycles laser pulses

The chapter deals with the details and the measurements performed during an experimental campaign, in which low energy laser driven ion accelerated beams have been observed. By low energy ion beams, in this case, we indicate laser driven ion beams with a maximum energy of a few hundreds of keV.
The possibility to generate such beams with TW-milli-joule-ultra-short lasers and with increasing repetition rate (even up to kHz range) have boosted a great deal of attention in many applications, such as precise energy-loss measurements in plasmas[37], taking advantage of the stopping power of the protons, that have the Bragg peak (see chapter 2), diagnostic for cultural heritage (CH) [16, 17, 154], potential laser driven isotope generation for positron emission tomography (PET)[49], injectors for conventional accelerator machines, e.g the Laser Ion Generation, Handling and Transport (LIGHT) collaboration[71] or the high intensity proton injector for the International accelerator Facility for Antiproton and Ion Research (FAIR) [19] that have been both installed at GSI. Sequences of solenoids and RF cavity that compose laser driven transport beamline and post-acceleration schemes, that will be detailed presented in chapter 5, allow delivering bright and intense proton bunches in the sub-nanosecond scale for investigating proton imaging applications[93] and manipulate, inject and post-accelerate a few MeV laser proton beams into LINAC to increase their energies up to a few tens of MeV [7, 8, 19].
It has stimulated interest in the production of short neutron bursts driven by laser accelerated light ions, i.e. compact laser neutron sources[101], and

a novel concept for the design of a neutron source for a laser-based transmutator [110]. The combined use of thin target, single or few-cycle laser pulses (Coherent Acceleration of Ion by Laser (CAIL) Scheme), as reported in [222], has been proposed and can represent an efficient way to improve the laser energy to deuterium energy conversion (interaction laser-deuterated targets) that is translated in efficient generation of neutrons (few MeV) with the accelerated deuterons via deuterium-deuterium (DD) fusion. Hence, a high yield of neutron generation can be potentially obtained with ultra-short-high-repetition rate-low energy laser systems[110].
However, the upcoming generation of high repetition rate TW (or even PW) laser systems brings new challenges in terms of the target design. Several types of solutions, including liquid targets [138], rotating tape [129, 149] and cryogenic targets [104] have been implemented.
Morrison et al.[138], recently, have used liquid targets and have measured for the first time the acceleration of $\leq$2 MeV protons at kHz repetition rate with a sub-TW milli-joule laser.
During this experimental campaign, the laser driven ion acceleration has been investigated in the same low energy range of Morrison et al.[138]. It is a pilot experiment of a neutron generation project for laser-transmutator. For more details we refer to [110, 222]. The laser driven ion beams have been generated, using in a single-shot mode, the SYLOS Experimental Alignment (SEA) laser (few-cycle laser system), hosted by ELI-ALPS facility [212]. It can provide a maximum of 42 mJ pulse energy and sub-13 fs pulse duration at a repetition rate, either in a single shot or 10 Hz repetition rate.[202, 26, 190].
This chapter is organized as follows: first, we describe the experimental setup (see section 3.1), including a brief description of the Off-Axis Parabola (OAP) alignment procedure and the imaging systems, both for the focal spot size and the target surface. In the experiment method (see section 3.2), we measure the focal spot size and derive the laser peak intensity. Furthermore, we describe the diagnostics used for proton detection and show one of the proton spectra obtained. In the end, we summarize the obtained results, taking into account that the experiment data analysis is still ongoing.

3.1 Experimental setup

The experiment has been performed, using the SEA laser, installed at ELI-ALPS research center, Szeged (Hungary) [202, 212]. The experimental arrangement is illustrated in figure 3.1 with a photograph of the setup in figure 3.2.
The input laser pulse has the following parameters: p-polarization, duration

of 11 fs, central wavelength 850 nm, max 36 mJ and a beam profile that is super-Gaussian of order 6 of 5 cm diameter FWHM. More details can be found in ref. [202].

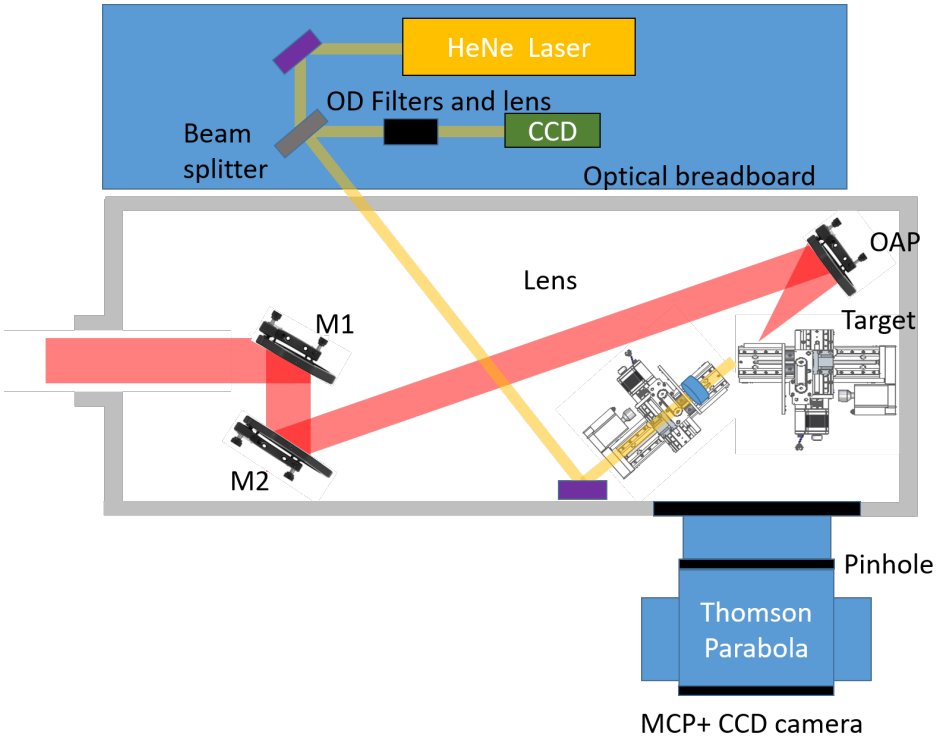

Figure 3.1: Experimental setup in the interaction chamber. The red thick lines represent the laser beam path and the yellow ones represent the imaging systems, both for the focus and the target.

The laser was operated in single-shot mode, achieved by means of a fast mechanical shutter, located inside the laser (the laser amplification stage). The beam is focused with an off-axis parabolic mirror (OAP) with an angle of 22.5 degrees and a focal distance of 15 cm (f/2.5) on targets such as Aluminium (Al), Carbon (C), Diamond-like Carbon (DLC) and plastic foil (CH) from few nm up to maximum 9 μm.
The red lines of figure 3.1 represent the laser path. The incoming beam is reflected by the first mirror (M1) to the second one (M2) and then directed to the OAP which focuses it.
Upon the interaction of the intense laser pulse with the air, the ionization process happens and the plasma is generated (see section 1.2.1).
The main nonlinear effect of interest, in this case, is self phase modulation (SPM), which broadens the spectrum. In the case of perfect alignment, SPM

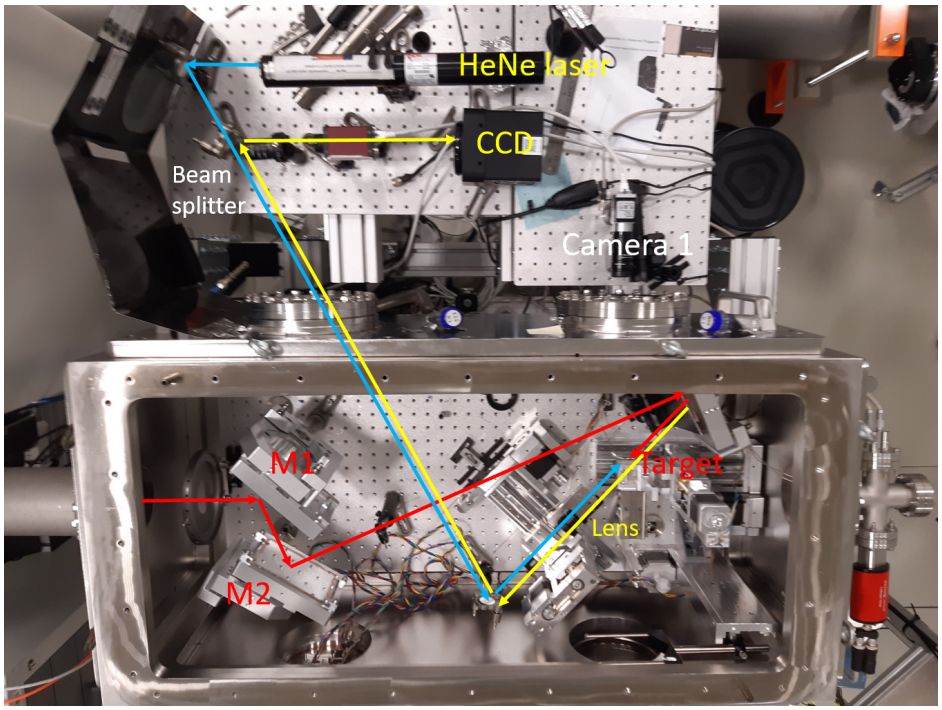

Figure 3.2: Picture of the experimental setup. The red lines represent the laser path, the blue lines represent the target illumination and the yellow lines represent the imaging system.

will lead to the generation of white light that can be visible on a screen. If now the OAP is misaligned, the intensity distribution will be distorted by aberrations. In our case, this distortion manifests by the appearance of a blue and red circle on the screen. When these two circles are made to be concentric by tweaking the parabola, the aberrations are minimized and the different wavelengths are properly superposed.[55]. Therefore, the OAP is properly aligned.
The laser focal spot is then monitored in the far-field on an 8 bit CCD camera (Manta Camera)[210], using an imaging system as illustrated by the yellow lines of figure 3.2. We find the proper focal plane position by scanning the image plane, that corresponds to the smallest and brightest laser focal spot image on the CCD. Taking advantage of the same imaging system [187], the target is positioned by using a HeNe laser and a beam splitter. The target surface is illuminated, as illustrated by the blue lines of figure 3.2. The backside reflection of the target surface is monitored on the CCD camera to be in the same image plane as to the focal plane position [187]. Hence, the focal and target imaging systems, allow us to obtain the best laser-target

interaction condition to generate low energy laser driven ion beams.
A Thomson parabola spectrometer (TPS) assembly with an MCP and slotted CR-39 is implemented [95, 128]. More details on it are presented in section 3.2.2, while in the next section, we measure the focal spot size and the laser peak intensity.

3.2 Experimental method

3.2.1 Measurement of the focal spot and intensity

In this section, we evaluate the laser focal spot size, starting from one of the CCD focus images in vacuum condition. An image of the focal spot is presented in figure 3.3. This measurement plays an important role in characterizing the focused beam and optimization of the OAP alignment.

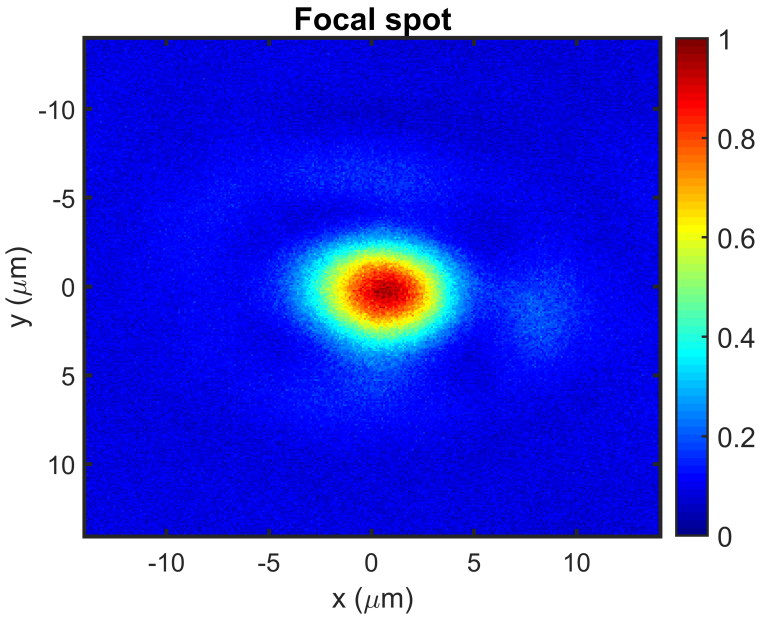

Figure 3.3: Focal spot image recorded in vacuum condition and centered on zero. Both the x and y axes are in μm units.

The background signal has been calculated, taking as reference a part of figure 3.3, in which the main signal is absent. After that, we normalized it, as it can be seen from the color bar. The x and y axis are converted from pixel to μm, according to the camera specification (1 pixel = 4.65 μm) and the magnification of the imaging system, that is $\sim$50 (see figure 3.2).
After the background subtraction and the normalization, we take both the

x and the y lineouts. The obtained curves are fitted with a Gaussian beam profile in order to measure the Full Width at Half Maximum (FWHM) focal spot size.
The parametric expression used for the fit Gaussian beam profile is[55]:

$$y(x) = a + be^{-2\ln 2\frac{(x-c)^2}{d^2}} \tag{3.1}$$

The comparison between the Gaussian fit and the x lineout is shown in figure 3.4.

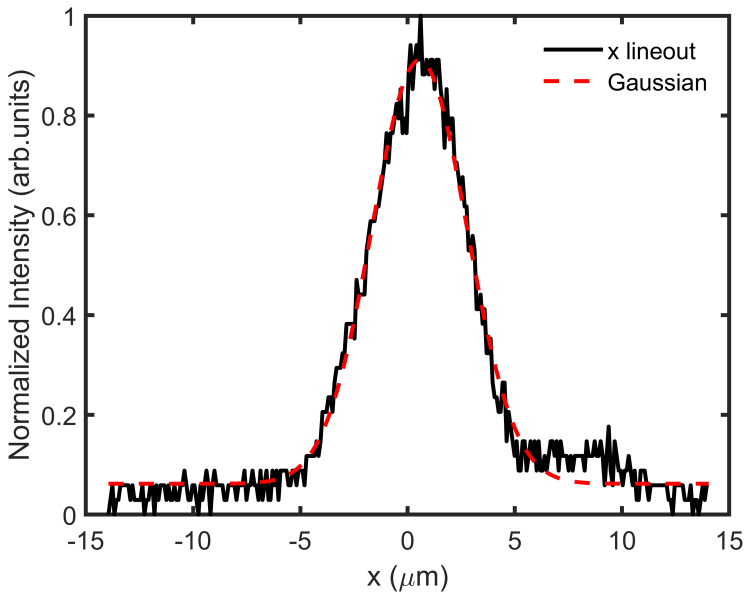

Figure 3.4: Fit of the x lineout with a Gaussian curve. The x axis is μm unity, while the y axis is in arbitrary units (arb. units).

.

The black line of figure 3.4 is the x lineout, while the dashed red line is the Gaussian fitting function. The fitting parameters a, b, c, d allow us to retrieve information about the amplitude, the offset and the FWHM.
Hence, the focal spot size is around ~ 5.19 μm, as can be seen from figure 3.4. The same value has been obtained with the y lineout of figure 3.3, thereby only x lineout is shown for reference. The Rayleigh range is around 30 μm. The focal spot size value for a Gaussian beam can be used to estimate the peak laser intensity achievable, according to the following[55]:

$$I_0 \approx \frac{2 \cdot E_l}{A \cdot \tau} \tag{3.2}$$

where E_l is the laser energy, τ is the laser pulse duration and A is the surface calculated as $A = \pi \cdot (d/2)^2$, where d is the focal spot size.
In order to properly evaluate the laser peak intensity, we consider different circles, i.e different areas, as references for our calculations, as shown in figure 3.5. This analysis provides us an indication of the uncertainties related to the laser intensity.
The intensity values on the right-hand side plot of figure 3.5 are calculated, keeping constant E_l, τ_l and A. Furthermore, they show that the intensity value decrease linearly, increasing the detectable area, i.e circle size.
This trend is due to a percentage value, estimated as the ratio between the area above the FWHM, compared to the total area evaluated for different areas. The percentage values are then, used in eq. 3.2, assuming that E_l=36 mJ, τ= 11 fs and $A = \pi \cdot (d/2)^2$, where d= 5.19 μm.
Ideally, the maximum laser intensity peak value is I= 2.1 $\cdot$ 10^{19} W/cm^2, replacing the laser energy, the laser pulse duration, and area values in eq. 3.2.

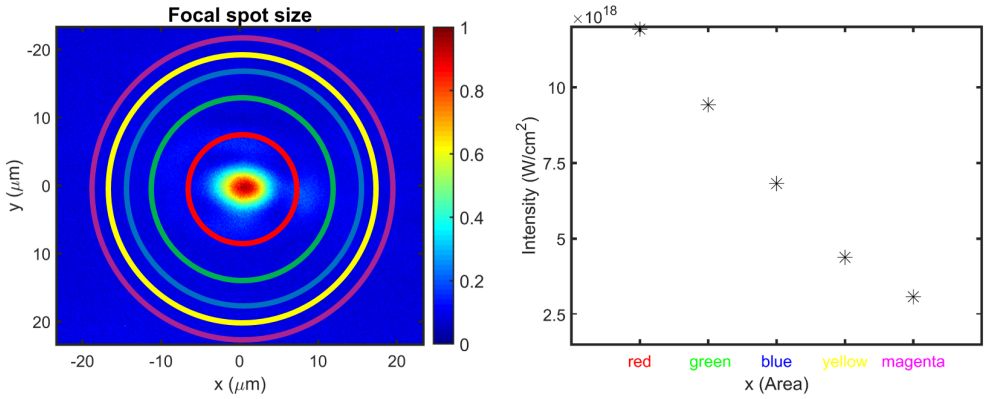

Figure 3.5: Correspondence between the different reference circles and the intensity measurements.

.

However, there are multiple factors, such as the effective detector area, the background signal, the dynamic range of the detector itself, that intrinsically are involved in measurement procedures. We mainly want to emphasize, in this case, the uncertainties related to the unknown "a priori" correct detection area.

3.2.2 Proton spectrum

In this section, we describe the detection system and report one of the laser proton spectra, measured during the low energy ion acceleration (LEIA) ex-

perimental campaign.

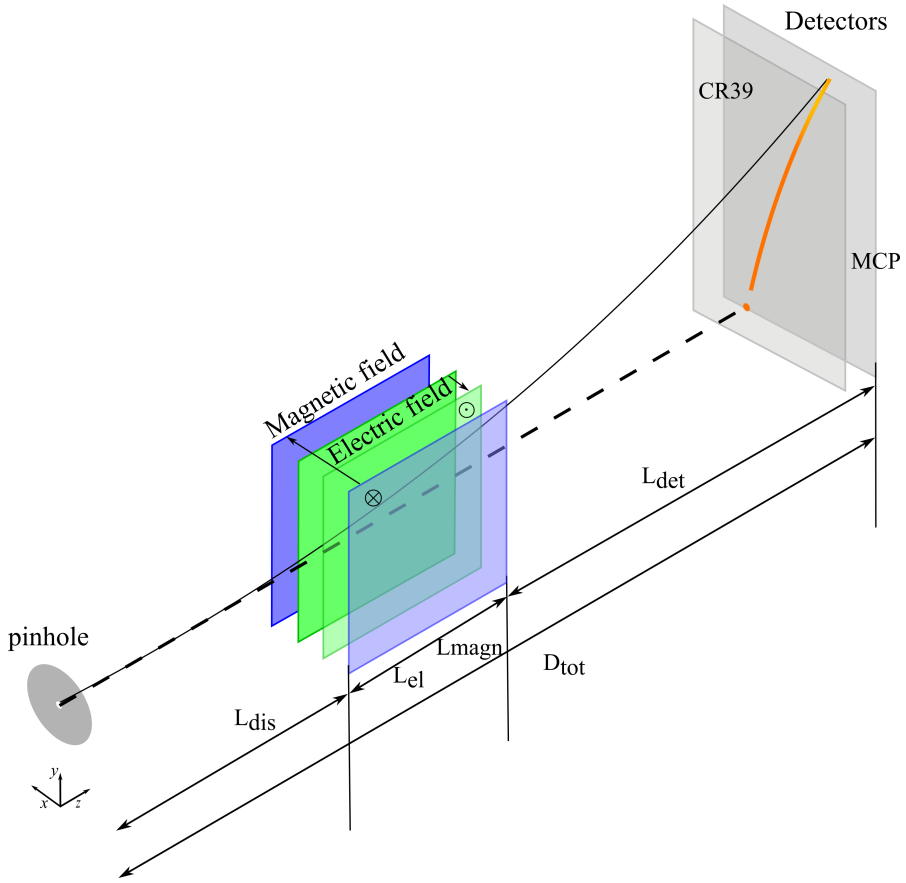

Figure 3.6: Scheme of the TPS used during the LEIA experimental campaign. It has the combination of both fields in a single region, and the use of a CR-39 detector for vertical calibration of the spectrometer.

.

A scheme of the detection system is presented in figure 3.6. As diagnostics, a Thomson Parabola spectrometer [36, 85, 198] (see chapter 2 and appendix A) for measuring the ions' energies has been used. The particles' energies have been detected with the assembly TP, slotted CR-39, MCP of a diameter of 8 cm, phosphor screen, and a CCD camera. This particular combination has been described in chapter 2.
The detection system has a pinhole with a size of 200 μm, magnetic and electric fields that are combined and have length $L_{el} = L_{magn}$= 5 cm. The magnetic field is B $\approx$ 0.27 T, while the electric field E = 2.61 kV/cm. The distance between the pinhole and the entrance to the TPS is L_{dis}= 26 cm, whereas the distance between the laser (source) and the pinhole is 58 cm.

The MCP and slotted CR-39 are represented in figure 3.6 by two grey rectangles. The distance between the TPS and the detectors is L_{det}=8.8 cm. The features of the detection system (e.g magnetic, electric field, etc..), that compose the TPS, determine the ions' traces on the detector.
The laser ion beams have been generated, using different types of targets such Al, C, DLC and CH with thickness, that goes from a few nm up to 9 μm.
We report one of the laser driven proton beam spectrum in figure 3.7. It was obtained in a single shot with laser energy of 36 mJ, pulse duration of 11 fs and an aluminum foil with a thickness of 9 μm.

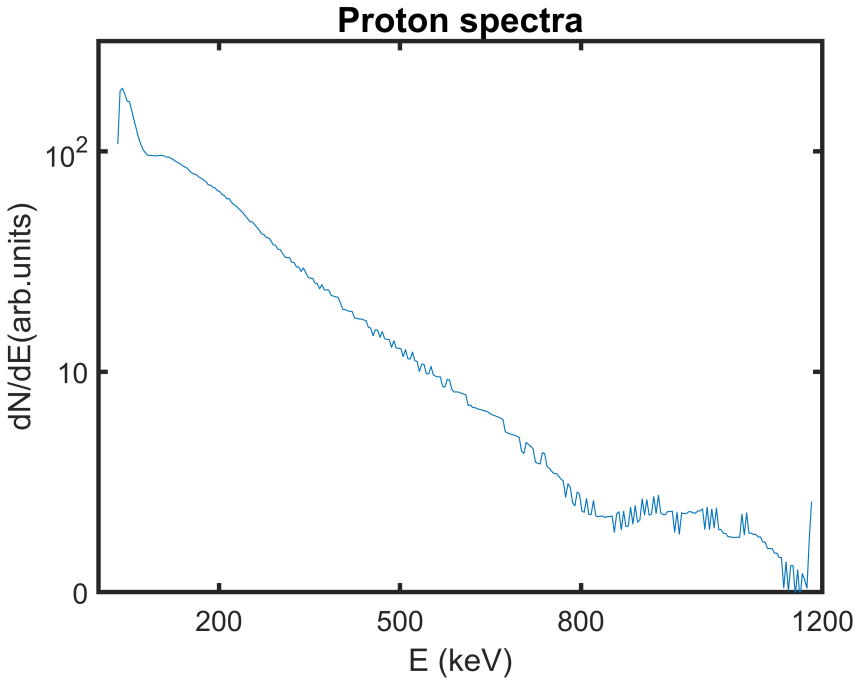

Figure 3.7: Proton energy spectrum; The x axis is in keV unity, while the y axis is in arbitrary units. The typical decreasing trend of laser driven proton beams is shown.

The calibration method used for the proton spectra of figure 3.7 has been explained in chapter 2. The proton spectrum is measured in arbitrary units (arb. units) and has only the horizontal calibration related to the geometry of the experimental setup (see figure 3.6). The vertical calibration is calculated, using the correspondence of the numbers of particles between the MCP and the slotted CR-39 [95] and is a work in progress.
The proton spectrum has the typical decreasing trend of laser proton beams

and provides us an indication of the maximum proton energy cut-off achievable (few hundreds of keV), using a milli-joule short-pulse laser system, such as the ELI-ALPS SEA laser[212, 202].

3.3 Summary and conclusions

In a nutshell, this experimental campaign represents a realistic case scenario, in which the theoretical background reported in chapter 1 have been investigated, using the diagnostics discussed in chapter 2.
We first described the experimental setup, including the details of the OAP alignment, the target and focus imaging systems. Then, we summarized in section 3.2.1, the experimental method used for the estimation of both the focal spot size and the laser peak intensity. Their values are respectively: focal spot size d= 5.19 μm and maximum achievable laser peak intensity I= $2.11 \cdot 10^{19}$ W/cm^2. As mentioned previously, many aspects need to be considered for laser peak intensity estimation. The analysis presented in section 3.2.1 highlighted the uncertainties related to the detection area.
It was a successful pilot experiment campaign in which optimum laser-target interaction conditions have been found, enabling the generation, detection and measurements of proton and ion spectra. The proton spectrum, reported in section 3.2.2, has an energy of the order of a few hundreds of keV. They were generated by the interaction of the SEA (multi-TW ultra-short milli joule) laser with a thin aluminum foil of a few μm. It represents a sample of the complete data analysis, that needs to be completed.
These experimental results represent the starting points in the investigation of a new concept for the design of a neutron source for a laser-based transmutator. The use of single or few-cycle laser pulses, such as the one of the SEA laser [202, 212], in combination with ultra-thin targets (CAIL Scheme[222]) can be, in the future, an alternative and valuable way to enhance the laser energy to deuterium energy conversion (interaction laser-deuterated targets). This, as consequence, can improve efficiently the generation of neutrons (few MeV) with the accelerated deuterons via Deuterium-deuterium (DD) fusion. Thus, ultra-short high repetition rate-low energy laser system can potentially allow obtaining a high yield of neutron generation [110, 222].
Furthermore, the experimental conditions (geometry, distances and details of the detection system) of section 3.2.2, are also useful for the theoretical study of the next chapter, which will take as a reference, a typical experimental setup, similar to the one presented in this chapter. The detected low energy proton range is of particular interest for a manifold of applications, including the ones in cultural heritage that will be described in chapter 6.

Chapter 4

Theoretical study of a new spectrometer design for laser driven ion acceleration

The possibility of producing beams of multi-species charged particles with energies of hundreds of MeV [90, 113] through the use of high intense (I>10^{22} W/cm^2) laser systems has made imperative to develop diagnostic systems for comprehensive characterization of plasma processes, their dynamics and evolution in this new unexplored interaction regime.
Such new regimes can pose some limitations e.g. for the Thomson parabola spectrometer (TPS)[198] as originally designed.
In the last few years, there have been numerous research groups [2] that have modified TP design, introducing variations both in the magnetic [194, 4] and electric sections[36, 81] in order to increase the achievable proton spectral information (energy range between a few keV up to 100 MeV) with respect to a conventional TPS.
In this chapter, we describe the study and the optimization of a new spectrometer design, in which we propose the replacement of the dipole with different not homogeneous magnetic profiles. The aim of this TP modification is to investigate the possibility of enlarging the energy dynamic range currently detectable (mainly for protons) and potentially the energy resolution.
We, initially, briefly summarize in section 4.1 the context of our study and main results regarding the TPS modifications, that have been designed and implemented [2, 36, 194].
We describe the numerical simulations, chosen as methodology for the spectrometer design in section 4.2.2. We verify their consistency and reliability, reproducing, comparing and using, as reference, existing diagnostics' combi-

nations, such as the one reported in [95].
In section 4.4, we present and illustrate our results, in which we analyze the effect of the replacement of the dipole with a quadrupole, that is the first considered not homogeneous magnetic field profile. We investigate the tuning of its parameters for two different proton energy range scenarios: (1) low energy range, i.e from few keV up to 100 MeV; (2) high energy protons. i.e from few tens of MeV up to hundreds of MeV.
Furthermore, we have studied our spectrometer design, including also the carbon ions contributions (see section 4.4.3). In conclusion, we summarize the advantages as well as the limitations of our approach, analyzing the replacement of a dipole with different not homogeneous magnetic profiles, including the quadrupole.

4.1 Context and state of the art

Thomson parabolas are considered suitable diagnostics for characterizing multi-species laser driven ion beams (see chapter 2). However, there are some drawbacks, that can inhibit their use for experiments.
In general, the main ones are : (1) the ion pinhole, which is usually located at the front of the TPS because it does not allow to obtain any spatial information regarding the ion beam (2) the traces of ion species that have the same Z/A can overlap on the detector screen, impeding a correct analysis and (3) the separation of the ion species that have very high energies (with different or same Z/A). Indeed, if they are not strongly dispersed by the magnetic field, they are difficult to be distinguished and properly resolved. There have been several modifications of the TPS designs [36, 81, 194, 103] in order to tackle the before mentioned issues.
The first limitation has been discussed and investigated, trying different approaches, e.g. increasing the solid angle of detection by utilizing magnetic spectrometers with large acceptance angles [97] or, in some cases, the pinhole was substituted by a horizontal slit [97, 39] or multiple pinhole arrays [196, 195].
The second problem is particularly relevant for studies in which the development of compact laser driven neutron sources [1, 101], such as the ones described in chapter 3, is involved and the discrimination between the deuterium D^+ and the potential overlapping traces of C^{6+} and O^{8+} is relevant. For this particular problem, the use of the stepped differential filtering technique has been proposed [3] and experimentally tested [100, 108].
The third issue is related to the traces of different species that can overlap or cannot be distinguished due to their high energies, although they have dif-

ferent Z/A. As it is known, the traces of two different species tend to merge together, when the width of the traces, which mainly depends on the pinhole size, becomes larger than the separation between them [2, 98] (see chapter 2).
In this case, the choices in order to increase the separation of the ion traces are three: (1) increase the electric field (2) increase the distance from the detector, placing it further away [98, 200] (3) increase the length of the electrodes or change their geometries [36, 81]. All of them have some limits. The increase of the electric field values can cause the electric breakdown/discharge. The increase of the length of the electrodes strengthens the electric field as well as the possibility that the low energy particles interact with the plate of the electrodes, impeding their detection. Therefore, a wedge configuration in which the tilt of one of the plates of the electric field [36] or the use of the trapezoidal shape for the detector [81] have been tested and considered as possible solutions.
All of these aspects do not need to be taken into account separately, thus, also combinations of multiple pinhole arrays, modification of both the magnetic and electric sections have been assembled together and experimentally proved [103, 194].
We focus our attention on the modification of the magnetic section of a TPS, as it will be described in the following sections. Up to current, for example, the substitution of a standard H design of a magnetic dipole with C shape magnetic Halbach structures [194] or the use of variable gap permanent magnets [103] have been used. Both of these changes aimed at mitigating the fringe effects and increasing the detectable energy dynamic range.

4.2 The study of a new spectrometer design with not homogeneous magnetic field

4.2.1 Methodology and content of the study

The scheme of the proposed spectrometer design is illustrated in figure 4.1. It is composed of a pinhole, a magnetic section, that is is schematized as a cylinder, an electric section and an ion detector, e.g MCP.
We aim at studying the effect of the replacement of the dipole, which is characterized by a constant field with different not homogeneous profiles, shown in figure 4.1, both in terms of minimum detectable energy on the detector (energy dynamic range) and in terms of energy resolution.
In the reference system, the z axis represents the direction of propagation of the particles, while the magnetic field acts on the transverse plane $x - y$ and

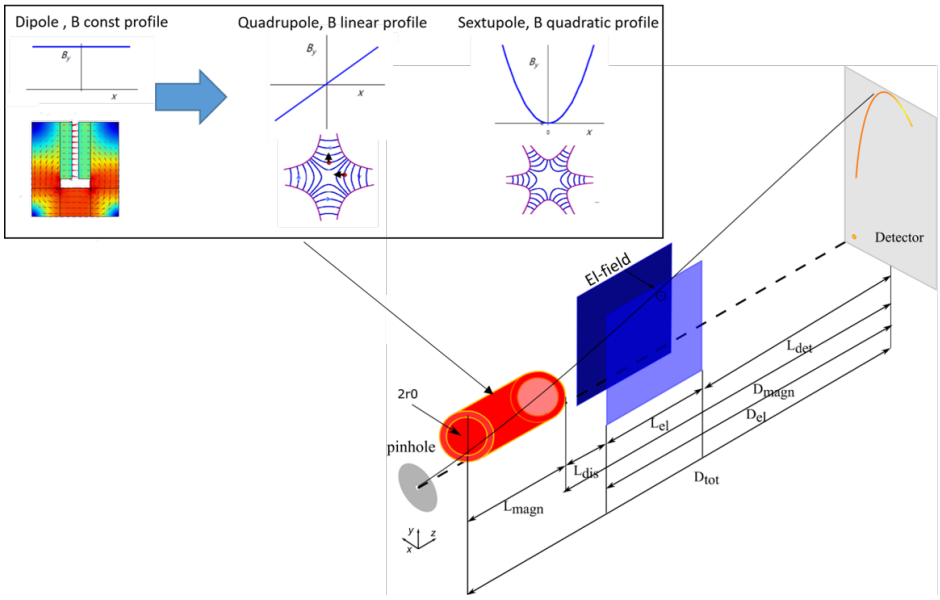

Figure 4.1: Structure of the proposed design spectrometer, that it is composed of an ion pinhole, a magnetic section, that it is depicted as a cylinder, an electric field and an ion detector (MCP). The constant dipole field is replaced by different not homogeneous magnetic field profiles.

the electric field is directed on the x axis.
We assume that the particles do not enter at the center of the magnetic element, but they are injected with a horizontal shift y=r_0 equal to the aperture of the magnetic element r_0, as is illustrated in figure 4.1. This allows to better disperse the high energy particles, that experience a stronger magnetic field.
By not homogeneous field we indicate a magnetic field, such as quadrupole or sextupoles. The magnetic profile, in these cases, scales linearly (i.e quadrupole) or quadratically (i.e sextupole) with the off-axis displacement (y/x) with respect to the direction of propagation (z) (see figure 4.1).
Thus, the magnetic field profile can be expressed with the following equations:

$$\begin{cases} B_x(y) = -Grad * y^n; \\ B_y(x) = Grad * x^n; \\ B_z = 0; \end{cases} \tag{4.1}$$

where *Grad* indicates the gradient and n is an index. The change of the gradient value allows tuning the strength of the magnetic field, whereas the change of the index n enables to distinguish the considered magnetic field

profiles. Hence, we can simulate and easily modify the magnetic sections, varying the values of $Grad$ and n.
We chose as detector a rectangular screen (e.g MCP [213]) with a maximum y dimension of 8 cm (the dispersion axis). Thus, the minimum displacement detectable on the y axis is located at 8 cm.
We can vary the distance L_{det} (see figure 4.1) between the spectrometer design and the detector screen in order to fix the maximum measurable value on the detector at a distance of 1 cm from the zero (reference point). This requirement can avoid spectral information losses. After specifying the initial assumptions and the goal of the numerical simulations, we describe in the following the model system.

4.2.2 Description of the model system

The model system, chosen as methodology, solves the Newton equation of motion of the particles (in our case protons and ions). We, first consider a Thomson Parabola spectrometer (TPS), that is a sequence of a magnetic and electric fields. [198, 166]:

$$\frac{d\vec{p}}{dt} = q(\vec{E} + \vec{v} \times \vec{B}) \tag{4.2}$$

We implement a second-order Runge-Kutta (RK) numerical method [34] as solver. The model allows us to vary the particles' features in terms of mass, charge and energy parameters (velocities) and also to choose their initial positions (coordinates).
We consider as input point sources of protons and carbon ions with low divergence. Thus, the particle-particle interactions and the space charge effects can be safely neglected.
Furthermore, the range of proton energies of our interest does not include relativistic effects (few hundreds of MeV $\ll$ 1 GeV).
We solve the particles' equation of motion and track their passage through the elements that compose the spectrometer (a TP or the spectrometer design) up to their arrival to the detector screen (see figure 4.1).
These input initial conditions permits, because of both the point particle sources and the shift y=r_0 respect to the original propagation axis (z), to select a specific portion of the magnetic field, almost constant $B_x(y)$, i.e $B_y(x)$ contribution does not affect the particles' motion.
As a consequence of these approximations, the point sources of protons/ions are deflected by the contribution of the $B_x(y)$ field. Therefore, the magnetic field and the electric field are parallel and directed on the x axis. The deflection due to the magnetic field is on the y axis, while the one due to the

electric field contribution is on the x axis (see figure 4.1).
We are aware that these initial conditions represent an ideal case scenario. However, the typical geometries of experimental setups, such as the ones described in chapter 2 and in chapter 3, can show that it can be possible to reproduce them physically by locating our system (TP or our design) sufficiently far from the particles' generation sources.
In these examples, the ion pinholes used are respectively 100 μm and 200 μm, the distance source-pinhole are respectively 20 cm and 58 cm, i.e the estimated beam divergent is less than half of a mrad and the solid angles are approximately 10^{-5} and 10^{-8} srd. This proves that the proton/ion beam had very low divergence, i. e the particle sources can assume a point source-like behaviour and our initial conditions can be close to realistic cases. However, in chapter 6, the effect of the beam divergence of a typical TNSA proton spectrum in a laser driven hybrid beamline for applications will be also discussed, considering a distance between the laser-source and entrance of the transport beamline of less than 10 cm.
As first step, we validate our model system in the following section. After that, we will present the results of the different sets of simulations.

4.3 Results

4.3.1 Validation of the model system

We have reported in chapter 2 the details of the experiment setup in which the combination of the TP spectrometer coupled with an MCP and a slotted CR39 have been studied and investigated [95].
We briefly summarize the main parameters, both in terms of the energy of the particles as well as the detection system in order to reproduce the same conditions for the numerical simulations.
The total length of the experimental setup is $\sim$ 50 cm (see figure 2.10). In this case, the Thomson parabola is composed by the sequence of a magnetic field with length $L_{magn} = 5$ cm and magnetic field strength B= 0.9 T and an electric field with length $L_{el} = 10$ cm and electric field E=22 kV/cm separated by a distance of 1.5 cm. Furthermore, the distance between the TP and the detector is $L_{det} = 18.4$ cm.
The detected proton energy [95] ranges from 2 up to 17.8 MeV, while for the carbon ions, the detected energy ranges from 5 MeV up to 58 MeV.
In detail, in figure 4.2, we compared the traces of the MCP response with our simulations' ions traces.
As it can be seen, in figure 4.2 (A), we identify the zero or reference point,

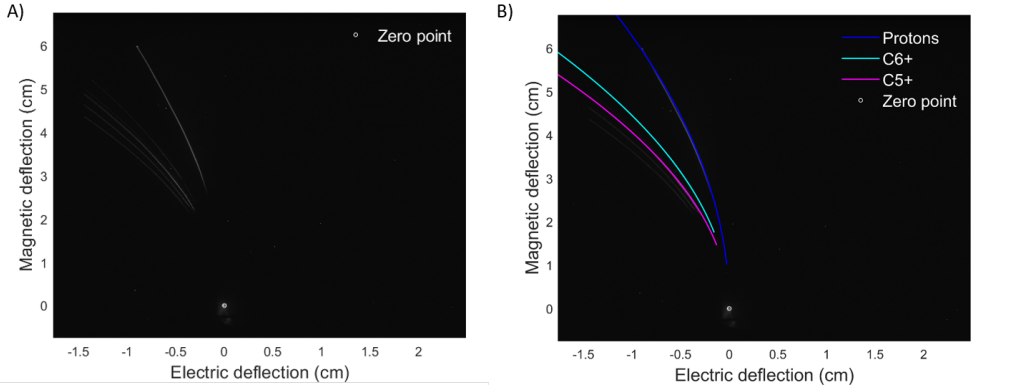

Figure 4.2: On the left hand-side, one of the experimental results of ref. [95] is reported, while on the right hand-side the comparison between the experimental results and our simulation results is shown.
For both the figures, the electric deflection is measured in cm and is on the x axis, while the magnetic deflection, also measured in cm units, is on the y axis.

while in figure 4.2 (B) we show the comparison. The theoretical results coincide well with the experimental ones. This example validates our model system and proves the good consistency with experimental results.
After the comparison, we describe the different sets of simulations, taking as a benchmark a conventional Thomson parabola design, composed of a sequence of a magnetic field of 0.9 T with a length of 10 cm and an electric field of E = 12 kV/cm with a length of 5 cm, separated by a distance of 1 cm.

4.4 Enhancing dynamic range with not linear magnetic field

4.4.1 The replacement of a dipole with a quadrupole for low protons energy range

In this section, we composed our spectrometer structure, investigating the replacement of the dipole with a quadrupole for the magnetic section.
The parameters that, in general, describe a quadrupole structure, are: (1) bore radius that, can go from few mm [174, 57] up to few cm [197] ; (2) the quadrupole gradient G (currently the maximum achievable gradient is of the order of 500 T/m [145, 125]) and (3) the length L_{quad}.

As it is known, in a quadrupole, the gradient $Grad$ can be calculated as the ratio between the magnetic field (B) and the bore radius (r_0), i.e. $Grad = B/r_0$ [214]. Therefore, considering an initial magnetic field $B = B_0$= 0.9 T (taken as reference) and a bore radius r_0 =2.2 cm, it is possible to evaluate the correspondent gradient (see equation 4.1).
We use as input a proton source with an energy range that goes from 0.5 MeV up to 100 MeV (see color bar on the right hand side of figure 4.3(A)). These energy values represent a realistic case scenario because currently the maximum achievable laser driven proton energy detected is 100 MeV [90].

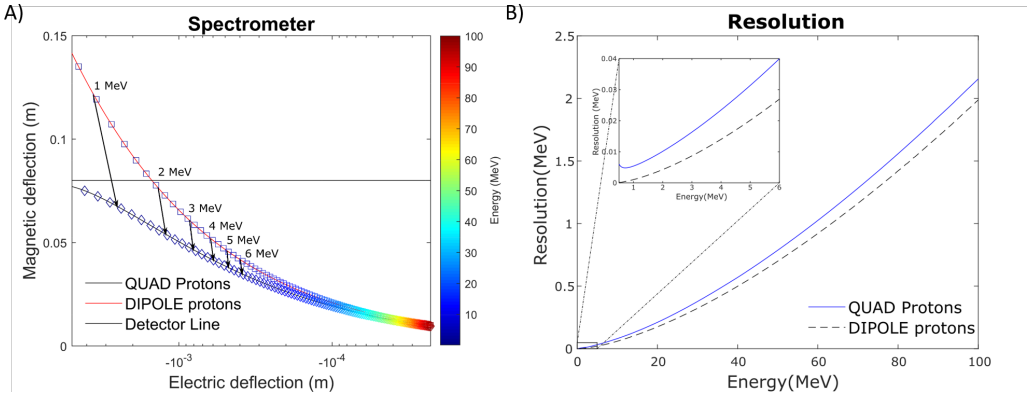

Figure 4.3: (A) The comparison between the dipole case with B_0= 0.9 T, L_{magn}= 10 cm and the quadrupole case with the same length $L_{quad} = L_{magn}$ and same initial magnetic field that corresponds to gradient G_{quad}= 45 T/m. On the x axis the electric deflection is measured in m (in logarithmic scale), while on the y axis the magnetic deflection is in m (in linear scale). The color bar on the right hand side represents the correspondent energy range (from a few keV up to 100 MeV). (B) The comparison between the two energy resolutions, calculated, according to the formula 4.3 for the dipole and the quadrupole.

We apply, for both the cases of the quadrupole and the dipole, a static and constant electric field E_0 = 12 kV/cm with a length of 5 cm. Furthermore, the magnetic and electric fields are separated by a distance (indicated as L_{dis} in figure 4.1) of 1 cm and the distance between the exit from the electric field to the detector (indicated as L_{det} in figure 4.1) is 5 cm. We consider as detector a screen of y dimension of 8 cm (see detector line in the figure 4.3(A)).
The dipole parameters are B_0= 0.9 T, L_{magn}= 10 cm. The quadrupole parameters are, for consistency, length $L_{quad} = L_{magn}$, Gradient G=45 T/m, i.e magnetic field B_0=0.9 T and bore radius r_0=2.2 cm.

In the comparison between the quadrupole and the dipole in figure 4.3 (A), it is clearly visible by the arrows, that join respectively the energies of 1, 2, 3, 4, 5, 6 MeV, that, respect to the detector limit (8 cm), the low energy range of protons are collected back on the detector screen in the case of the quadrupole, i.e there is an increase in spectral information.
Furthermore, for a more complete analysis, we estimate the energy resolution. The uncertainties of the ion position on a detector can limit the energy resolution of a conventional TPS[139]. If the projection of the ion pinhole on the detector screen has a size, that we can indicate as δR, the energy resolution is function of the displacement of the particles from the zero point (see figure 4.2).
This distance can be calculated as R= $\sqrt{x^2(E) + y^2(E)}$ for $z = z_0$ (our propagation axis), therefore the energy resolution can be retrieved, using the following formula:

$$\delta E_{res} = \frac{\delta E}{\delta R} \delta R_p \tag{4.3}$$

where δR_p depends on the size of the pinhole, that it is typically 50-100μm [95]. In our case, we use δR_p=100 μm as reference. We evaluate the resolution of both the cases and we show their comparison on the right hand side of the figure 4.3.
The overall energy resolution for the total analyzed energy range, i.e. from a few keV up to 100 MeV, slightly decreases, as it can be seen in the figure 4.3(A). In particular, we highlight in the inset of figure 4.3(B) the energy resolution in the range between 0.5 up to 6 MeV, which corresponds to the same range of energy shown by the arrows. The difference is of the orders of few tens of keV. The overall energy resolution values go from a few keV up to less than half MeV.
The results of figure 4.3 prove that it is possible to enlarge the detectable energy dynamic range at the cost of losing few tens of keV in energy resolution. In the next section, we further investigate the comparison between the dipole and the quadrupole cases in order to verify if this improvement is scalable to a high proton energy range.

4.4.2 The replacement of a dipole with a quadrupole for high protons energy range

We explore, in detail, the tuning of the quadrupole parameters, compared to the dipole with the aim of studying the effect of this replacement for a high energy range of a point source of both proton and carbon ion beams (see section 4.4.3).

We vary both the parameters of dipole and quadrupole in order to use as input a proton source with an energy range that goes from MeV up to few hundreds of MeV (see the color bar of figure 4.4 (A)).
For all the cases, we have applied the same electric field contribution $E_0 =$ 12 kV/cm with a length of 5 cm, as it was done before. For consistency, we have the same length $L_{quad} = L_{magn} = 10$ cm.
Furthermore, we have still kept fixed at 1 cm the distance from the zero (reference point) to the maximum detectable energy on the detector screen (dimension = 8 cm). The distance between the electric field and magnetic field is 1 cm for both of the cases. After introducing the initial assumptions, we run different sets of simulations in order to optimize the quadrupole parameters.

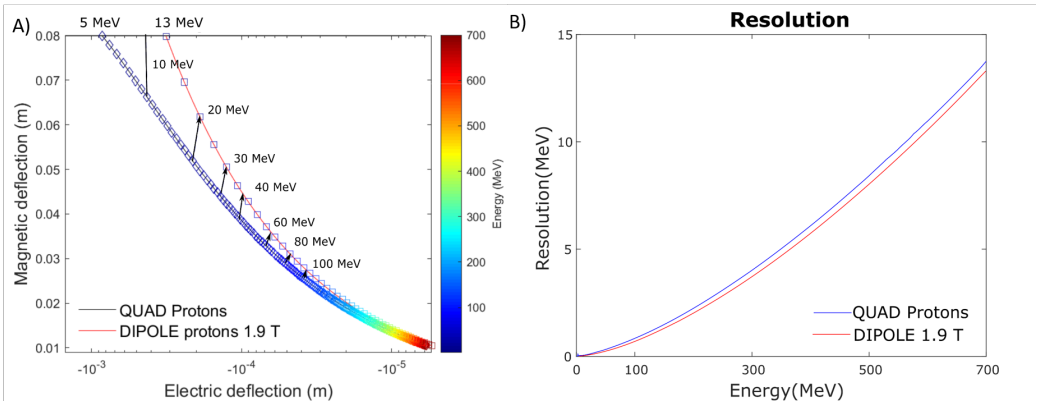

Figure 4.4: (A) The comparison between the dipole case with B_0= 1.9 T, L_{magn}= 10 cm and the quadrupole case with the same length $L_{quad} = L_{magn}$ and same initial magnetic field that corresponds to gradient G_{quad}= 100 T/m. On the x axis the electric deflection is measured in m (in logarithmic scale), while on the y axis the magnetic deflection is in m (in linear scale). The color bar on the right hand side represents the correspondent energy range (from a few keV up hundreds of MeV). (B) The comparison between the two energy resolutions, calculated, according to the formula 4.3 for the dipole and the quadrupole.

As mentioned before, while in the case of the dipole, the maximum feasible magnetic field achievable is 1.4 T, in the case of the quadrupole, the maximum achievable gradient is of the order of 500 T/m. Thus, we change the parameters in order to explore the effect of a stronger gradient demanded by the increase of the proton energy range of interest.
The optimized quadrupole parameters are gradient G= 100 T/m, bore radius=1.9 cm and magnetic field at the tips B_0 =1.9 T.

We modify, accordingly, the dipole magnetic field, that becomes $B_0 = 1.9$ T. For the first comparison, illustrated in figure 4.4(A), the drift between the detector and the spectrometer L_{det} (see figure 4.1) has the same value of 11 cm to keep at 1 cm from the zero our reference point.
The theoretical results show that the overlap between the quadrupole and the dipole with $B_0 = 1.9$ T, has the same trend observed for the low energy range (see figure 4.3 (A)).
In detail, the arrows that join, in this case, the energies 10, 20, 30, 40, 60, 80, 100 MeV show the same behaviour of figure 4.3(A). Furthermore, the comparison of the energy resolutions (calculated, using the equation 4.3) is illustrated in figure 4.4 (B). This difference is very small and of the order of a few keV. Hence, it is possible, to increase the energy dynamic range of the detected protons, substituting the dipole with a quadrupole.
However, we are aware that a dipole design with such an high magnetic field is challenging. We, therefore, further add in figure 4.5 (A) the comparison between the quadrupole case with a more realistic case scenario, represented by a dipole with B_0= 0.9 T.

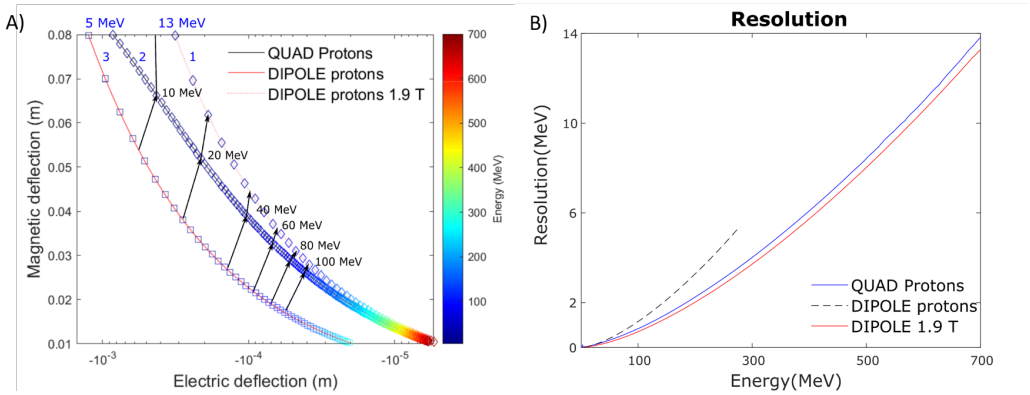

Figure 4.5: (A) Comparisons between the dipole cases with $B_0 = 0.9$T, L_{magn} = 10 cm (line 3), the quadrupole case ($L_{quad} = L_{magn}$), Gradient G_{quad}= 100 T/m (line 2) and the dipole case with $B_0 = 1.9$ T, $L_{magn} = 10$ cm (line 1). On the x axis we plot the electric deflection in m (in logarithmic scale), while on the y axis we plot the magnetic deflection in m (in linear scale). The color bar on the right hand side represents the correspondent energy range (from a few keV up to maximum 700 MeV); (B) The comparison between the energy resolution (y axis) calculated (see equation 4.3) in MeV versus proton energy range (x axis in MeV), for both the homogeneous cases of the dipoles and the case of the quadrupole (high energy range).

The three cases in figure 4.5 are labeled with three different numbers. For this

particular set of simulations, we decided to locate the minimum detectable value on the detector screen to a value of 5 MeV (5 MeV - indicated in blue in figure 4.5). This led to the possibility to explore a high range of proton energy, as well as to study the feasibility of our detection system. The cases of the dipoles (lines 3 and 1) are simply shifted, due to the change of the dipole magnetic field, while the comparison between lines 1 and 2 is the same as that illustrated in figure 4.4 (A).
Hence, the comparison that brings us new information is the one between lines 2 and 3. The quadrupole parameters did not change, while for the case of the dipole with $B_0 = 0.9$ T, we obviously have to change the drift between the spectrometer and the detector to a value of $L_{det} = 16.5$ cm in order to respect our reference condition (5 MeV minimum detectable energy).
In detail, in figure 4.5 (A) it can be observed that in the case of the dipole with B_0=0.9 T, the detectable proton energy range goes from 5 MeV (our lower limit) up to 250 MeV, while in the case of the quadrupole we can extend it up to 700 MeV.
The arrows of the figure 4.5 (A) join the energy positions of 10, 20, 40, 60, 80 and 100 MeV, and they allow also to visualize the increase in energy resolution (the protons are better dispersed in the case of the quadrupole), as represented in figure 4.5 (B).
For completeness, we have also studied the same three cases described before, fixing this time, as reference, the maximum energy observed on the detector screen (700 MeV- indicated in red in figure 4.6 (A)). As it has been already done in refs [194, 200], it is possible to tune the drift between the electric field to the detector L_{det} in order to modify the detectable energy spectra.
In our case, we want to obtain maximum detectable energy of 700 MeV for all the three cases. The lines 1 and 2 remain the same as the figure 4.5 (A) because they have already 700 MeV as maximum detectable energy, while we change the drift L_{det} =30 cm for line 3.
As it can be seen in figure 4.6, with these modifications, it is possible to observe a bigger energy dynamic range in the case of the quadrupole with respect to the dipole cases. The energy resolutions are very close to each other and the difference between the three cases is of the order of a few keV, as shown in figure 4.6 (B).
In summary, the theoretical results have verified that it is possible to tune the parameters of the quadrupole in order to scale and increase the detectable proton energy dynamic range. Despite the slight loss in term of energy resolution and even considering a big drift (L_{det} =30 cm) for the dipole case (see figure 4.6), the quadrupole is still the best choice for enlarging the proton energy dynamic range by keeping, at the same time, a compact structure.
In the following section, we investigate the two proton energy case scenarios,

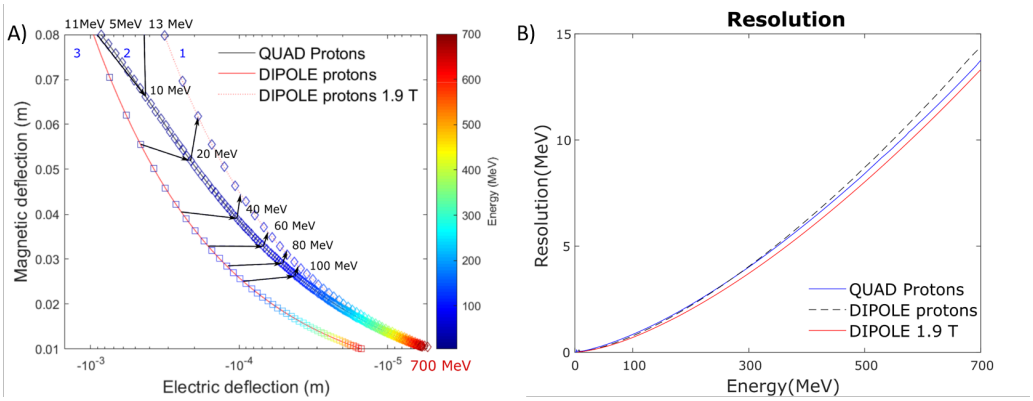

Figure 4.6: (A) Comparisons between the dipole case with $B_0 = 0.9$T, L_{magn} = 10 cm, L_{det} =30 cm (line 3), the quadrupole case ($L_{quad} = L_{magn}$), Gradient G_{quad}= 100 T/m (line 2) and the dipole case with $B_0 = 1.9$T, L_{magn} = 10 cm (line 1). The distance L_{det} to the detector is kept 11 cm both for the quadrupole and the dipole with $B_0 = 1.9$T. On the x axis we plot the electric deflection in m (in logarithmic scale), while on the y axis we plot the magnetic deflection in m (in linear scale). The color bar on the right hand side represents the correspondent energy range (from a few keV up to maximum 700 MeV); (B) The comparison between the energy resolutions (y axis) calculated as reported above (see equations 4.3) in MeV versus proton energy range(x axis in MeV), for both the homogeneous case of the dipoles and the case of the magnetic field profile of the quadrupole (high energy range).

including the carbon ions contribution.

4.4.3 Carbon ions

In this section, we considered the same designs and same magnetic field profiles, using as sources protons and carbon C^{5+},C^{6+}.
We decided to add only these two carbon ions species, because they are produced in huge quantity compared to the other respective species C^{4+},C^{3+} [95] and because they are also characterized by a value of q/m much more close to the behaviour of the protons.
We have implemented a first set of simulations, using the quadrupole parameters of section 4.4.1: Grad: 45 T/m, bore radius: 2.2 cm, L_{quad}=10 cm. The simulated carbon ion beams have the same energy interval of the protons from a few keV up to 100 MeV. We use the same distance between the magnetic and electric field (L_{dis} =1 cm) and the same distance from the

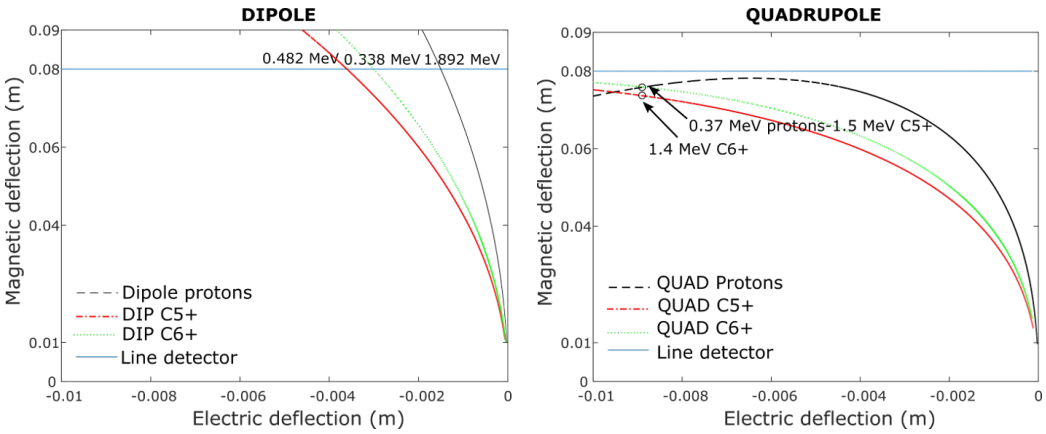

Figure 4.7: Ion traces observable on the detector. Our point sources include proton, C^{5+} and C^{6+}. On the right hand side, we show the quadrupole case (B_0 =0.9 T, r_0 = 2.2 cm, Grad= 45 T/m, L_{quad}= 10 cm) and a constant electric field of 12 kV/cm, while on the left hand side the same ion traces are shown, considering a constant magnetic field of B_0= 0.9 T, L_{magn}= 10 cm, keeping the same parameters for the electric field. The drift L_{det} is 5 cm for both of the cases.

detector L_{det} = 5 cm. The detector screen has y dimension of 8 cm.
The comparison between the ion traces on the detector is shown in figure 4.7. For the quadrupole case, the carbon ions have the same type of displacement observed in the proton case (see figure 4.3).
However, the carbon ions' traces passing through the quadrupole can create an overlap with the proton trajectories (see right hand side of figure 4.7).
Therefore, the dipole represents the best choice, as can be seen from the energy values indicated in figure 4.7. The quadrupole minimum detectable energy for the carbon 5+ and carbon 6+ is respectively 1.5 MeV and 1.4 MeV, while for the dipole, it is respectively 0.482 MeV and 0.338 MeV. For the protons, instead, the minimum detectable energy is the same and this confirms our previous theoretical results (see section 4.4.1).
We run a second set of ion traces simulations, applying a magnetic field of the dipole B_0 =1.9 T and the same quadrupole parameters of section 4.4.2 in order to investigate the overlap of the ion traces for high energy range particle sources.
The second set of quadrupole parameters (see section 4.4.2) are the following: G=100 T/m, bore radius:1.9 cm, L_{quad}=L_{magn}=10 cm.
In this case, the energy for the protons goes from a few tens of MeV up to few hundreds of MeV (250 MeV), as shown in figure 4.5, while for the carbon ions we can enlarge it to hundreds of MeV. The distance between magnetic and

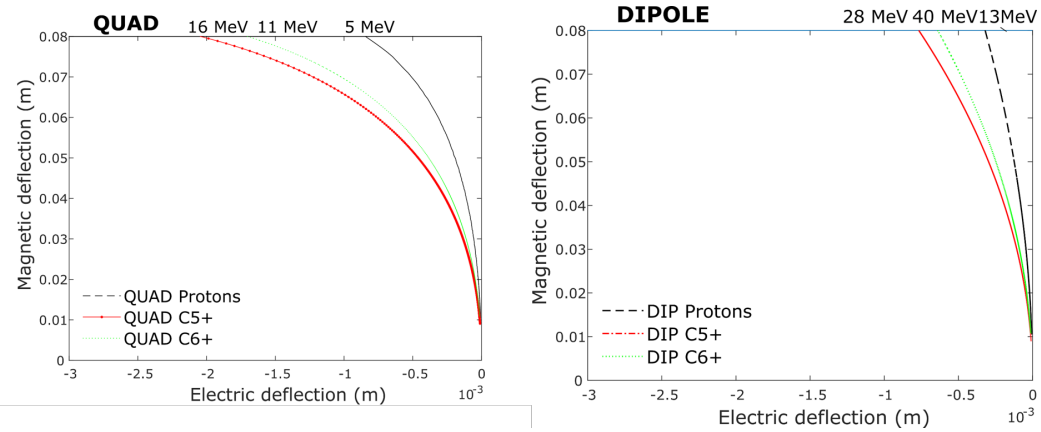

Figure 4.8: Ion traces observable on the detector. Our point sources include proton, C^{5+} and C^{6+}. On the right hand side we show the quadrupole case (B_0 =1.9 T, L_{quad}=L_{magn}=10 cm.) and a constant electric field of 12 kV/cm, while on the left hand side the same ion traces are shown, considering a constant magnetic field of B_0= 1.9 T, keeping the same parameters for the electric field. The drift L_{det} is 10 cm for both of the cases.

electric fields is 1 cm and the minimum detected energy is at 8 cm (detector screen).
We report in figure 4.8 the same comparison of figure 4.7 for the new set of quadrupole parameters. The overlap of the previous case is not present on the detector screen. Thus, the simulations evidence that a stronger quadrupole gradient is needed for improving the detection of both proton and carbon ions together. The results prove that there is a considerable improvement in terms of the low energy dynamic range. The quadrupole minimum detectable energy for the carbon 5+ and carbon 6+ is respectively 16 MeV and 11 MeV, while for the dipole case, it is respectively 28 MeV and 40 MeV. The increase in the capture of the low energy particles is of the order of few tens of MeV, as it is visualized by the energies indicated in figure 4.8. The carbon traces on the detector screen are also better separated.
The same improvement trend is observed in terms of energy resolution with respect to the dipole case and it is reported in figure 4.9.
We calculate the resolutions of the dipole and quadrupole for the carbon ions cases, using the equation 4.3. The resolutions are shown in figure 4.9, separately for carbon 5+ and carbon 6+.
For the carbon ion cases, these comparisons prove that the difference between the quadrupole and the dipole case is of the order of a few keV. Thus, the second set of quadrupole magnetic profiles represents the best choice, both in

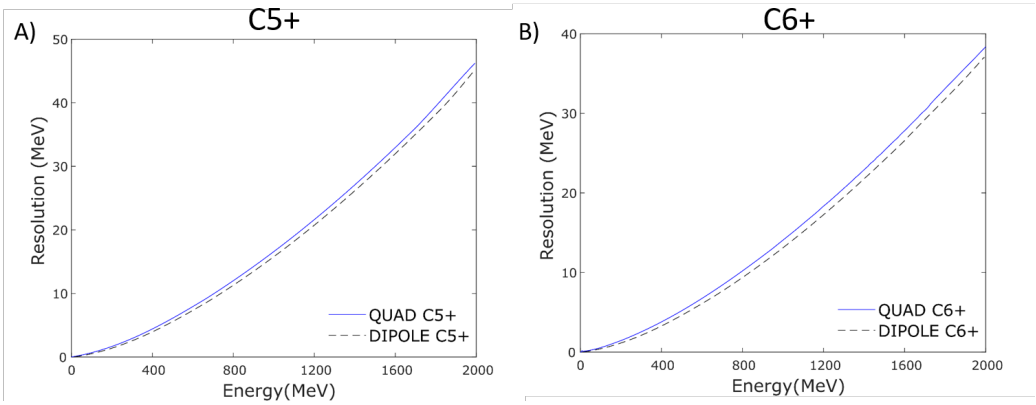

Figure 4.9: The comparison between the energy resolution (y axis), calculated using the equation 4.3, is illustrated for both carbon 5+ and carbon 6+ in MeV versus carbon energy range (x axis in MeV), for both the homogeneous case of the dipoles and the case of the quadrupole (high energy range).

terms of energy dynamic range and energy resolution for carbon ions beams. The results presented for the carbon ions are consistent with the ones presented for the protons and confirm the advantage of the use of the quadrupole compared to the dipole. However, they highlight that, if we are interested in the detection of protons/carbon ions in the low energy range, a stronger quadrupole gradient is needed in order to avoid the overlap of the traces, preserve the achieved gain in spectral (energy) information and for obtaining an overall improvement in the ion species detection (trace separation).

4.4.4 Scaling law for different not homogeneous magnetic field profile

The encouraging results that have been obtained in the previous sections lead us to further study the effect of the replacement of a homogeneous magnetic field with different magnetic field profiles, such as decapole and octupole.
Thus, a set of simulations have been implemented in order to investigate the minimum achievable detectable energy achievable with these modifications. We decide to use as input a point source of protons that goes from a few keV up to 100 MeV.
The quadrupole parameters are length L_{quad}, magnetic field B_0, r_0=2.2 cm, gradient $Grad$= 45 T/m, as described in section 4.4.1, because they are suitable for the current proton energy achievable experimentally in terms of laser driven proton acceleration (proton energy range between few keV up to 100 MeV [90]).

For consistency, the same distance between the spectrometer and the detector L_{det} =5 cm and the same distance between the electric and magnetic field L_{dis}= 1 cm have been used for all the cases. We fixed L_{det} =5 cm in order to keep a 1 cm distance from the zero on the detector (our initial condition). Furthermore, our detector has a dimension of y=8 cm, as illustrated by the black detector line in figure 4.10.

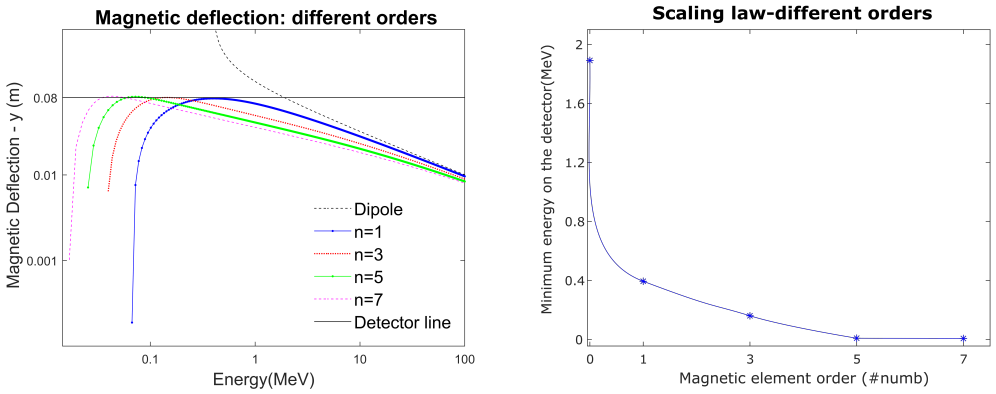

Figure 4.10: On the left hand side, the overlap of the different magnetic profiles compared to the case of the dipole (homogeneous field) is shown. The continuous black line represents the detector line (in our case, it is fixed at 8 cm). The dashed black line represents the magnetic deflection of the reference case of the dipole, while the blue, red, green and magenta lines represent the cases of the not linear magnetic profiles. Both the x axis and the y axis are in logarithmic scale. On the x axis the proton energy range is in MeV, while on the y axis, the magnetic deflection is in m units.
On the right hand side, the scaling law is shown. We illustrate the different orders (n) of the magnetic profiles vs the minimum energy that can be measured in MeV on the detector.

Starting from the equations 4.1, we considered different index n values and gradients. We exclude the even n values because the magnetic field profiles affect the low energy proton trajectories (our proton range of interest), turning them back and impeding their arrival on the detector. Hence, we analyze the odd cases of n = 1, 3, 5, 7 (see figure 4.10).
We can respectively obtain magnetic field profiles of a quadrupole, an octupole, a decapole and a multipole element (order 7). The gradients are indicated with G_q, G_{oct},G_{dec} and G_{mult} . They are calculated using equations 4.1 and have the following values: G_q= 45 T/m, G_{oct} =1859 T/m^3, G_{dec}=1.7$\cdot 10^8$ T/m^5 and G_{mult}= 3.6 $\cdot$ 10^{11} T/m^7.
In the case of the spectrometer composed by a dipole, the energy spectral in-

formation achievable and observable on the detector screen, goes from 1.891 ($\sim$ 2 MeV) up to 100 MeV, while for the not homogeneous magnetic profiles, the achievable spectral information increases from 1.891- 100 MeV to 0.392-100 MeV (case n=1), 0.15 - 100 MeV (case n=3), 0.008-100 MeV (case n= 5) and 0.0061-100 MeV (case n= 7) (see figure 4.10).
This comparison is also visualized on the plot of the scaling law on the right hand side of figure 4.10, in which the magnetic element order versus the minimum detection energy on the detector is shown.
The results, illustrated in figure 4.10, evidence that the replacement of a homogeneous magnetic field with the different not homogeneous fields can effectively increase the achievable energy dynamic range in the low proton energy range, without introducing losses for high energy. The reduction of the magnetic field of the dipole is obviously possible, but it is unavoidable to lose in high energy particle dispersion. Furthermore, as expected, there is a proportionality between the increase in the order of the elements and the respective increase in detectable information (minimum energy observable on the detector screen).
However, after the third-order (decapole) it was observed that there is not a significant improvement in terms of capture of the low energy particle compared to the previous orders, as can be seen in figure 4.10.

4.5 Discussions and conclusions

In this chapter, we present the theoretical study of a novel type of spectrometer with the aim of investigating the enhancement of detectable energy dynamic range, compared to existing spectrometer combinations.
We have implemented different sets of simulations, studying the replacement of different not homogeneous field profiles instead of a constant dipole field in a TP design, for two proton energy range scenarios. Our results provide useful guidelines regarding the advantages and the limitations of our proposed designs.
In section 4.4.1, for a proton energy range between a few keV up to 100 MeV [90], the theoretical simulations proved that it is possible, using the quadrupole case, to increase the detectable energy dynamic range in the low energy range, without significant losses in terms of energy resolution. This "new" detectable proton energy range is particularly relevant for applications, such as the ones in cultural heritage, that will be described in chapter 6. However, laser sources that include carbon ions, are limited by the potential overlap of the ion traces, as reported in section 4.4.3. The minimum detectable proton energy value, in this case, becomes 0.38 MeV.

For proton energy range that goes from a few keV up to hundreds of MeV, such as the ones obtained with conventional acceleration [60], we observed in section 4.4.2 that the change of the quadrupole parameters led also to an improvement in terms of detectable proton energy dynamic range. This detectable proton energy enhancement is easily scalable, starting from the case of the low proton energy range scenario and we obtained also similar energy resolutions. The observed energy resolution differences are always of the order of a few keV. In figure 4.5, we showed that the quadrupole allows to almost duplicate the detectable proton energy range with respect to the dipole and the energy resolution can be increased of few tens of keV.
Furthermore, the addition of the contribution of the carbon ions 5+ and 6+ does not perturb these improvements. The results of the carbon ions evidence that a strong quadrupole gradient is both a suitable choice and is required in order to obtain an overall improvement in terms of energy resolution, separation of the traces, compactness and detectable energy dynamic range.
We also deduced that these advantages can be further extended by manufacturing very sophisticated magnetic devices, with strong gradients. However, this improvement saturates after the third order magnetic field profile that corresponds to a decapole element.
In conclusion, the quadrupole magnetic profile represents the most reliable, suitable and feasible (easy to manufacture and assemble) case, among the analyzed ones. The versatility and the tunability of the replacement of the quadrupoles in our spectrometer designs, compared to the existing combinations, e.g. the tuning of the length of the drift [201, 103] in combination with a TPS, allows constantly to enlarge the detectable energy information achievable, without losing in energy resolution and gaining compactness of the total spectrometer structure. Therefore, according to the constraints of the different experimental setup and the proton energy information needed to be detected for specific applications, the proposed spectrometer design can represent an alternative and versatile laser driven proton diagnostic.
In laser driven proton acceleration, the use of quadrupole (e.g doublet or triplet) is not new because they have been implemented, as reported in refs [197, 174, 147], downstream laser-plasma interaction point for manipulating and adapting laser proton sources for applications, as it will be discussed in chapter 5. Similar sets of quadrupole parameters will be used for the detailed numerical study of a laser driven proton hybrid beamline for applications, subject of chapter 6.

Chapter 5

Introduction of laser driven proton hybrid beamlines and post acceleration schemes

Laser driven proton beams have been used as sources for a wide range of applications, ranging from medical application (PET or cancer treatment)[30, 120], warm dense matter [156, 28], inertial fusion [172], material science[56, 13, 12, 15] up to cultural heritage[17, 16].
Currently, the high beam divergence (few tens of degrees at the source) and the wide energy spread (up to 100%) of laser generated ions limit their efficiency and their use for applications.
To overcome these issues, there have been different proposals for manipulating the laser-generated proton beams downstream the laser-plasma interaction point using conventional accelerator devices, implementing so-called hybrid beamlines or post acceleration schemes.
This chapter aims at providing an overview of the different transport elements, such as RF cavities, dipoles, quadrupoles, etc that have been coupled with laser driven proton sources for adapting and customize them to a specific application.
We report the results of the first examples of laser driven proton hybrid and post acceleration beamlines in section 5.1.
We mainly focus our attention on the PQMs pairs hybrid schemes [197, 174, 147] and the use of passive magnetic chicanes[41, 181, 179] as energy selectors (ES), because these studies are important references for design and the optimization of our laser driven proton hybrid beamline, which will be discussed in chapter 6.

5.1 Laser driven proton hybrid beamlines

5.1.1 History and state of the art

In general, the main requirements for most of the LDIA applications [176, 75] are:

- Reach a lower energy spread around a central energy, therefore, reduce the initial typical energy spread of the beams ($\sim 100\%$)
- Obtain stable and controlled (collimation, capture and transport) beams
- Tunability in energy and final transverse focus spot sizes (focusing, shaping and energy selection)
- Suitability for high repetition rate TW (even PW) laser systems

In the last few years, novel alternative acceleration regimes [113, 184] (see chapter 1) and the use of sophisticated targets [183, 124] have been studied theoretically and experimentally [104, 138] with the aim of better controlling the acceleration mechanism and improving the proton beam yield.
In 2006, the use of ultra fast triggered micro lens have been proposed by Toncian et. al. [199] for focus, collimate and select a part of laser generated proton spectra with a small energy spread.
This scheme [199] requires two laser pulses: one, for the proton sources (Chirped Pulse Amplification (CPA)1 in figure 5.1 (A)), while the second one (CPA2 in figure 5.1 (A)) irradiates the micro-lens, that is the hollow cylinder of $\sim$ 1 mm diameter and few mm length
The irradiation of the laser CPA2 starts to accelerate and inject the hot electrons through the cylinder's wall. They are, then, spread inside and evenly onto the cylinder (Debye shield of hot electrons). A space field is temporally created (arrows) 5.1 (B) and starts the plasma expansion towards the vacuum and sustains the radial electric field 5.1 (C) that focus, collect and select the laser protons passing inside the cylinder.
Although this double-pulse scheme has shown good results in terms of feasibility and energy tunability (the delay between the two pulses can be controlled with picosecond precision and can be tuned for choosing the required proton energy range selection), it is not considered preferable compared to other approaches. The complex geometry of two laser beams that need to be synchronized or delayed with respect to the main pulse, as well as the deterioration of the hollow cylinder (it needs to be changed after every shot) does not make it easy implementable and suitable for increasing repetition rate of high power laser systems. To avoid the double pulse scheme, an alternative

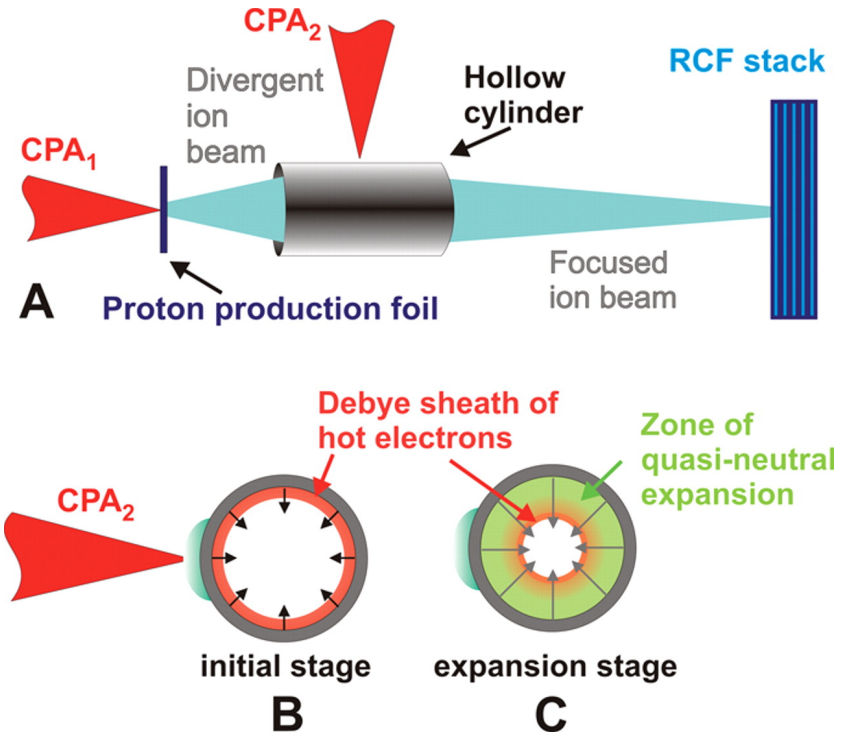

Figure 5.1: Ultrafast laser driven microlens: (A) Double pulses scheme and (B-C) radial electric field creation inside the hollow cylinder. Figure extracted from [199].

option with one side closed cylinder irradiated only by the main laser pulse was also investigated, but in this case, the energy tunability is lost due to the absence of the second laser pulse and problems of fast realignment, synchronization, and decrease of proton efficiency have been observed[199, 218]. Hence, several research groups have designed different laser driven proton hybrid beamline and/or post acceleration schemes, using accelerator devices such a RF cavity [142] (see 5.2), a compact travelling wave accelerator [102], pulse powered solenoids [31, 32], permanent quadrupoles magnets(PQM) [174, 197, 147] (see 5.3), magnetic passive chicanes that act as energy selectors (ES) [181, 179, 169] (see 5.4). Some of these hybrid beamline and post acceleration schemes will be described in detail in the following sections, emphasizing, for each of them, the advantages and disadvantages.

5.2 Coupling with RF cavity

The first experimental evidence of a post-acceleration scheme for laser generated ion beams has been provided by Nakamura[142].
Nakamura [142] et al, proposed to post accelerate laser generated ion beams, using the principle of longitudinal phase space rotation (see fig 5.2). They applied a RF electric field that has a maximum electric field amplitude of ± 40 kV/20 mm, synchronized with the pulsed laser[142].
The utilized laser plasma protons sources, were driven by a TW Ti: Sa laser system (pulse duration ∼ 210 fs, energy 350mJ, 1 Hz) focused on a rolled tape target of thin Ti foil (thickness of both 3 and 5 μm) [142].

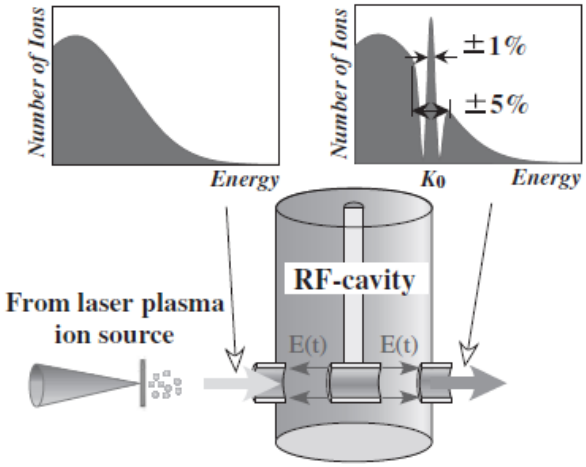

Figure 5.2: The principle of "phase rotation" applied to laser generated proton sources leads to the creation of peaks in energy distribution. Figure reported from [142].

The RF cavity resonator had two accelerating gaps of the same size (20 mm) and the distance between them was 100 mm. The RF cavity was located at distance ∼ 1.080 m from the source and its mode of operation was π (the polarity of the electric field between the two gaps is opposite). The laser source at 80.7 MHz was used as a trigger for the RF electric field in order to guarantee the same phase relation between the RF electric field itself and the pulsed laser.
In the fig 5.2, the principle of "phase rotation" applied to a laser source is illustrated. The laser generated ion beams are accelerated within a short time (less than 1 ps), relatively small compared to the period of the RF electric field (period = 12.39 ns), used for the phase-space rotation. The ions with

different energies and different velocities arrive, after travelling the appropriate distance of around 1 m (this distance is suitable in order the ions pass during the half period of the RF frequency) at the accelerating gaps of the RF cavity at different times. The difference in time of arrival is translated in acceleration for lower energy particles that arrive later and deceleration for the fastest ones that arrive earlier. This allows the creation of local energy peaks in energy distribution (see figure 5.2) [142].
The reported results (see figure 5.3), clearly show the effect of the coupling with a RF cavity resonator and the formation of the local energy peaks (with phase rotation), compared to the laser driven proton spectra without phase space rotation (maximum proton energy observed was around 800 KeV).

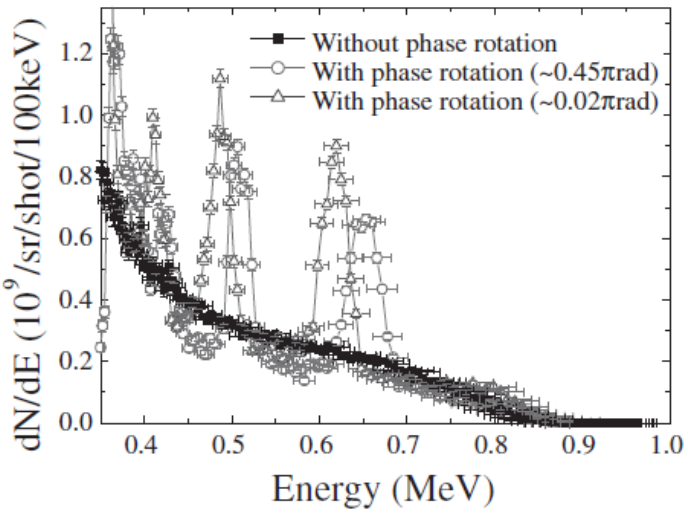

Figure 5.3: Laser generated proton energy spectrum with and without the "phase space". Figure extracted from [142].

Ions (especially protons) with certain incident energies, that travel a certain distance and arrive to the accelerating gaps, experience the phase rotation given by the RF electric field and create the local few hundreds of keV energy peaks. The final energy spread observed with respect to the central energy of these peaks at full width half maximum (FWHM) is around $\sim 7\%$. Furthermore, these energy peaks can be also slightly shifted in position by the difference in phase between the RF cavity electric field and the pulsed laser (see figure 5.3).
This post acceleration scheme has good reproducibility and compactness for laser drive proton sources at 1 Hz. Therefore, it can be also suitable for an

additional increase in the repetition rate of the laser ($\sim$ 10 Hz). Furthermore, the change in the relative phase between the RF electric field and the pulsed laser can give energy tunability with a relatively small final energy spread. However, the laser driven proton beam energy is very low (few hundreds of keV) and this represents a strong limit for their use, as well as the dependence from the incident energy of the protons.

5.3 Coupling laser proton sources with PQMs

Between 2008 and 2009, sets of permanent quadrupoles magnets (PQMs) ([197, 147, 174] have been employed to shape, collimate (transport and capture) and focus laser driven ion beams.
The magnetic field B of a quadrupole is usually zero at the center, and its intensity increases linearly with off-axis displacement. Therefore, a quadrupole, in a transverse plane (coordinate system x-y), can contemporary focus/defocus a particle beam that passes through it in one plane and defocus/focus in the other plane, according to the orientation of its poles. Its main parameters are the bore radius (r_0), the length (l) and the gradient ($G = B/r_0$), as it was discussed in chapter 4.
In this section, we summarize and compare the results of the three pioneer works that involve laser driven proton hybrid beamline schemes with PQMs pairs, emphasizing differences and similarities. [197, 147, 174].
The research group of Sargis Ter-Avetisyan [197], was among the firsts, in using PQMs pairs for laser driven proton beams manipulation (focusing, collimation and shaping).
In ref. [197], the laser generated proton sources were obtained by the interaction of TW Ti:Sa laser system (pulse duration: 40 fs) focus on a 5 μ m Ti target with an intensity of $I \sim 10^{19} W/cm^2$.
It was initially tested the focusing behaviour of a single quadrupole with the following features: length: 5 cm, bore radius: 2 cm, gradient of $\sim$ 65 T/m, therefore $B_0 \sim 1.318$ T), locating it 15 cm, downstream a laser generated proton source (see figure 5.4) (A). These choices have been considered suitable for selecting a laser proton beam in the range between 3-4 MeV. Taking into account that protons at different energies are focused at different positions (chromatic effect), they located an Al filter of 70 μm to block protons with energies below 2.8 MeV, in order to have a clear detection (MCP).
The figure 5.4 (B) shows the effect of a quadrupole on the laser proton bunch that focuses it in one plane (vertical) and defocuses (horizontal) it in the other one.
After detecting and optimizing the focal distance for one quadrupole at a

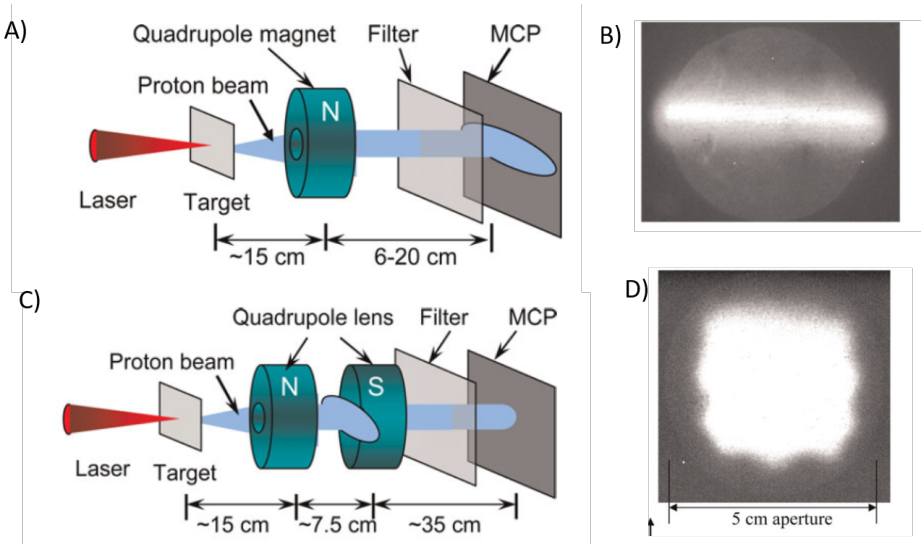

Figure 5.4: (A) Experimental setup with a single quadrupole; (B) Focus measurement with experimental setup with one single quadrupole; (C) Experimental setup with quadrupole pairs; (D) Focus measurement with experimental setup with quadrupole pairs. Figure adapted from [197].

certain energy, a magnetic quadrupole lens system (PQM) system was built. They used a second identical quadrupole (rotated of 90° respect to the first one to invert the poles) in order to collimate the beam (5.4 (C)). A final beam density profile with a rectangular shape of 4 mm × 4 mm has been observed (see figure 5.4 (D)), locating the detector at a distance of 35 cm from the last quadrupole.
In figure 5.5, the measurements of the proton energy spectrum of the initial not collimated beam (black line) are compared with the final one (in red), after the PQMs pair scheme. They observed a final selected proton bunch with more than $\sim 10^8$ protons with an energy of (3.7 ± 0.3) MeV. The width of the peak observed, as reported in [197], depends from the resolution of the implemented measuring system.
Furthermore, the proton density of the final "quasi" mono-energetic beam ((3.7 ± 0.3) MeV) reached, is increased up to a factor ~ 30, compared to the possible 40 achievable (if all the initial not collimated protons with this energy would be collimated). These results [197] demonstrate that magnetic quadrupoles allow to focus, collect and collimate laser driven proton beams. Both Schollmeier et. al [174] and Nishiushi et al. [147] have implemented as well magnetic quadrupole lens systems.
Schollmeier et al. have measured laser driven proton beams of maximum

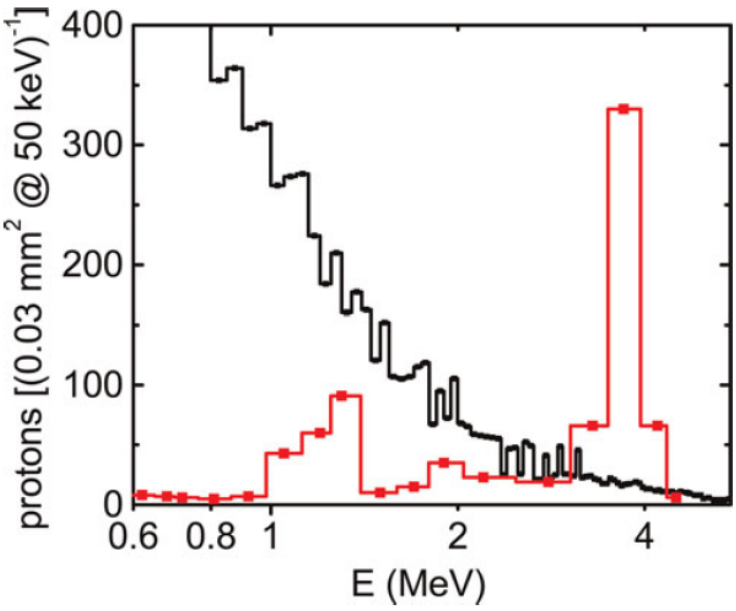

Figure 5.5: The proton energy spectrum of the initial not collimated beam (black line) compared with the final one (in red), after the PQMs pair scheme. Figure reported from [197].

energy of 22 MeV that comes from the interaction of a PW (λ= 1053 nm) laser system with 40 J energy, pulse duration less than 1 ps, focused on a 5μm Cu foil [174]. The PQMs used are miniature devices with a strong high field gradient up to 500 T/M with a bore radius around 1 mm, a length of less than 2 cm. The structure is, therefore, very compact (total length: 50 cm after the source) and allowed to focus 14 ± 1 MeV with 10^6 particles (final FWHM spot size of 286 μm $\times$173 μm) [174].
Nishiushi et al. [147], instead, were the first that used as input laser driven proton sources with 1 Hz repetition rate. The laser parameters were energy 0.7 J, pulse duration 30 fs focused on a sophisticated polyimide tape target of 12.5 μm. (I $\sim 10^{20}$ W/cm^2). The maximum observed proton energy was around $\sim$ 3 MeV at 1 Hz repetition rate.
In this case, the two PQMs had different magnetic field strength (55T/m and 60 T/m), different lengths (5 cm and 2 cm) and bore radius (3.5 cm and 2.3 cm). The total length of the hybrid beamline is 65 cm after the source. These differences aim at increasing the capture and the collection of the beams. They managed to focus (2.4 ± 0.1) MeV with $\sim 10^6$ particles (final FWHM spot size of 3 $\times$8 mm^2).

The details presented and reported show that by changing the quadrupoles' features, the hybrid beamline scheme can be easily adapted to different types of laser driven proton sources [197, 174, 147]. The use of PQMs system pairs represents a valuable option and can be optimized separately, independently by the used laser proton sources.
Using a longer quadrupole and a stronger gradient allows to improve the compactness of the hybrid beamline scheme and shorten the focal distances [174]. These schemes can be also suitable for high repetition high intense laser system [147]. Furthermore, when it is possible to reach such a small focus spot size with a high number of particles, the space charge effect due to the Coulomb repulsion among the particles maybe need to be taken into account. As it is known, the laminar parameter allows estimating if the beam is space charge dominated or emittance pressure dominated [165, 91, 75]. When its values are greater than 1, the space charge effects cannot be ignored (see chapter 6).
In ref. [197], the final beam spot size is big and it is of the order of $\sim$ 4 mm $\times$ 4 mm, as well as the entrance radius, therefore the space charge effect is negligible, while in reference [147, 174], although the final spot sizes are smaller and final selected energies are different, the final number of particles (low current) achieved makes still this contribution unimportant.
The hybrid beamlines proposed in [197, 147, 174]) allow to collect, collimate (reducing the initial proton divergence) and monochromize laser driven proton beams, in a reproducible way, providing good improvement of the obtainable final proton beams features.
Among the disadvantages, there is the fact that the magnetic field of a quadrupole impedes the optimal collimation condition of the beams, which are "quasi" parallel and "quasi" mono-energetic [197]. Furthermore, the sizes and the magnetic shielding of the quadrupoles represent constraints for the vicinity of the two quadrupoles or the vicinity of the first quadrupole to the source [197, 174], while the apertures (bore radius) can bring to some losses and limit the acceptance of the beams, especially passing from one quadrupole to the other one [174, 147].
The chromatic effects of the quadrupoles (protons with different energies are focused in different locations) bring an energy-spot size dependence that makes important their position. However, at the same time, this aspect can be also useful for applications in which a transverse focusing spot size tunability is needed (see chapter 6).

5.4 Coupling with passive magnetic chicanes of dipoles

Passive magnetic chicanes of dipoles, that account for the energy selection of laser driven proton beams have been also used [41, 181, 179].
One of the first prototypes and experiments with this hybrid beamline scheme has been provided by Chen et al.[41].An energy selector (ES) is generally composed of a sequence of four identical magnetic dipoles, that are disposed symmetrically with respect to the central selecting slit and are preceded by an initial collimating slit, as it is shown in figure 5.6.
The multi-MeV laser driven proton beam is collimated by the first slit and then dispersed by the Lorentz force from the first dipole (outward magnetic field) and guided to the central selecting slit by the second one (inward magnetic field), while the last two dipoles (respectively, inward and outward magnetic fields) realign the selected proton beam in its original propagation direction (see figure 5.6).

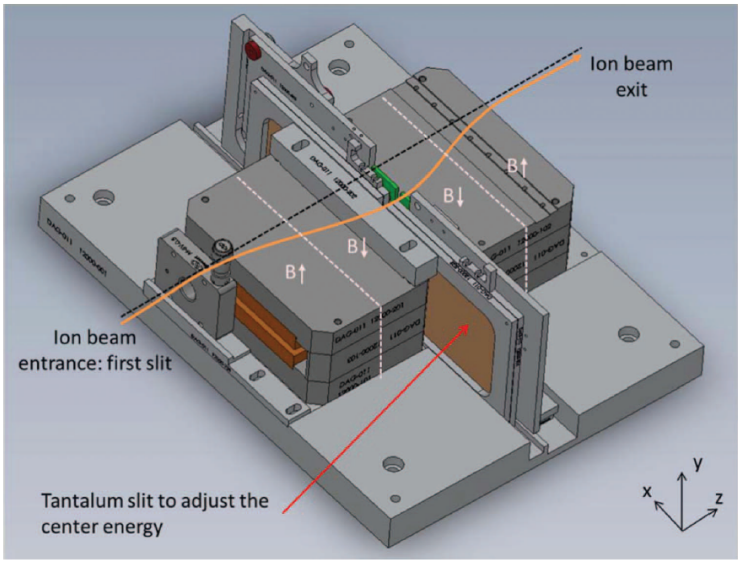

Figure 5.6: Drawing of energy selector (ES) structure. Figure extracted from [41].

The scheme used by Chen et al [41] is very compact, has a total length of $\sim$ 20 cm and a width of 10 cm with the magnetic field of B=1 T. This ES structure has been designed for the selection of a proton energy range between multi-hundreds keV up to 1 MeV with a final energy spread of $\sim$ 5%.

It was tested with the ELFIE laser system at the Laboratoire pour l'Utilisation des Lasers Intenses (LULI). The laser driven proton source was generated by the irradiation of a 25 μm gold foil with 10J, 350 fs pulse duration ($\lambda \sim 1057$ μm) laser system [41].
The ES was located 22 cm from the source. The distance between the ES and the source and the choice of the aperture of the initial collimating slit to a value of 200 μm allowed to decrease the initial divergence of the proton beam to 1 mrad. The first collimating slit was made of stainless steel, while the central selecting one was made of tantalum. Furthermore, the aperture of the central slit was fixed to a value of 500 μm. This choice was considered as the best compromise for reaching the final energy spread requirements while avoiding drastically reducing the number of particles of the selected beam.

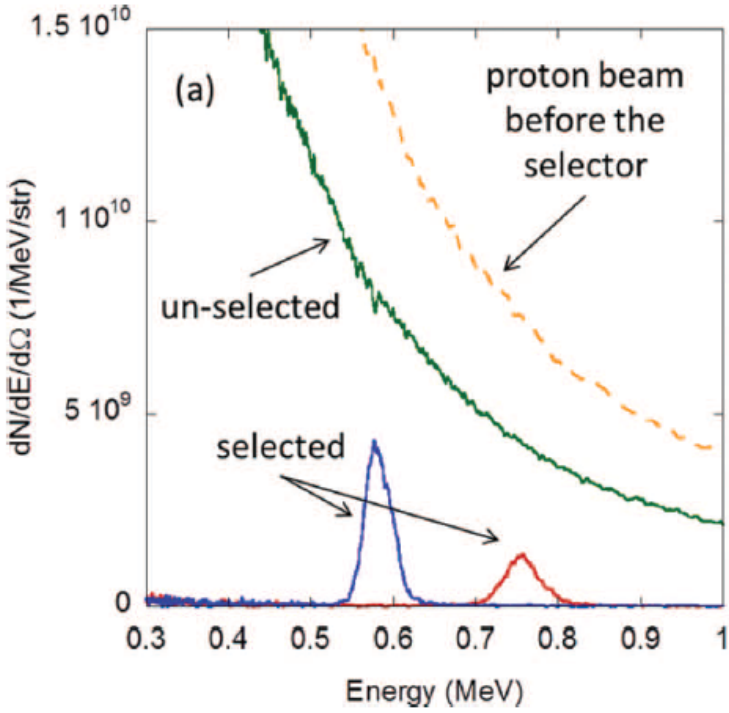

Figure 5.7: Proton energy spectra measurements performed in four different conditions and for four independent shots. Figure reported from [41].

The results, reported from [41] in figure 5.7, show the proton spectra measurements that have been performed for four independent shots in four different conditions, The orange line refers to the case in which the ES was not implemented, while the black line (indicated as unselected) refers to a

measurement that has been performed, locating the ES after the source with the central selecting slit completely open, in order to observe only the effects on the final proton beams parameters from the first initial collimating slit.
The two selected peaks, instead, correspond respectively to an energy of 755 keV with an energy bandwidth of 50 keV (blue line) and an energy of 580 keV with an energy bandwidth of 30 keV (blue line). For obtaining two different selected energies, the central selecting slit of the ES (kept with the same aperture of 500 μm) was moved in two different locations.
This passive magnetic device can provide the energy tunability for laser driven proton sources through the movable adjustable slits in an easy and fast way (see figure 5.7). Furthermore, the scheme is compact (easy to allocate inside the vacuum chamber, that it is typically 1-2 m diameter in LDIA experiment) and can allow the realignment of the exit selected beam in a stable way.
However, there are two main limitations in terms of the final number of particles obtainable and final energy spread. These two aspects are related to both the choice of the aperture of the central movable slit and the features of the source beam [41]. Decreasing the value of the aperture of the central selecting slit can decrease the final obtainable energy spread, but also inevitably reduce the final number of particles. Therefore, its choice should be a right compromise between a reasonable final number of particles and the final application requirements in terms of energy spread. The final energy spread of the particles is also influenced by the natural intrinsic divergence of the laser proton beams. They have an initial transverse momentum that affects their normal transverse displacement across the dipoles [41]. Furthermore, in ref. [41] extra spatial dispersive effects on final proton beam features have been observed and were attributed to the asymmetry and imperfections of the setting of the scheme.
The same hybrid beamline scheme proposed by Chen et al [41], was further studied and investigated by other research groups [181, 169, 179]. The features of dipoles and the slits (apertures and materials) have been changed according to the different final application requirements.
In particular, in ref. [181, 169], the ES dimensions are bigger than the other two cases [179, 41], because the energy range of laser driven proton beams that need to be selected arrive to an upper limit of 60-70 MeV. The total length of the ES reached $\sim$ 3.5 m, the magnetic fields of the dipole varied between B=0.085-1.4 T (maximum limit achievable), each dipole length is of the order of 40 cm and the dipole's gaps are 6 cm. These choices have been made because the ES structure has become a section of the external ELIMED (the Czech pillar of the international ELI project) transport beam for laser driven ion beams for medical applications.

The parameters of the ES structure that have been studied by Sciscio' et al. [179] are intermediate between the two cases presented above[41, 181, 169]. They are [179] suitable for selecting a proton beam with an energy range between 2-20 MeV and allow to reach a final energy spread of $\sim$ 20 %.
In the design of laser-PIXE hybrid beamline for material science applications discussed in chapter 6, an energy selector (ES) section is considered. The features of our ES structure are closer to the ones of Sciscio' et al because the final proton beam requirements are similar to the ones of our application. Additional details regarding our ES components (dipoles' features, distance between the laser-proton source and the ES and slits apertures) and the final proton beams requirements will be described in detail in chapter 6.

5.5 Summary and conclusions

In this chapter, we have summarized the details of the first hybrid beamline and post acceleration schemes, that have been proposed for manipulating and transport laser driven proton beams.
Nowadays, the initial choice of using a single type of transport structure (conventional accelerator devices) [142, 197, 174, 142] coupled with laser proton sources has been gradually replaced by the use of combinations and/or sequences of different elements, as it was introduced in chapter 3.
For example, the post acceleration scheme with RF cavities of Nakamura et al [142], have been further investigated by Nishiuchi et al [148], who proposed a complete laser proton driven beamline scheme including both permanent quadrupoles triplets and RF cavities for focusing and selected a final proton energy beam of 1.9 MeV with a final energy spread of 5%.
There have been also numerical studies regarding the possibility to post accelerated laser driven proton beams using accelerating structure, such as Drift Tube Linac (DTL) cells [7, 8]. In detail, the numerical simulations reported in ref. [6] prove that a potential acceleration of an initial 7 MeV laser proton beam up to $\sim$ 15 MeV, within a total distance of 8 m, can be achieved using 48 DTL cells.
Moreover, high powered solenoids have been introduced by Burris et Mog [31] and have been used also by Busold et al. [32]. Combinations of a RF cavity and high powered solenoids [33] have been implemented to deliver proton energies bunches of around 9.6 MeV with more than 10^9 particles and a final energy spread down to $\sim$ 3 %.
Sophisticated pulse powered magnets (both quadrupoles and dipoles) and solenoids [126] have been also designed especially for medical field applications.

Furthermore, there have been complete laser driven proton beamlines that include sequences of permanent quadrupoles magnets[169, 132] (the initial collimating and collecting stage) followed by an ES structure (energy tunability and selection). These combinations [169, 132] can provide energy tunability also in the energy range of 60-70 MeV with a very small final energy spread and increase the overall transmission efficiency of the transport line, decreasing the particle losses.
Therefore, numerous and various hybrid beamlines[197, 132] or post acceleration schemes[142, 148] have been studied and have been used.
Although each scheme presents some advantages and disadvantages, the coupling of laser driven proton sources with conventional accelerator devices is currently considered a valuable option for tailoring (shaping, transporting, selection, focusing) the laser driven proton beams. These schemes can efficiently improve the proton quality and yield and make them implementable for a great variety of applications.
In particular, we use as a reference for the choice of the transport systems that compose our compact laser-PIXE hybrid beamline for material science applications, the experimental results and the studies regarding the ES structure and the PQMs pair schemes. Further details regarding our hybrid beamline scheme are described in chapter 6.

Chapter 6

Laser driven proton beams for applications in the domain of cultural heritage

This chapter deals with the detailed numerical study of the design of a compact laser driven proton hybrid beam, mainly dedicated to cultural heritage (CH) application, but also implementable for other types of applications in material science (semiconductors doping, etc..).
We initially give, in section 6.1, a brief introduction of the context and the state of the art of a particular sophisticated nuclear technique named Particle induced X-ray emission (PIXE) [152], used in the field of cultural heritage with conventional electrostatic accelerators [122].
We focus our attention on the PIXE technique with proton as sources. We describe the potential advantages given by the use of laser driven proton beams as alternative sources in CH and we report the first experimental results [16] that open up the feasibility of this new application, named "Laser-driven PIXE".
In this chapter, we will provide indications for optimizing the elements of a compact proton beamline, first reproducing typical proton beam parameters as obtained on classical PIXE with conventional electrostatic accelerators [152] and then potentially improving the technique.
In section 6.2.1, we report the methodology for testing, designing and optimizing our proposed hybrid line schemes. Coupling laser-generated proton sources to conventional beam steering devices successfully enhance the capture and transport of the laser-accelerated proton beams. This leads to a reduction of the high divergence and broad energy spread of the source.
The design of our hybrid beamline is composed of an energy selector (ES), followed by permanent quadrupole magnets (PQMs) aiming for better control

and manipulation of the final proton beam parameters. This allows tailoring both, mean proton energy and spot sizes, yet keeping the system compact. We analyze at the beginning only the ES performance. Then, we present the study of the entire hybrid line including the focusing elements (i.e. the ES followed by one or two PQMs). Finally, we present and illustrate the results and the conclusions are drawn.

6.1 Particle Inducted X-ray emission (PIXE): context and state of the art

In the last decades, there was a lot of effort from many research groups worldwide[16, 76, 224], in order to find innovative techniques, both in the field of physics and chemistry, for diagnostics and conservation in the domain of the cultural heritage.

Figure 6.1: Cultural heritage artworks: 1) Painting : Madonna dei fusi - Leonardo Da Vinci; 2) Renaissance Venetian Glass Collection; 3) Bronze sculpture - Statuette du trésor des bronzes de Bavay.

The main challenge in the CH world is to collect as much information as possible regarding the chemical [20, 173] and morphological [178] state of the surface and the bulk of the samples (paintings, bronze, pigments, ceramics, etc.) while preventing any possible damage [35, 112] as well as find the best way for their conservation and restoration without any aesthetic aspect modification.
Surface spectroscopies, such as Photoluminescence, Raman, X-ray photoelectron spectroscopy (XPS), X-ray fluorescence (XRF), Energy dispersive X-ray

Fluorescence (EDX)[224] in Scanning Electron Microscope (SEM) are techniques used to retrieve chemical information on the artworks (see figure 6.1). Morphological information [178] can, instead, be obtained with SEM.
Chemical elements present on the surface and in the bulk can be detected using also sophisticated techniques of nuclear physics, such as Particle Induced X-ray and Gamma Emission (PIXE and PIGE), as shown in figure 6.2. PIXE and PIGE measurements, conventionally, are performed using, as sources, charged particles (i.e. protons, alpha particles and sometimes heavy ions) [152].

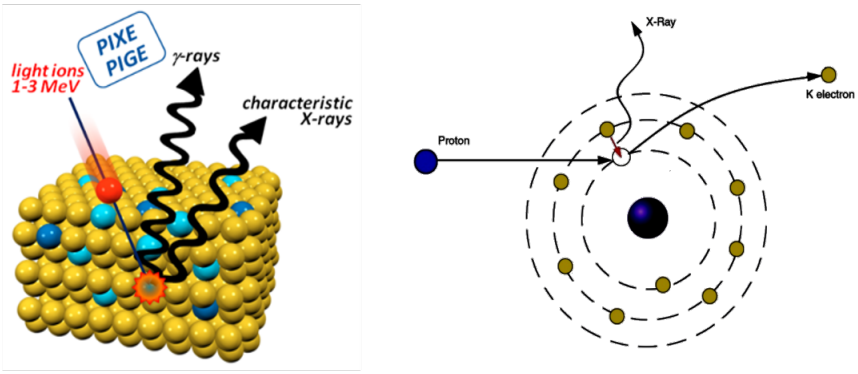

Figure 6.2: Sketch of PIXE and PIGE spectroscopies. When a light ions (protons) beam interacts with a sample, induces characteristic gamma rays (PIGE) and characteristics X-rays (PIXE) emissions. On the left side, it is illustrated this interaction, while, on the right, it is shown that, upon the interaction of a proton with an atom, a core electronic excitation takes place and a characteristic X-ray photon (PIXE) is produced by the electron-hole or vacancy rearrangement (L to K shell in this case).

In detail, when proton beams (light ions) with energies between 1 to 3 MeV irradiate the material samples (ceramics, bronze, pigments, etc.) a core electronic excitation takes place. Then, the subsequence electron-hole or vacancy rearrangement causes the production of the characteristic X-rays (PIXE) (see figure 6.2). The produced X-ray radiation can be measured by energy-dispersive detection systems[20] and provides the characteristic fingerprint of the chemical elements and their respective quantities present in the sample [224].
In PIGE spectroscopy [52], the incident proton beams (1-3 MeV) can reach the target nuclei (weaker Coulomb repulsion) of the sample and the short range nuclear interaction comes into play. The target nucleus can be excited and when the de-excitation of the nucleus occurs, the characteristic gamma

ray is emitted. Nuclear energy levels are specific for each element, hence, from the gamma ray energies, the chemical elements and their respective quantities [42] can be retrieved, as well as it is done for PIXE spectroscopy. Sometimes, during a CH analysis, the presence of patina, varnish or crust on the samples [42] can inhibit the X-rays detection because the X-rays produced, especially from very low Z material elements, can be re-absorbed by the material itself and/or can be lost during the path between the sample to the detector [207]. Therefore, usually, the PIGE spectroscopy [52] that is, instead, very sensitive for light elements' detection, is used as a complementary technique in order to compensate the missed information or gain additional ones [42].
In ref. [46], for example, the two techniques PIXE and PIGE are implemented together for a glass sample analysis. In this case, the comparison between the energy spectra both from the characteristic X-ray and the characteristic gamma ray of very low Z elements is important for the following reasons.
It can validate the presence of the same chemical element, such as Sodium, using simultaneously two different techniques and it can also provide the difference between their respective quantities, both in the bulk (PIGE) and the surface (PIXE) of the sample [27, 42, 152]. This is very useful for understanding the state of deterioration of the artworks and gives an advantageous hint for the appropriate restoration process [152, 42].
For our study, we focus our attention on proton beams used as probes for PIXE spectroscopy. Proton sources are usually preferable compared to X-rays or electrons, for several reasons:

- It is possible to gain information on low Z material, such as Calcium or Sodium [27], that are relevant for the restoration processes of the artworks (i.e. glass samples- Renaissance Venetian Collection-Louvre figure 6.1);
- The detection limit [35] achievable is two orders of magnitude (up to 20 ppm) better than X-ray;
- The easy transport and manipulation of proton beams by electric and/or magnetic transport devices over large distances without significant losses;
- Variable spatial resolution is obtainable because proton beams can be focused down to the micrometer range and we can achieve a more precise analysis [35];
- The possibility to have "differential PIXE" (protons with different energies arrive at different penetration depths due to their Bragg peaks).

This allows retrieving additional information regarding the manufacturing, construction or painting techniques.

The PIXE spectroscopy, using protons as source, is performed in facilities such as the Accélérateur Grand Louvre d'analyse élémentaire (AGLAE) [130, 163], shown in figure 6.3, located at the French Louvre laboratory - (C2RMF) [225] in Paris (France), the AIFIRA facility at Centre d'Etudes Nucléaires Bordeaux-Gradignan (CENBG) [10, 189] in Bordeaux-Gradignan (France) and Instituto Nazionale di Fisica Nucleare- LAboratorio di tecniche nucleari per i BEni Culturali (INFN- LABEC) laboratory in Florence (Italy) [61, 74, 164].

Figure 6.3: Accélérateur Grand Louvre d'analyse élémentaire (AGLAE), Paris, France. Figure reported from [152].

In these laboratories, electrostatic accelerators (such as Van der Graff tandems or Pellatron types [122]) generate proton bunches with energies that go from 1 to 5 MeV, a beam current from few pA to nA [43], a beam charge of the order of nC [158].
The final proton parameters, obtainable from the external beamline of AGLAE [152, 158], are summarized in table 6.1.
In the following section, we report the first results that drive the possibility to use laser generated proton sources as an alternative for PIXE spectroscopy and we describe the potential advantages of these sources compared to the

conventional ones for this particular application.

Case (protons)	AGLAE external beamline
Mean Energy	1- 5 MeV $\sim$ 2.5 MeV
Energy spread	$\leq$ 10 %
Focus spot	10 μm up to 500 μm
Beam current	10- 150 nA
Beam charge per shot	1.8 n C per shot

Table 6.1: Conventional PIXE final proton parameters

6.1.1 Laser driven proton beams as alternative sources for Cultural Heritage applications

Recently, the use of laser accelerated proton beams as diagnostic for chemical analysis of CH artifacts has been investigated [16, 11, 133, 154].
Barberio et al. irradiated an ancient ceramic sample (an amphora from AD 1650) with a laser proton beam driven by the Jupiter laser, Livermore (CA), that has intensity $\sim 10^{20}$ W/cm^2, laser energy up to 220 J, focal spot diameter (FWHM) $\sim$ 9 μm, Pulse duration $\tau \sim$ 700 fs, central wavelength $\lambda \sim$ 1.056 μm and repetition rate $\ll$ 1 Hz.
In the figure 6.4, it is clearly visible that the ceramic artifact (in CH, ceramic samples are considered as the most fragile type of artwork) does not show any aesthetic damage, there are no signs of fractures or cracks after the irradiation [208]. Furthermore, in the XRF performed analysis (right side of figure 6.4), it is shown that there are no significant chemical composition changes before and after the irradiation.
Therefore, they were able to demonstrate that the damage induced by the laser accelerated protons was the same (if not lower) than that induced by using conventional PIXE. However, the possibility that the short, but intense proton beam achievable using laser-driven PIXE could potentially have a positive impact on the damage induced on the artifact during the time of analysis is still under investigation.
In ref [16] it is also shown that it is possible to retrieve the chemical composition of the target with a single shot ("laser-driven PIXE") through the irradiation of a known material (e.g. silver sample) with laser generated proton beams.
We report the results of ref. [16]. The sketch of the experimental setup, the diagnostics (RCF of type HS and X-ray spectrometer and IP) and the X-ray

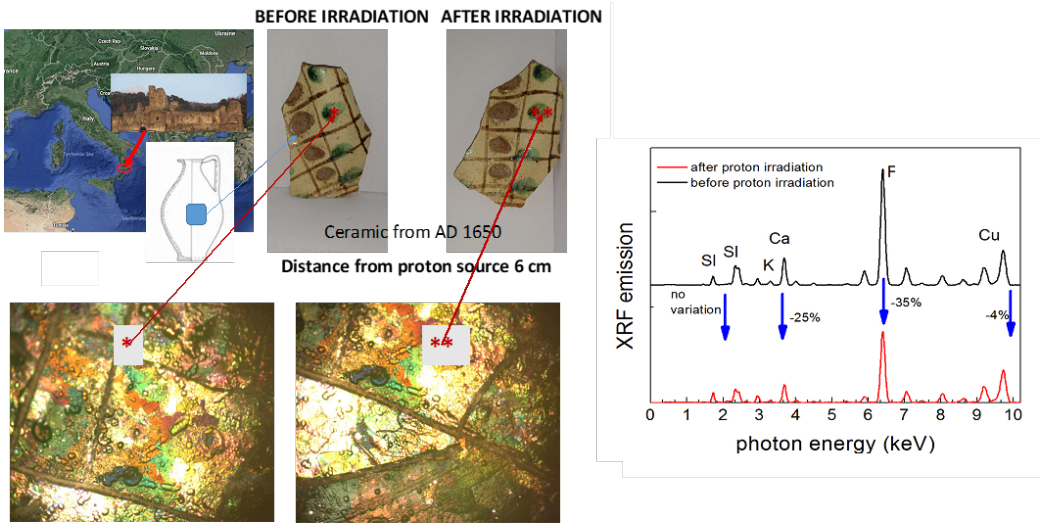

Figure 6.4: Ceramic sample and XRF analysis performed on the ceramic sample, figures extracted from [16].

spectra measurements are shown in figure 6.5.
In 6.5 (A), it is visible that the angle of incidence and emission is 10 deg (space constraints) and that the safety distance source-sample is 6 cm. This length was estimated, according to the thermodynamics simulations reported in [16], to guarantee that the temperature of the sample irradiated by the proton beam stays safe below the melting point. The X-ray spectrometer range is 20-100 keV, hence, it is able to detect the silver lines. The laser-driven PIXE results are collected, through the Bragg laws, from the scanning of the IP reported in figure 6.5 (B).
The conventional PIXE and "laser-PIXE " results are in perfect agreement and allow to identify the chemical components of the silver sample (known material) and its impurities of titanium and cobalt, as it is shown in figure 6.5 (D).
These results catalyze the possibility of using a laser driven proton source for PIXE spectroscopy as an alternative to conventional machines, implementing a technique named "laser-driven PIXE".
It is possible, by means of the laser-driven PIXE, to scan larger volumes of the artworks with a single shot covering surfaces up to cm^2, as it can be seen from the detail of RCF scan in figure 6.5) (C), whereas the final spot sizes that are typical of conventional accelerators go from a few μm (1-2 μm) up to 500 μm (see table 6.1).
Laser-generated proton sources have also the advantage of an improved com-

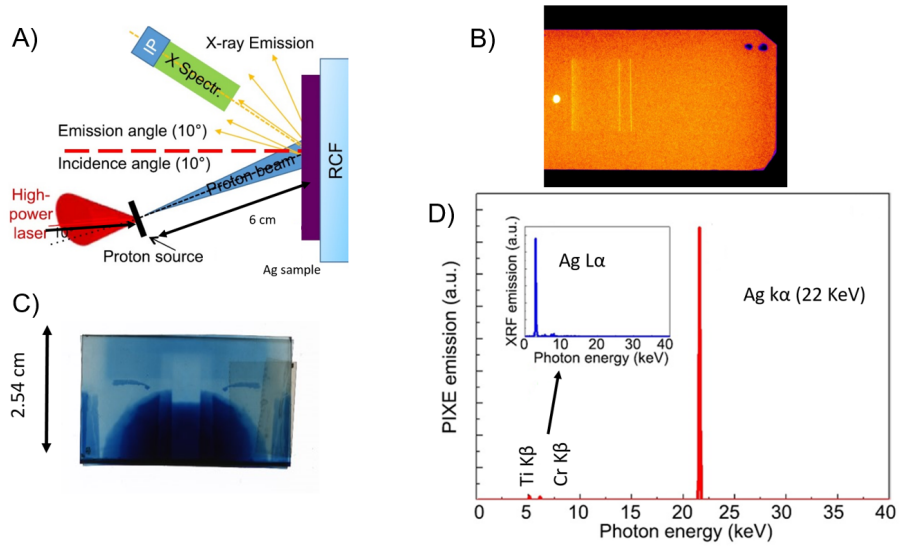

Figure 6.5: Laser-driven PIXE experimental setup (a); scan of the RCF (b), IP scan (c), X-ray spectra (d), figures adapted from [16].

pactness of the acceleration section, compared to large conventional facilities such as NEW AGLAE ($2 \times 30\ m^2$) in Paris [152] and INFN-LABEC ($40 \times 15\ m^2$) in Florence [76].
The broad energy range of laser-accelerated proton sources permits the "tuning" of the beam energy in a broad range from a few keV to tens of MeV, potentially allowing a "layer by layer" analysis of the irradiated bulk material [133].
The total time for performing a full PIXE analysis depends on the allowable current on the sample and the required photons for having a reliable signal-to-noise ratio on the X-ray detector. Compared to conventional accelerators, the technique of laser-driven PIXE" is able to scan a larger surface and – depending on the energy spread – to perform volumetric analysis. In applications where this is useful, this technique can be quicker than conventional accelerators. However, when the usable current is limited, the energy spread needs to remain small and the spot size is the same, the analysis time remains the same since this depends on the global flux.
In summary, the use of laser driven proton beams can potentially bring advantages in terms of compactness, versatility, efficiency and tunability compared to traditional types of sources.

6.2 Design and optimization of a dedicated laser driven hybrid beamline for CH applications

6.2.1 Methodology and content of the study

Laser accelerated proton beams have features that make them desirable candidates for laser-driven PIXE, as discussed in the previous section.
However, their high beam divergence (few tens of degrees at the source) and their high energy spread (up to 100%) can limit the efficiency of energy-selected beams for applications.
To tackle these problems, there have been several proposals and experiments for transporting, capturing and manipulating the laser-generated proton beams downstream the laser-plasma interaction point using conventional accelerator devices, implementing the so-called hybrid beamlines [197, 147, 41, 179] or post acceleration schemes [6, 102, 142], as it was described in chapter 5).
In this section, we study, design and optimize a dedicated transport line for applications, including the laser-driven PIXE.
We aim at comparing − in terms of proton beam features − the performance of a laser-driven hybrid beam line with the typical parameters of conventional facilities for PIXE spectroscopy[152], reported in table 6.1.
The proposed beamline design includes an ES, with similar features as reported in Scisciò et al. [179], followed by magnetic focusing devices, i.e. Permanent Magnet Quadrupoles (PQM), in order to vary the final transverse dimensions of the energy-selected beam on the CH sample.
The used ES provides the possibility of tuning the beam energy in the range that is typical for the PIXE analysis, i.e. 1–5 MeV, reducing the initial energy spread to a final value of $\leq 10\%$. The ability to select different energies in a short time allows the possibility of performing a "layer by layer" analysis of the artifact [11, 133, 154].
The reduced energy spread also allows coupling the beam exiting the ES with focusing PQMs in order to modify the analyzed surface on the CH sample, taking into account that the broad energy spread of an unselected beam would lead to unsustainable chromatic effects in the focusing section.
The variation of the PQM's position between the ES and the sample allows tuning the final transverse beam spot size from a fraction of mm^2 up to 1–2 cm^2. This potentially permits scanning a cm^2 area with a few laser shots.
We also estimate the final charge of the proton bunch, which needs to be high enough to be comparable to what is obtained on conventional facilities

(in the order of nC/shot or a fraction of nC/shot if using a higher-repetition rate laser) [158].
We first illustrate the proposed hybrid beamline scheme and we describe the methodology for designing and optimizing it. In section 6.2.2, we analyze only the ES performance and select the best features in terms of energy tunability and energy range. In section 6.2.3, we present the study of the entire hybrid beamline including the focusing elements (i.e. the ES followed by one or two PQMs).
We investigate three total length scenarios for our hybrid beamlines because they should fit in a medium/big size vacuum chamber. In laser driven proton acceleration (LDPA), the vacuum chambers have a typical diameter of around 1 m for TW laser systems [68] or, in PW facilities, can reach a diameter of 2 m [16]. Our three scenarios are:

1. the ES coupled to one quadrupole aiming at a total length of 80 cm;
2. the ES coupled to one quadrupole aiming at a compact design of 50 cm total length;
3. the ES coupled to two PQMs in a FODO configuration.

6.2.2 Hybrid beamline scheme: Analysis of the energy selector

The hybrid beamline scheme is qualitatively represented in figure 6.6 and has been studied using the beam optics code TRACE3D [111] and the particle-tracking code TSTEP [48]. These two codes are commonly used in the conventional accelerator community and allow monitoring the transport of an accelerated beam through the elements of a beamline.
The ES contribution, which accounts for reducing the energy spread of the proton bunch, is optimized, using TSTEP simulations.
Commonly, an ES [41, 181, 179] is implemented as follows: a magnetic dipole chicane with one entrance slit (a_1) and one selecting slit (a_2), as it can be seen in figure 6.6.
The entrance slit (a_1) reduces the initial divergence of the beam that enters the dipoles. The particles (accelerated along z) are then dispersed transversely along x by a distance that depends on their velocity. The aperture of the second slit (a_2), which is movable on the dispersion plane along the x-axis, accounts for the energy selection of the protons.
After the central selecting slit (a_2) – see figure 6.6 – two additional dipoles realign the selected beam along the initial propagation axis, as it was explained in chapter 5.

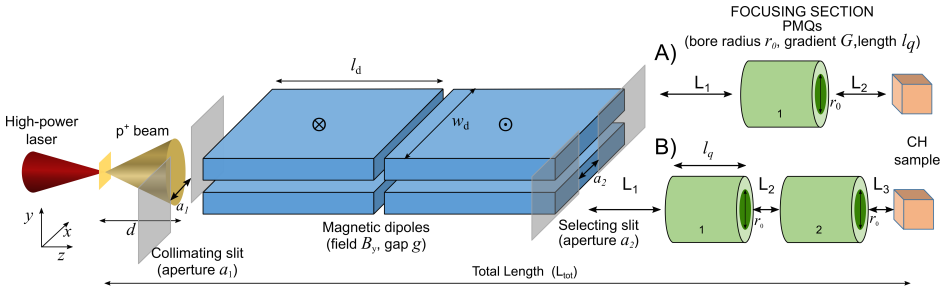

Figure 6.6: The hybrid beamline is composed of an Energy Selector (ES), consisting, in this case of only two dipoles, a collimating slit (a_1) and the central selecting slit (a_2), followed by one or multiple PQMs. The PQM parameters, i.e length l_q, bore radius r_0 (internal diameter) and the gradient G, are optimized in order to focus/defocus the final transverse spot size on the irradiated sample. Two possible focusing sections two scenarios are considered: ES followed by one PQM (A) and ES followed by two PQMs (B). The total distance L_{tot} is maximum 80 cm and the drifts are, respectively, L_1 and L_2 in the case (A) and L_1, L_2, L_3 in case (B).

We limit our beamline design to using only two dipoles. Adding further two dipoles would allow bending the beam back to its original trajectory axis. However, the characteristics of the beam using 4 dipoles are not as competitive as using only 2 dipoles. For the application, it is not relevant to keep the beam on its original propagation axis and we can also gain space according to our geometrical constraints (the vacuum chambers have a typical diameter of around 1-2 m) . Thus, we limit the present study to only 2 dipoles, as it is illustrated in figure 6.6.
As it is known, the main dipole parameters are the length l_d, the width w_d and magnetic field B_0. The dipole parameters, that we use for our ES geometry, are the following: length of $l_d = 10$ cm, a width of $w_d = 10$ cm, a vertical gap size of $g = 0.9$ cm (i.e., the dipole gap in y-direction), and magnetic field $B_y = 0.92$ T (incoming magnetic field for the first dipole and outgoing magnetic field for the second one).
These parameters are similar to what is reported in Scisciò et al. [179], where a selector in the energy range 2–20 MeV has been optimized for reaching a tunable final energy spread between 10-30 % for applications. They are suitable and easily adaptable for our PIXE energy range of interest between 1 and 5 MeV.
After defining the dipoles' parameters, as first step, we have studied the effect of the initial beam divergence on the energy selection process.
The aim of these sets of TSTEP simulations is to indicate a maximum ini-

tial divergence that is compatible with the final beam parameters that are required for the PIXE analysis [76, 158].
TSTEP code allows to use as input, both standard beam distribution that belongs to the library of the program itself [48], as well as a customized initial beam distribution, that can be generated separately and then implemented in the program.
The user can also define, among the requested input lines of the code, other beam parameters, such as the beam charge, the rest mass, initial spatial position of the simulated beam and have also the option to enable or disable the space charge effects.
TSTEP allows modeling the transport elements using simple predefined code lines [48]. It tracks the particles' trajectories that pass through the designed beam transport line and provides, at the end of each run (simulation) as output a complete data set, that contains the information regarding the position, divergence, energy of each particle of the bunch, etc.. for each transport element used. Therefore, the data are very precise and easy to retrieve, analyze and process, using for example numerical tools, such as MATLAB.
Three different proton beams having a uniform energy distribution at 1-3 -5 MeV with energy spread $\Delta E/E_0$ of 100 % have been used as inputs for TSTEP simulations. The black energy spectrum of figure 6.7 (A)-(B)-(C) illustrate our initial input distribution and represent the case of the unselected beams.
Each of the three uniform proton energies distributions show the proton beam conditions at the entrance of the energy selector (ES), i.e. initially we do not take into account the features of the laser-plasma source. We are aware that our simulated beam distribution does not represent the real case scenario, but they are a useful tool for studying only the influence of the intrinsic beam divergence on the final energy spectra and for optimizing the values of the initial collimating slit, as it was done in refs. [41, 179]. (see chapter 5). However, later on, when we estimate the final charge bunch, we explain how we scale and adapt them to realistic values (a typical TNSA proton spectrum).
The initial divergence is determined by the aperture a_1 of the first slit and its distance d from the laser-plasma source. For example, an aperture $a_1 = 500$ μm and an initial divergence of 3 mrad correspond to a distance between the laser proton source and the entrance of the ES of $d = 8$ cm.
Hence, the increase of the divergence of the beam that passes through the first collimating slit is equivalent to vary the distance between the ES and the source and to the tune of the phase space (x,x',y,y') parameters of the initial distributions. For each of them, the initial transverse dimension of the proton beam is given by the aperture of the initial collimating slit, which in all the cases, has a value of 500 μm.

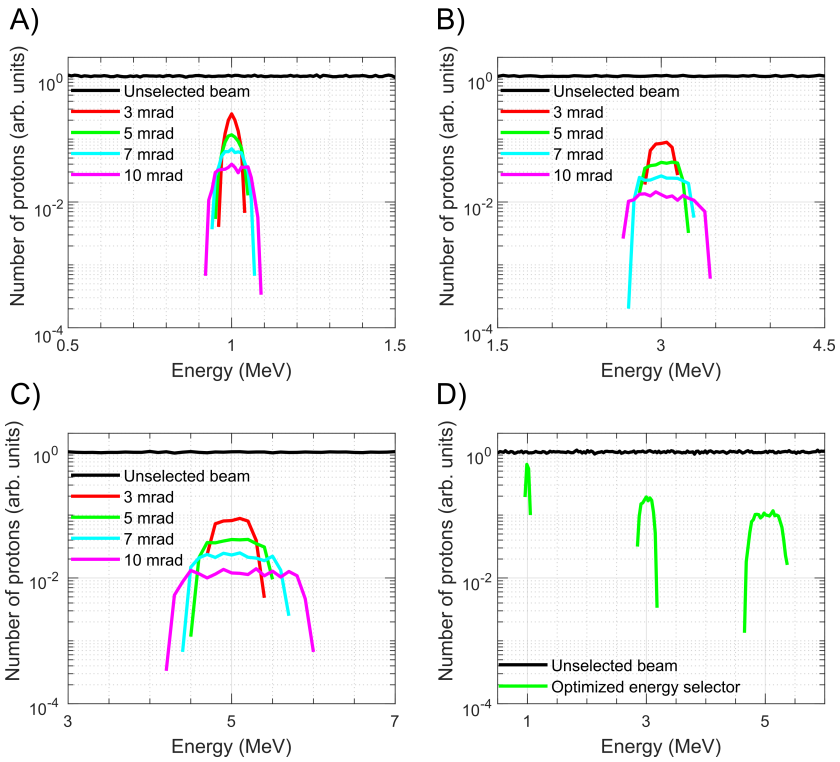

Figure 6.7: Final energy spread of the proton beam passing through the ES, varying the divergence of the initial proton beams distributions. The dark black curve represents the unselected beam at the entrance of the selector, while the colored spectra represent the final energy spread obtainable, after the ES process : case of 1 MeV (A), 3 MeV (B), and 5 MeV (C). The divergence of the initial proton beam distribution has the values: 3 mrad (red color), 5 mrad (green color), 7 mrad (light blue color) and 10 mrad (magenta color). (D) Final energy spectra in the case of 1, 3, and 5 MeV beams, utilizing as initial parameters: divergence 5 mrad and $a_2 = 1000$ μm for 1 MeV beam and divergence 3 mrad and $a_2 = 500$ μm for 3 and 5 MeV beams.

The initial divergence has been varied from a minimum of 3 mrad up to 10 mrad (half angle) for the three energy cases 1, 3, and 5 MeV and the aperture of the central selecting slit has been fixed to an initial value of 500 μm. The final achieved energy spread is represented by the colored lines of the spectra of figure 6.7.
Each colour corresponds to different values of the chosen initial divergence, therefore, different initial proton distribution. As expected, it is shown that the increase in the initial divergence leads to an increase in the final energy spread. It is also clearly visible that this increase starts to be particularly

significant for a divergence $\geq$ 7 mrad for the cases of 3 and 5 MeV, from the simulations results (light blue and magenta colours in panel B and C of figure 6.7).
When selecting 1 MeV protons (figure 6.7 A), the FWHM energy spread ranges from 3% (for 3 mrad initial divergence-red colour) to 11% (10 mrad initial divergence-magenta colour). For the cases of 3 and 5 MeV (respectively figure 6.7 B and figure 6.7 C), an initial divergence of 10 mrad leads to a final energy spread of 23 and 30%, respectively. This is an increase of a factor three with respect to the case of an initial divergence of 3 mrad (8% and 10% final energy spread, for 3 and 5 MeV, respectively).
These results prove, that even if we used a few mrad divergence for the initial proton distribution, the intrinsic divergence [41, 179] of the incoming beam affects the final energy spread obtainable. This is due to the transverse momentum of the incoming protons that can add further deviations with respect to the normal spatial displacement given by only the magnetic field of the dipoles. The trajectories of the particles are influenced by the initial divergence of the incoming beams and this effect is relevant especially for higher energies protons, although their displacement from the original propagation axis, passing through the ES, is smaller compared to low energy particles [179, 41].
Therefore, we define our optimal initial divergence as a compromise between the final energy spread, which is required to be $\leq$ 10%, and the number of particles transmitted through the slit, that obvious decrease in the case of smaller aperture. Moreover, this energy spread range is acceptable, considering that the energy interval 1-5 MeV allows the investigation of the first few μm of CH samples.
An aperture a_1 = 800 μm for the case of 1 MeV has been chosen, obtaining a divergence of 5 mrad. For the same distance ES-laser source of 8 cm, a smaller aperture of a_1 = 500 μm for both 3 and 5 MeV cases have been used in order to have an initial divergence of 3 mrad.
We considered, as second step, the aperture a_2 of the selecting slit for the final energy selection because it allows obtaining a narrow energy spread. The width of the aperture should be a compromise between the desired final energy spread and the number of transmitted particles that is required in order to have a final charge that is comparable to what is implemented on conventional PIXE facilities [76].
A value of a_2 that is too small leads to a strong reduction of the final number of particles that are transmitted through the selector. However, for selecting lower energy particles, which experience a larger displacement by the dipole field, a larger aperture allows having the desired final energy spread $\leq$ 10%. Therefore, a big aperture and with a value of a_2=1000 μm for the central slit

for selecting a 1 MeV beam has been chosen, whereas for the cases of 3 and 5 MeV a smaller value of a_2=500 μm has been chosen. These three different energies are the most employed ones when using PIXE applications [76] and allow obtaining a FWHM final energy spread $\leq 10\%$ in the energy range of our interest.
In panel D of figure 6.7 we illustrate our final results, according to the optimized slit's parameters as function of the desired final beam parameters. For the selected central energies of 1–3–5 MeV, we reach our goal of obtaining the respective selected final energy spread of $\leq 10\%$.
The simulations' results prove that a "relaxed" choice, both in term of the first collimating slit, that has a value of $a_1 = 800$ μm and in term of the second selecting slit that has a value of a_2=1000 μm are acceptable for the case of 1 MeV. Smaller slits (both collimating slit and central slit have values of $a_1 = a_2 = 500$ μm) for the case of 3 and 5 MeV are required and much more suitable for high energy cases.
The transmission efficiency of the beamline η_{BL} has been defined as the ratio between the number of particles that reach the CH sample (final beam) and the number of particles that pass through the initial slit of the ES, in the same final selected energy range.
For the central energy 1 MeV, the value $\eta_{BL} \simeq 12$ % has been obtained, while for the central energies 3 and 5 MeV, the value of $\eta_{BL} \simeq 9\%$. With η_{BL}, the losses induced by the collimation slit (with width a_1) are not taken into account.
These initial losses strongly depend on the characteristics of the laser-plasma interaction that generates the protons, such as the beam energy-divergence distribution at the source, that has been introduced in chapter 1. Since for our study we do not focus on a specific case of laser-plasma interaction conditions, these losses have been estimated with η_S from the solid angle of the collimation slit's aperture.
The horizontal divergence at the source is reduced by the initial collimating slit to a value of 3 mrad (for the cases of 3 and 5 MeV, 5 mrad for the case of 1 MeV). In the vertical plane, the divergence is only limited by the vertical aperture of the dipoles (∼1 cm), corresponding to a half angle of 56 mrad.
Considering that the mean divergence of a TNSA proton beam at the source typically is about 15° half angle [121, 77], corresponding to a solid angle of around 0.21 steradiant, the collimation slit induces a loss of η_S= 0.31% for the energy cases of 3 and 5 MeV.
This value, instead, is higher for the case of 1 MeV protons, i.e. $\eta_S = 0.50\%$ due to the initial horizontal collimation of 5 mrad that is achieved with a wider slit aperture $a_1 = 800$ μm.
The final total transport efficiency (i.e. from the source to the end of the

transport line) is $\eta_T = \eta_S \cdot \eta_{BL}$ and we we obtain $\eta_T = 0.059\%$ for the 1 MeV beam and $\eta_T = 0.028\%$ and for the 3 and 5 MeV beams. This efficiency could be improved using a focusing section before entering the first dipole, as reported in ref. [179].
It is possible, starting from these values, to estimate the bunch charge that is delivered to the sample for each mean energy within one single laser shot. From a typical TNSA proton spectrum [68, 65, 77], obtained using a TW-class laser system with a repetition rate in the range 1–10 Hz, we can set values for the initial charge at the source.
Taking as a benchmark for the number of particles, a typical proton spectrum as produced by a high-power short-pulse laser of new generation [77], and considering the central energies of 1, 3, and 5 MeV with a final energy spread of, respectively, 6, 8, and 10% we obtain about $5 \cdot 10^{11}$, $5 \cdot 10^{11}$, and $1 \cdot 10^{11}$ particles per shot, respectively.
After all the losses along the line, the final charge on the sample is $\sim$ 0.05 nC/shot for 1 MeV, $\sim$0.02 nC/shot for 3 MeV, and $\sim$ 0.004 nC/shot for 5 MeV.
A reference value for the total charge that is used in order to retrieve the PIXE signal from a scanned area of the sample is reported in Pichon et al. [158], where 1.8 nC are used to scan a submillimetric area.
Coupling our beamline with a 1 Hz high-intense laser system allows accumulating a similar final charge in less than 10 min irradiation for the 1–3–5 MeV beams. These time expositions can be further reduced by a factor 10 using the new upcoming 10 Hz high-intensity laser systems [109, 135, 170].
Moreover, using the same benchmark number of protons, the value of the laminar parameter has been calculated. When the protons, especially the beam with a central energy of 1 MeV (lower energy case) passes through the ES, they can experience space charge effects, which can decrease the beam quality. The laminar parameter is expressed as:

$$\rho_{laminar} = \frac{I_{peak} \cdot \sigma_x^2}{I_{Alfven} \cdot \gamma \cdot \epsilon_x^2}$$

Where I_{Alfven} is $(4\pi \cdot \epsilon_0 \cdot m_p \cdot c^3)/e$. Its value allows distinguishing if the beam is emittance pressure dominated or space charge dominated [165], as mentioned in chapter 5.
The possibility of extrapolating a very accurate set of beam data for each transport element given by the particle tracking code TSTEP allows to easily estimate the normalized emittance, the beam size and the peak current of the accelerated proton bunch. Hence, we can evaluate the laminar parameter value, that is around $3.14 \cdot 10^{-4}$ for the most critical case represented by the

proton energy case of 1 MeV (low γ value). Its value is very small and below 1 and this ensures that the space charge effects can be safely neglected.

6.2.3 Optimization of the focusing section based on PQMs

This section describes the results obtained from the second set of simulations that are performed in order to investigate the combination of the ES with the focusing/defocusing PQMs. For optimizing our design, two different scenarios have been considered.
At first, we aim at focusing/defocusing the proton beam using a single quadrupole and for the total length of the beamline (figure 6.6 A). We consider a case with 50 cm total length and a case with 80 cm total length. The first one represents a compact beamline that can be easily adapted to a medium/large vacuum chamber [68, 13, 206], whereas the second one is an extended version, characterized by a range of the final spot size of the beam, which is broader than the compact version (50 cm), but presumably requires an extension if implemented in a chamber of common dimensions. The extension addition can also be desirable for inserting additional diagnostics [22], such as the ones described in chapter 2.
Secondly, we study the case where two quadrupoles are used, in a FODO configuration, in order to focus/defocus the beam. In that case, the total length of the beamline is about 80 cm.
The distance between the source and the sample has a fixed value for each scenario considered: in this way, the proton beam (i.e., change the selected energy or vary the final spot size) is manipulated without the necessity of displacing the sample.
The key design parameters of the PQMs are the bore radius r_0, the magnetic field gradient G, and the magnetic length l_q, as mentioned in chapter 4.
The maximum achievable gradient is related to the magnetic field B_0 on the quadrupole's pole tip and the bore radius, as $G = B_0/r_0$. For our beamline design a PQM length of l_q= 4.5 cm and a bore radius of $r_0 = 1$ cm have been chosen.
The use of rare-earth materials allow obtaining a value of B_0 in the range of hundreds of mT ([57, 145]) and a field gradient in the order of several tens of T/m. Hence, these quadrupole parameters can be easily obtained with the existing permanent magnet technology ([83, 57, 145, 125]) and allow us to keep the dimensions of the beamline compact. Moreover, they are similar to the ones used for the theoretical study of a novel spectrometer design for laser accelerated proton diagnostics, discussed in chapter 4.

Focusing section based on a single quadrupole

We first perform TRACE3D simulations, which evaluate the beam envelope along the line, in order to optimize the focusing section. The obtained results are then compared and validated with TSTEP simulations, performed in the same conditions (i.e. same PQM parameters, same distances between the transport elements).
TRACE3D [111] is a beam optics code that monitor the beam envelope evolution along the transport line, utilizing the beam Twiss parameters (α, β, γ). It allows, as TSTEP, to define the elements that compose the beamline, using predefined code lines, but does not track the single particle trajectories. Furthermore, it includes an optimization routine that indicates the optimal parameters of the line based on matching conditions of the beam Twiss parameters (e.g. between two different positions of the transport line, i.e, in our case, between the exit of the ES and the irradiated CH sample).
The TRACE3D simulations aim at optimizing the position of the quadrupole for obtaining a variable final beam transverse dimension on the sample, ranging from a few mm up to the order of cm.
For the three mean energies of our interest 1, 3 and 5 MeV, the simulated gradient of the quadrupoles is set at G =60 T/m and magnetic length l_q=4.5 cm. This value is obtained from preliminary optimizations with TRACE3D, where different gradients have been exploited. It is a good compromise for operating at these different energies and it is a compatible value with the typical field intensities of commercial PQMs of this size.
The initial values of the Twiss parameters(α, β,γ) are calculated according to the transverse beam geometry at the exit of the ES and represent the initial beam conditions for the TRACE3D simulations.
The horizontal (in x direction) dimension of the beam is determined by the aperture a_2 of the selecting slit of the ES (1 mm for 1 MeV, 500 μm for 3 (figure 6.8 (A)) and 5 MeV), while the vertical dimension (along y) depends by the dipoles's gap g (the vertical aperture is of 0.9 cm).
The results are reported in figure 6.8, where the phase space of the protons at the end of the ES is plotted for the case of 3 MeV beam energy.
For calculating the optimal position of the PQM between the selector and the sample, we set the drift spaces before and after the quadrupole location, indicated in figure 6.8 (A) with L_1 and L_2, as free parameters.
We define conditions on the final Twiss parameters on the y −coordinate with the values $\alpha_y = 0$ and β_y= 0.008 m for obtaining a collimated beam and a decreased final spot size (small irradiated area on the sample).
We repeat the optimization routine with the values $\alpha_y = 28$ and $\beta_y = 1.4804$ m for obtaining a defocused beam, that is, a final spot size with increased

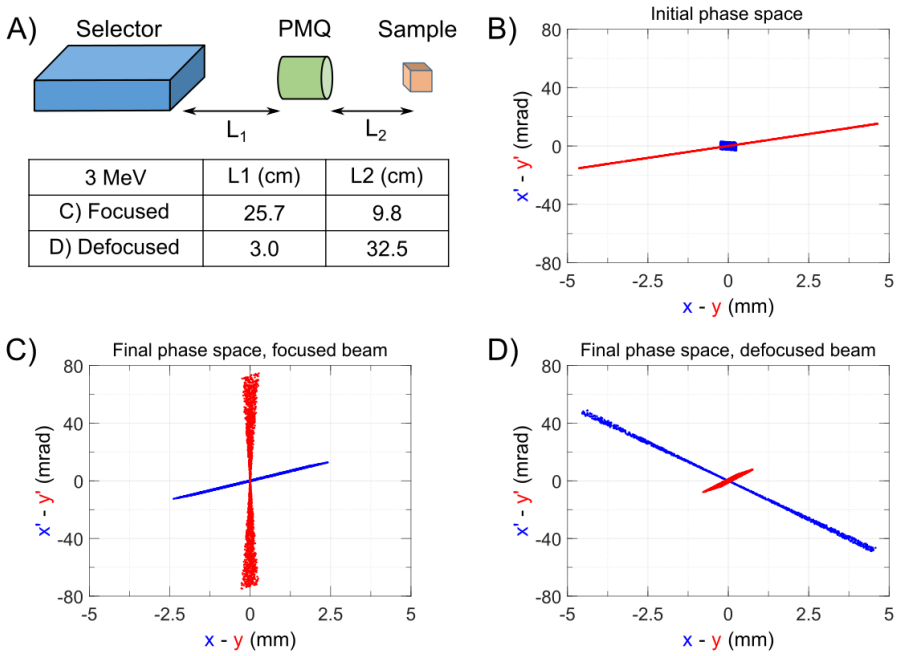

3 MeV	L1 (cm)	L2 (cm)
C) Focused	25.7	9.8
D) Defocused	3.0	32.5

Figure 6.8: (A) Scheme of the simulated beamline. The numbers in the table indicate the values of L_1 and L_2 for the corresponding colored plot in (C) and (D). (B) Initial transverse phase space, as obtained at the exit of the selector that is used for calculating the input Twiss parameters of the TRACE3D simulations. (C) and (D) Final phase space obtained with the TRACE3D optimized distances L_1 and L_2 for a focused and defocused beam, respectively.

dimensions (large irradiated area on the sample).
The numerical values of α_y, β_y reported and respectively associated with the smallest and largest irradiated areas on the sample, are calculated, through Matlab routines, from TSTEP data simulations and are fixed and used as references for the optimization runs.
The total distance between the source and the final longitudinal position (i.e., the position where the irradiated sample is placed) is fixed at 80 cm. The matching routine retrieves, for both, the smallest and the largest spot size, the optimized values of L_1 and L_2.
In figure 6.8 (C) and 6.8 (D), we report, as an example among the three possible energy cases, the final transverse phase space obtained with the TRACE3D optimization routine and refined with a particle tracking simulation with TSTEP, of a beam with a mean energy of 3 MeV passing through a y-focusing PQM that has the following optimized distances: $L_1 = 25.7$ cm,

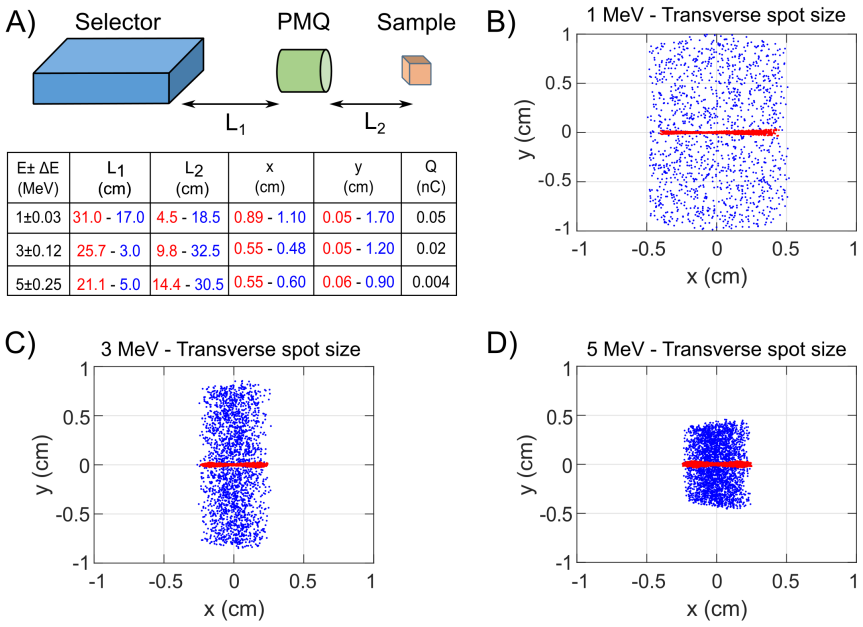

E± ΔE (MeV)	L_1 (cm)	L_2 (cm)	x (cm)	y (cm)	Q (nC)
1±0.03	31.0 - 17.0	4.5 - 18.5	0.89 - 1.10	0.05 - 1.70	0.05
3±0.12	25.7 - 3.0	9.8 - 32.5	0.55 - 0.48	0.05 - 1.20	0.02
5±0.25	21.1 - 5.0	14.4 - 30.5	0.55 - 0.60	0.06 - 0.90	0.004

Figure 6.9: (A) Scheme of the simulated beamline and position of the PQM, charge, energy, and final transverse spot size dimensions for the analyzed cases. (B)–(D) Final transverse dimensions of the focused (red plot) and defocused (blue plot) proton beam for the cases of 1, 3, and 5 MeV, respectively. These spot sizes are obtained with a single PQM after the selector, having a length of 4.5 cm and a magnetic field gradient of 60 T/m. The entire beamline (from the proton source to the CH sample) has a length of 80 cm.

$L_2 = 9.8$ cm for the focused, small final spot size and $L_1 = 3$ cm, $L_2 = 32.5$ cm for the defocused, large final spot size, as indicated in the table of figure 6.8.
These optimized parameters of the beamline are simulated again with the particle tracking code TSTEP that computes the final transverse spot of the beam from a realistic proton distribution, tracking the trajectory of the single macroparticles. We repeat the process for energies 1, 3, and 5 MeV. The results are shown in figure 6.9.
The final energy spread is not altered by the addition of one (or multiple, as discussed later) PQM, i.e the results of figure 6.7 remain unchanged.
As a consequence, the value of η_{BL} does not change when adding these newly optimized PQMs. Thus, no additional particle losses are induced and the overall transport efficiencies are the same as calculated in the previous sec-

tion.
From the plots of figure 6.9 (A), one can see that with this configuration it is possible to scan areas of the CH sample with dimensions in the cm^2 range, as represented in figure 6.9 (B–D) with the blue dots.
Furthermore, it is possible to focus the beam (red plot) and achieve a precision on the vertical axis of < 1 mm, simply by changing the position of the PQM and keeping unvaried all other parameters.
We also study, as an alternative to the 80 cm long beamline, the possibility of reducing the total length in order to design a line that can possibly fit in a medium size experimental chamber. We aim at obtaining a variable final spot size in the same range as for the longer beamline case (from the mm to the cm range) within a total distance of about 50 cm from the laser–plasma source.
Hence, we repeat the same procedure as before: the TRACE3D matching algorithm provides indications for the optimized position (for small/large final spot size) and gradient of the PQM.
These values are then validated by additional TSTEP simulations. The optimized design for the case of a 50 cm long beamline is illustrated in figure 6.10 (A), where the layout is shown and the final beam spot sizes for the energy cases 1–3–5 MeV are plotted.
In figure 6.10 (B)–(D) , the smallest achievable spot size as identified by the red dots and the largest achievable spot size, indicated with the blue dots, are shown.
As before, the used PQM has a length of $l_q = 4.5$ cm and a bore radius $r_0 = 1$ cm. The gradient, instead, needs to be increased to G =100 T/m. This allows to shorten the focal distance and obtain both the biggest and the smallest final transverse spot sizes on the CH sample.
As shown in figure 6.10 (B)–(D), this beamline allows enlarging the final vertical (y-axis) transverse dimension up to about 1 cm for all the analyzed energies. Final spot sizes in the submillimetric range are also obtainable for all mean energies by varying the position of the PQM between the exit of the ES and the end of transport line.
In the 3 MeV case, by placing the PQM 5.3 cm after the exit of the selector, a final vertical dimension of ~ 0.4 mm is obtained, as it can be seen from figure 6.10 (C).
The final energy spread is, with this compact scheme, the same as what is reported in figure 6.7 and the transport efficiency is not influenced by the focusing section. As before, we have $\eta_T = 0.028\%$ (3 and 5 MeV) and $\eta_T =$ 0.059 % (1 MeV).

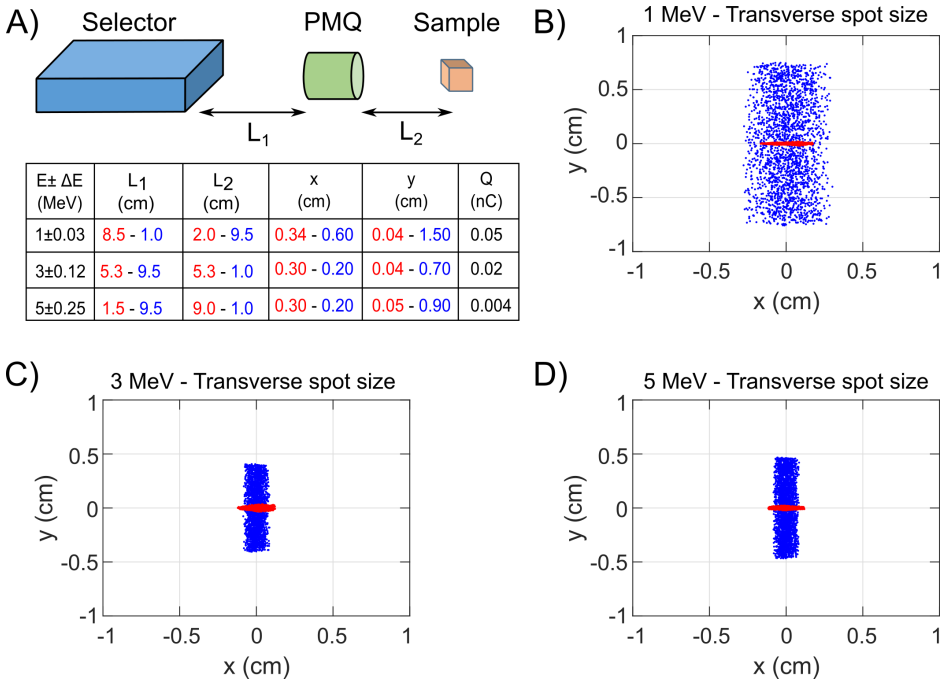

E± ΔE (MeV)	L_1 (cm)	L_2 (cm)	x (cm)	y (cm)	Q (nC)
1±0.03	8.5 - 1.0	2.0 - 9.5	0.34 - 0.60	0.04 - 1.50	0.05
3±0.12	5.3 - 9.5	5.3 - 1.0	0.30 - 0.20	0.04 - 0.70	0.02
5±0.25	1.5 - 9.5	9.0 - 1.0	0.30 - 0.20	0.05 - 0.90	0.004

Figure 6.10: (A) Scheme of the simulated beamline and position of the PQM, charge, energy, and final transverse spot size dimensions for the analyzed cases. (B)–(D). Final transverse dimensions of the focused (red plot) and defocused (blue plot) proton beam for the cases of 1, 3, and 5 MeV, respectively. These spot sizes are obtained with a single PQM after the selector, having a length of 4.5 cm and a magnetic field gradient of 100 T/m. The entire beamline, that goes from the proton source to the CH sample, has a length of 50 cm.

ES followed by two PQMs

We also investigate the possibility of implementing two PQMs after the ES, instead of the focusing section with only one PQM. The same methodology as for the beamlines analyzed before has been used.
In the three energy cases, the two PQMs are in a FODO configuration, where the first quadrupole (closer to the selector) focuses in y (defocuses in x) and the second one focuses in x (defocuses in y).
We firstly perform a series of preliminary TRACE3D simulations in order to find a viable gradient compromise for all three energy cases. The optimized parameters of the previous configuration, that are $l_q = 4.5$ cm, $G = 60$ T/m, and $r_0 = 1$ cm for both PQMs, are suitable for the FODO scheme.
After having optimized the PQM gradients, we have performed additional

TRACE3D simulations in order to optimize their position with respect to the exit of the ES.
Similarly, as before, our goal is to obtain an optimized spacing of the PQMs for a focused (small) and defocused (large) spot size on the irradiated sample, by keeping a fixed distance between the proton source and the sample.
The optimization regarding the gradients and the positions of the PQM pairs, provided by TRACE3D simulations, are compared and tested with TSTEP. The particle tracking results allow a further tuning of the spacing and the final spot sizes for the different energy cases are achieved.
The final spot sizes for the different energy cases are illustrated in figure 6.11.

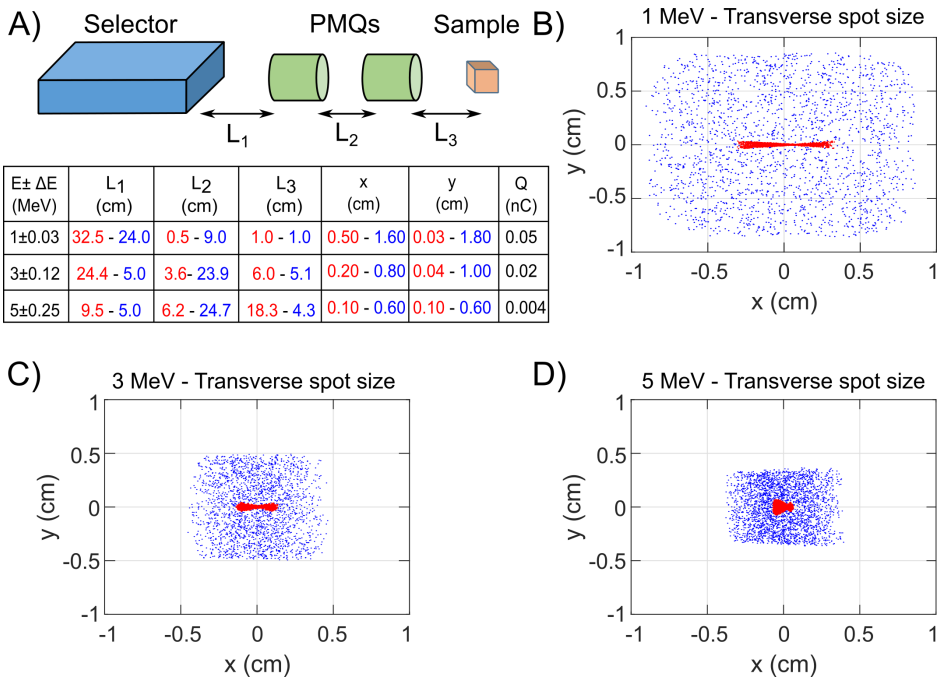

E± ΔE (MeV)	L1 (cm)	L2 (cm)	L3 (cm)	x (cm)	y (cm)	Q (nC)
1±0.03	32.5 - 24.0	0.5 - 9.0	1.0 - 1.0	0.50 - 1.60	0.03 - 1.80	0.05
3±0.12	24.4 - 5.0	3.6- 23.9	6.0 - 5.1	0.20 - 0.80	0.04 - 1.00	0.02
5±0.25	9.5 - 5.0	6.2 - 24.7	18.3 - 4.3	0.10 - 0.60	0.10 - 0.60	0.004

Figure 6.11: (A) Scheme of the simulated beamline and position of the PQM, charge, energy, and final transverse spot size dimensions for the analyzed cases. The entire beamline, that goes from the proton source to the CH sample, has a length of ∼80 cm. (B)–(D) Final transverse dimensions of the focused (red plot) and defocused (blue plot) proton beam for the cases of 1, 3, and 5 MeV, respectively. These spot sizes are obtained with a pair of PQMs in a FODO configuration. They have a length of 4.5 cm and a magnetic field gradient of 60 T/m.

These optimized results allow us to find small/large quasi-symmetric transverse spot sizes with the spacing details that are reported in figure 6.11. The

additional PQM, if carefully optimized, allows to obtain more symmetric spot sizes (in x and y) compared to the previous cases with a single PQM where asymmetric, elongated final spots are obtained.
The final transverse spot sizes are in the cm^2 range. In detail, when the PQM spacing is optimized for obtaining a defocused beam, a final spot size of greater than 1 cm^2 is obtained for the 1 MeV case and about 0.6×0.6 cm for the 5 MeV case, as it can be seen in figure 6.11 (B)–(D).
On the other hand, small spot sizes are obtained, when the spacing is optimized for focusing the beam on the sample. Millimetric dimensions on both transverse axes are reached, for all investigated energies (the smallest spot is achieved for the 5 MeV case with 1 mm on both transverse axes).
In this case with a PQM section implementing a quadrupole pair, the total length of the beamline is $\sim$ 80 cm for all energies, that is, the same order of magnitude as the cases with a single PQM.
Hence, this allows fixing the position of the irradiated sample with respect to the proton source and the variation of the spot size dimension and energy can be achieved by changing the spacing of the PQMs after the selector.
Compared to the scheme with a single PQM, this beamline has the advantage of producing quasi symmetric final spot sizes. This can potentially be an advantage for scanning small areas (below 1 mm) on the sample with a more concentrated charge and an improved precision.
We can perform "layer-by-layer" PIXE analysis without resetting the electrostatic accelerator as it is done conventionally [43, 76].
Furthermore, the number of transmitted particles is unaltered by the addition of one PQM. Hence, the overall (i.e., from the proton source to the sample) transmission efficiency is $\eta_T = 0.028\%$ for the 3 and 5 MeV beams, while for the case of 1 MeV we obtain $\eta_T = 0.059$ %.
After taking into account all the losses along the line, it is possible to estimate, with these values, a final charge on the sample of $\sim$ 0.05 nC/shot for 1 MeV, $\sim$ 0.02 nC/shot for 3 MeV, and $\sim$ 0.004 nC/shot for 5 MeV, as reported in section 6.2.2.
As benchmark for comparing these values to convention PIXE, we consider a total charge of 1.8 nC used to scan a sub-millimetric area [158].
The coupling of our beamline with a 1 Hz high-intense laser system allows reaching a similar final charge in less than 10 min irradiation for all the three energy cases. The new 10 Hz high-intensity laser systems [109, 135, 170] will allow to further decrease these time expositions by a factor 10.

6.3 Discussions and Conclusions

In summary, we presented a compact beamline based on laser-accelerated protons coupled to an ES and focusing quadrupoles, for application of laser-driven PIXE.
The proposed design allows obtaining a feasible and versatile scheme, yielding to a final beam with variable transverse dimensions and a reduced energy spread.
As reported in the previous sections, the simulated structure is compact because the largest version of it is less than 1 m long ($\sim$ 80 cm) and allows selecting proton beams with mean energies in the range 1–5 MeV achieving final FWHM energy spread of $\sim$ 10%, as it is shown in figure 6.7.
The implementation of the PQMs after the selector provides a broad range of final transverse dimensions, with negligible modification to the transport efficiency and final energy spread. With a single PQM, as it was explained in section 6.2.3, we achieved a final vertical dimension of the beam ranging from the cm scale to <1 mm. Using a PQM pair, we obtained more symmetric spot sizes in the same range and we can reach a final transverse spot size greater than 1 cm^2.
The overall transmission efficiency (i.e. from the proton source to the sample) is η_T= 0.028% for the 3 and 5 MeV beams, while for the case of 1 MeV, we obtain η_T = 0.059 %.
These values remained unchanged for all the proposed schemes. As previously mentioned, it is possible to deliver a final charge on the sample of $\sim$0.05 nC/shot for 1 MeV, $\sim$ 0.02 nC/shot for 3 MeV, and $\sim$0.004 nC/shot for 5 MeV.
The coupling of our proposed schemes with a 1 Hz high-intense laser system allows obtaining a similar conventional PIXE final charge (1.8 nC [35]) (see section 6.2.2) within a few tens of min irradiation for all the three energy cases (1–3–5 MeV proton beams). The upcoming generation of 10 Hz high-intensity laser systems [109, 135, 170], will allow to further shorten these time expositions.
In conclusion, especially for scanning a large surface of the sample, the laser-driven PIXE represents a valid alternative to the conventional technique, which requires a pencil scan that lasts several minutes.
Our results provide helpful guidelines and a consistent methodology for designing and optimizing a beamline for laser-accelerated protons in order to exploit ion beam analysis (IBA) for Cultural Heritage.

General conclusions and future perspectives

This thesis deals with laser generated proton sources, approaching their features from the diagnostics, transport, and manipulation points of view.
Within my Ph.D. research activities, different types of diagnostics have been studied. In 2016, I collaborated for the first published calibration curve (OD vs Dose) of the RCF HD-v2 type [40], subject of paper **I**. It has been published in Review of Scientific Instruments [40].
Furthermore, during my participation at the TITAN experimental campaign in August 2016, I was responsible for the diagnostics and I calibrated the Thomson Parabola Spectrometer (TPS), as reported in chapter 2. My contribution on the proton spectra measurements has led me to coauthor the following publications of papers **II** and **III**. The first one is related to the target engineering design [205], reported in section 1.3.2, while the second one is a Scientific Report paper on Laser-Generated Proton Beams for High-Precision Ultra-Fast Crystal Synthesis[13].
Within the framework of laser driven proton acceleration, I have dealt with topics related to laser ion diagnostics and laser-driven hybrid beamlines for applications.
Concerning the study related to diagnostics, my participation in the Low energy Ion acceleration campaign (LEIA) allowed me to deal with laser driven ion diagnostics, such as the MCP and CR-39. In detail, the experiment arrangement of the detection system has represented a useful reference for the description of the model, that has been used for the numerical results, discussed in chapter 4.
The details of the design and optimization of a novel spectrometer for laser driven ion diagnostics have been presented in chapter 4. The proposed design is composed of a quadrupole coupled with a constant electric field. The main advantages in this choice are given by the achievable compactness of the structure and the gain in energy spectral information (low proton energy range), without significant loss in terms of energy resolution.

I have also analyzed the contribution of the carbon ions, that are co-generated with the protons in laser-plasma interactions. In this case, we have observed that a set of quadrupoles with a strong gradient can provide an overall improvement in terms of the energy resolution, separation of the traces, compactness, and detectable energy for both proton and carbon ions.
These results can be further improved by using high-order magnetic elements, such as octupole, decapole, etc... However, they are not worthy in terms of the balance between advantages and costs after the case of the decapole, as explained in chapter 4. Hence, the quadrupole represents the most feasible (easy to manufacture and assemble) choice, among the analyzed ones.
The replacement of the quadrupole, compared to existing combinations [201, 103] allows constantly to scale and enlarge the detectable achievable proton energy, without significant losses in terms of the energy resolution.
In this thesis work, another aspect that has been studied is the design and implementation of a hybrid proton beamline for applications, as described in chapter 5. These studies represent a valid and reliable way to transport and manipulate the laser driven proton sources in order to match the required final proton parameters for applications, such as the ones of paper **III**.
My participation in the TITAN experimental campaign allowed me to approach the field of laser-driven proton beam applications. During this campaign, the first laser-PIXE measurement has been performed[16]. Over the last four years, these experimental results have catalyzed a strong interest of the community in this application, as reported in refs. [154, 17, 133]. Within this context, I worked on the design and optimization of a laser-PIXE hybrid beamline for material science applications, as discussed in chapter 6.
The simulated compact hybrid beamline scheme has been investigated, using numerical tools that are standard codes in the conventional accelerators community [111, 48]. The proposed schemes are versatile and compact (the biggest one is less than 1 m), as described in section 6.2.3. They allow to obtain feasibility both in terms of final proton transverse spot sizes and, in addition, to reduce the proton energy spread, i.e improve the final proton beam yield.
The proposed laser-driven hybrid beamline includes an energy selector (ES) followed by PQMs. The ES allows selecting typical conventional PIXE proton energies of 1, 3, 5 MeV, reaching a final energy spread of around 10 %. The addition of the PQMs allows to obtain feasibility in the final transverse spot sizes, i.e beam vertical dimension from less than 1 mm up to cm-scale, without significant variation in terms of energy spread and overall transmission efficiency.
The estimated overall transmission efficiency from the proton source to the CH sample is η_T= 0.028% for the 3 and 5 MeV beams, while for the case of

1 MeV, $\eta_T = 0.059$ % is obtained. For instance in order to obtain a total charge of 1.8 nC [152], that is used to scan a sample's sub-millimeter region in conventional PIXE, a final charge of ∼0.05 nC/shot, ∼ 0.02 nC/shot, and ∼0.004 nC/shot for 1 MeV, 3 MeV and 5 MeV have been calculated [77] with the η_T values respectively.
The coupling of the beamline with a 1 Hz high-intense laser system will allow reaching a similar final charge (1.8 nC [35] in conventional PIXE) in less than 10 minutes irradiation for all three energy cases (1, 3, 5 MeV). Furthermore, the coupling with the upcoming 10 Hz high-intensity laser systems [109, 170], such as the ones described in chapter 3, will allow obtaining the same final charge on the sample in less than 1 minute.
Hence, the theoretical analysis of these hybrid proton beamlines provides practical guidelines for the design of a dedicated transport line for improving and further investigating the laser-PIXE application.
These numerical results are the subject of paper **IV**. They have been presented at the European Conference on Laser-Matter interaction (ECLIM 2018, Rethymno, Greece), summer schools and internal ELI-ALPS research institute events, as shown in the list of attendance of international conferences and schools. It has been published in 2019 on Laser particle beams [137].
The preliminary results discussed in chapter 4 have been presented at the European Advanced Accelerator Concepts Workshop (EAAC 2019, Elba, Italy). They have been finalized within the last year of my doctoral studies and a manuscript is under preparation (paper **V**).
As future prospects of this work, we plan to purchase, assemble and test in the near future the design of the proposed spectrometer in chapter 4 in order to be able to compare the theoretical predictions with experimental data. Similar sets of quadrupoles can be also implemented for laser driven proton hybrid beamline for applications, as discussed in chapter 6. We aim at finalizing the Low energy Ion acceleration (LEIA) data analysis, described in chapter 3. It is the first laser-generated proton observation at ELI-ALPS and a pilot experiment in the perspective of a new concept for the design of a neutron source for a laser-based transmutator [110, 222].
In conclusion, the numerical and experimental results may serve as a major asset for future advancements, both in laser-driven ion diagnostics as well as in the implementation of laser-driven proton beamlines for applications. I hope that this work can contribute to take a step further in the fascinating world of accelerator physics.

Appendices

Appendix A

The Thomson parabola spectrometer structure

A Thomson parabola spectrometer (TPS) is composed by a sequence and/or a combination of a magnetic and electric field. In this appendix, we will describe in details the equations of motion that characterize the movement of a charged particle inside a TPS.

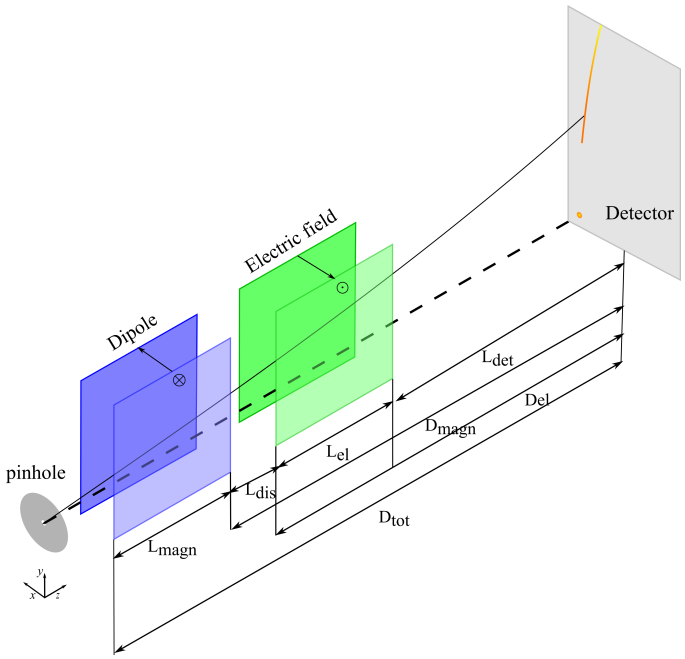

Figure A.1: Thomson parabola spectrometer structure. It is composed by: an ion pinhole, a magnetic section, an electric field and an ion detector. Figure adapted from [2].

We recalls the same scheme illustrated in chapter 2, as starting point for describing the reference system. The z axis is the propagation axis, while the magnetic and electric field are directed on the x axis and they are parallel to each other and perpendicular to the direction of propagation, i.e. B =(B,0,0) and E = (-E,0,0). The charged particle that move inside the TPS experiences the Lorentz's force

$$\vec{F} = q(E + \vec{v} \times \vec{B}). \tag{A.1}$$

We analyze separately the contribution of the magnetic (section A.1) and electric sections (section A.2).

A.1 Magnetic deflection

The deflection due to the magnetic field is related to the velocities of the particles. We, first analyze the contribution given by the magnetic section (see figure A.2).

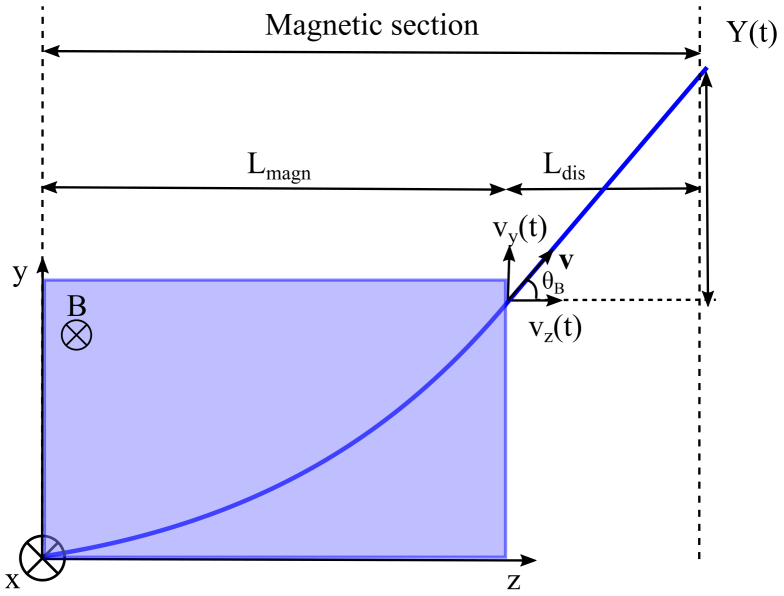

Figure A.2: Description of the magnetic section of the Thomson parabola spectrometer structure. Figure adapted from [9].

The particle has velocity $\vec{v}$= (v_x,v_y,v_z). Starting from the eq. A.1, we can have the first derivative of $\vec{v}$:

$$\dot{v_x} = 0 \tag{A.2}$$

$$\dot{v_y} = \omega v_z \tag{A.3}$$

$$\dot{v_z} = -\omega v_y \tag{A.4}$$

where $\omega = \frac{qB}{m}$. The second derivative respect to time of v_y, combining the above equations, becomes:

$$\ddot{v_y} = \omega(-\omega v_y) = -\omega^2 v_y \tag{A.5}$$

As solution of these set of differential equations, we start from

$$v_y = C_1 \cos(\omega t) + C_2 \sin(\omega t) \tag{A.6}$$

With the initial condition $v_y(t = 0) = 0$, i.e C_1=0. Hence, eq A.6 becomes:

$$v_y = C_2 \sin(\omega t) \tag{A.7}$$

Replacing eq A.7 in A.4, we obtain:

$$\dot{v_z} = -\omega C_2 \sin(\omega t) \tag{A.8}$$

with the solutions:

$$v_z = C_2 \cos(\omega t) \tag{A.9}$$

The initial condition $v_z(0)$=v_0 (initial velocity in the propagation direction), leads to $C_2 = v_0$. The particle's velocity inside the magnetic field is:

$$v_x = 0 \tag{A.10}$$

$$v_y = v_0 \cos(\omega t) \tag{A.11}$$

$$v_z = v_0 \sin(\omega t) \tag{A.12}$$

At the exit of the magnetic field, our conditions are: $z = L_{magn}$ and t=T_B. Then, integrating eq. A.12, we obtain:

$$z = \frac{v_0 \sin(\omega t)}{\omega} + C_1 \tag{A.13}$$

Since z(0)=0 and z(T_B)=L_{magn}, as consequence $C_1 = 0$ and:

$$L_{magn} = \frac{v_0 \sin(\omega T_B)}{\omega} \tag{A.14}$$

From eq. A.14, we can derive the value of T_B as function of L_{magn}:

$$T_B = \frac{1}{\omega}[\arcsin\left(\frac{L_{magn}\omega}{v_0}\right)] \tag{A.15}$$

Integrating eq. A.11 and considering our initial conditions y(0)=0 , we can find the value of the deflection y:

$$y = \frac{v_0}{\omega}\left\{-\cos\left[\arcsin\left(\frac{L_{magn}\omega}{v_0}\right)\right] + 1\right\} \tag{A.16}$$

The solution at the exit of the magnetic section is the following[92]:

$$x = 0 \tag{A.17}$$

$$y = \frac{v_0}{\omega}\left\{-\cos\left[\arcsin\left(\frac{L_{magn}\omega}{v_0}\right)\right] + 1\right\} \tag{A.18}$$

$$z = L_{magn} \tag{A.19}$$

Now, we consider the drift L_{dis}, we have an angle θ_B between v_y and v_z. Considering a simple trigonometrical formula we can obtain:

$$\frac{v_y}{v_z}|_{L_{magn}} = \tan(\omega T_B) \tag{A.20}$$

Knowing the expression of T_B as function of L_{magn}, we obtain:

$$\frac{v_y}{v_z}|_{L_{magn}} = \tan\left(\frac{\omega L_{magn}}{v_0}\right) \tag{A.21}$$

The y contribution given by the drift is:

$$L_{dis}\tan\left(\omega T_B\right) \tag{A.22}$$

Hence, at the end, we derive the set of equations due to the magnetic field with length L_{magn} and drift with length L_{dis} reported in chapter 2:

$$x = 0 \tag{A.23}$$

$$y = \frac{v_0}{\omega}\left\{1 - \cos\left[\arcsin\left(\frac{L_{magn}\omega}{v_0}\right)\right] + 1\right\} + L_{dis}\tan\left[\arcsin\left(\frac{L_{magn}\omega}{v_0}\right)\right] \tag{A.24}$$

$$z = L_{magn} + L_{dis} \tag{A.25}$$

A.2 Electric deflection

After deriving the equations of x, y, z due to the presence of a magnetic field and a drift, we analyze the electric section (see figure A.3. The electric field is directed on the x axis).
The starting point is the following equation:

$$\dot{v_x} = -\frac{qE}{m} \tag{A.26}$$

integrating in time, from eq. A.26 we obtain:

$$v_x = -\frac{qEt'}{m} + C_1 \tag{A.27}$$

From the initial condition $v_x(t' = 0) = 0$, i.e C_1=0;
Integrating in time the eq. A.27, we obtain the solution:

$$x = \frac{-qE_x t'^2}{2m} \tag{A.28}$$

that represents the electric contribution, at the end of the section.

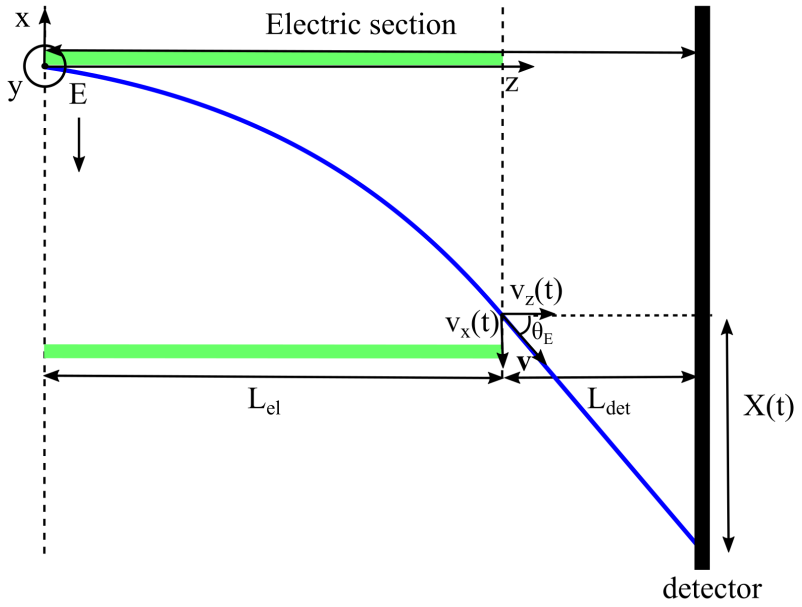

Figure A.3: Description of the electric section of the Thomson parabola spectrometer structure.

In this case, similar to the magnetic case, the angle θ_E can be calculated as:

$$\tan(\theta_E) = \frac{v_x}{v_z}|_{L_E} \tag{A.29}$$

Using eq. A.28 and eq. A.29, we obtain

$$t' = T_E = \frac{L_E}{v_0 \cos(\omega T_B)} \tag{A.30}$$

Hence, eq A.29 becomes:

$$\tan(\theta_E) = \frac{v_x}{v_z}|_{L_E} = \frac{qEL_E}{mv_0^2 \cos^2(\omega T_B)} \tag{A.31}$$

and the final set of equations, solution of the motion of the particles , that include all the contributions is:

$$x = \frac{-qE_x T_E^2}{2m} + L_{det} \tan\theta_E \tag{A.32}$$

$$y = \frac{v_0}{\omega}\left\{1 - \cos\left[\arcsin\left(T_B\right)\right] + 1\right\} + (L_{dis} + L_E + L_{det}) \tan\left[\arcsin\left(T_B\right)\right] \tag{A.33}$$

$$z = L_{magn} + L_{dis} + L_E + L_{det} \tag{A.34}$$

where T_E is given by eq. A.30 and T_B is given by eq A.15.

Small angle approximation

Using the small angle approximation, $\cos(x)$, $\sin(x)$, $\arcsin(x)$ can be written, respectively:

$$\cos(x) \simeq 1 - \frac{x^2}{2} \tag{A.35}$$

$$\tan(x) \simeq x \tag{A.36}$$

$$\arcsin(x) \simeq x \tag{A.37}$$

Therefore, eq. A.33 and eq. A.32 can be simplified:

$$x = \frac{-qE_x L_E^2}{2mv_0^2 \cos^2(\omega T_B)} + \frac{L_{det} qE_x L_E}{mv_0^2 \cos^2(\omega T_B)} \tag{A.38}$$

$$y = \frac{\omega L_{magn}^2}{2v_0} + (L_{dis} + L_E + L_{det})\frac{\omega L_{magn}}{v_0} \tag{A.39}$$

Taking into account that T_B can be written as L_{magn}/v_0 , $\omega = \frac{qB}{m}$ and introducing the kinetic energy $v_0^2 = 2E_{kin}m$, we can further simplify the equations:

$$x = \frac{-qE_x L_E^2}{2E_{kin}\cos^2(\omega T_B)} + \frac{L_{det} qE_x L_E}{2E_{kin}\cos^2(\omega T_B)} \tag{A.40}$$

$$y = \frac{qBL_{magn}^2}{2\sqrt{2E_{kin}m}} + (D_{tot})\frac{qBL_{magn}}{2\sqrt{2E_{kin}m}} \tag{A.41}$$

The magnetic and electric field are usually combined ($L_{magn} = L_{el}$), hence we arrive to the commonly used equations:

$$x = \frac{-qE_x L_E}{2E_{kin}}(\frac{L_E}{2} + L_{det}) \tag{A.42}$$

$$y = \frac{qBL_{magn}}{\sqrt{2E_{kin}m}}(\frac{L_{magn}}{2} + D_{tot}) \tag{A.43}$$

This represents the derivation of the equations reported in chapter 2.

Bibliography

[1] A Alejo, H Ahmed, A Green, SR Mirfayzi, M Borghesi, and S Kar. Recent advances in laser-driven neutron sources. *Il nuovo cimento C*, 38(6):1–7, 2015.

[2] A Alejo, D Gwynne, D Doria, H Ahmed, DC Carroll, RJ Clarke, D Neely, GG Scott, M Borghesi, and S Kar. Recent developments in the Thomson Parabola Spectrometer diagnostic for laser-driven multi-species ion sources. *Journal of Instrumentation*, 11(10):C10005, 2016.

[3] A Alejo, S Kar, H Ahmed, AG Krygier, D Doria, R Clarke, J Fernandez, RR Freeman, J Fuchs, A Green, et al. Characterisation of deuterium spectra from laser driven multi-species sources by employing differentially filtered image plate detectors in Thomson spectrometers. *Review of Scientific Instruments*, 85(9):093303, 2014.

[4] A Alejo, S Kar, A Tebartz, H Ahmed, S Astbury, DC Carroll, J Ding, D Doria, A Higginson, P McKenna, et al. High resolution Thomson Parabola Spectrometer for full spectral capture of multi-species ion beams. *Review of Scientific Instruments*, 87(8):083304, 2016.

[5] Matthew Allen, Pravesh K Patel, Andrew Mackinnon, Dwight Price, Scott Wilks, and Edward Morse. Direct experimental evidence of back-surface ion acceleration from laser-irradiated gold foils. *Physical review letters*, 93(26):265004, 2004.

[6] P Antici, M Fazi, A Lombardi, M Migliorati, L Palumbo, P Audebert, and J Fuchs. Numerical study of a linear accelerator using laser-generated proton beams as a source. *Journal of Applied Physics*, 104(12):124901, 2008.

[7] P Antici, M Migliorati, A Mostacci, L Picardi, L Palumbo, and C Ronsivalle. A compact post-acceleration scheme for laser-generated protons. *Physics of Plasmas*, 18(7):073103, 2011.

[8] P Antici, M Migliorati, A Mostacci, L Picardi, L Palumbo, and C Ronsivalle. Sensitivity study in a compact accelerator for laser-generated protons. *Journal of Plasma Physics*, 78(4):441–445, 2012.

[9] Patrizio Antici. *Laser-acceleration of high-energy short proton beams and applications*. PhD thesis, Ed. Ecole Polytechnique, 2007.

[10] Ph Barberet, S Incerti, F Andersson, F Delalee, L Serani, and Ph Moretto. Technical description of the CENBG nanobeam line. *Nuclear Instruments and Methods in Physics Research Section B: Beam Interactions with Materials and Atoms*, 267(12-13):2003–2007, 2009.

[11] M. Barberio and P. Antici. Laser-PIXE using laser-accelerated proton beams. *Scientific Reports*, 9(1):6855, dec 2019.

[12] M. Barberio, M. Scisciò, S. Vallières, F. Cardelli, S. N. Chen, G. Famulari, T. Gangolf, G. Revet, A. Schiavi, M. Senzacqua, and P. Antici. Laser-accelerated particle beams for stress testing of materials. *Nature Communications*, 9(1):372, dec 2018.

[13] M. Barberio, M. Scisciò, S. Vallières, S. Veltri, A. Morabito, and P. Antici. Laser-Generated Proton Beams for High-Precision Ultra-Fast Crystal Synthesis. *Scientific Reports*, 7(1):12522, dec 2017.

[14] M. Barberio, M. Scisciò, S. Veltri, and P. Antici. Fabrication of nanostructured targets for improved laser-driven proton acceleration. *Superlattices and Microstructures*, 95:159–163, jul 2016.

[15] M. Barberio, S. Vallières, M. Scisciò, G. Kolhatkar, A. Ruediger, and P. Antici. Graphitization of diamond by laser-accelerated proton beams. *Carbon*, 139:531–537, nov 2018.

[16] M. Barberio, S. Veltri, M. Scisciò, and P. Antici. Laser-Accelerated Proton Beams as Diagnostics for Cultural Heritage. *Scientific Reports*, 7(1):40415, dec 2017.

[17] Marianna Barberio, Massimiliano Scisciò, Emmanouil Skantzakis, and Patrizio Antici. Carbon-Based Nanostructured Film Materials for High-Intense Laser-Matter Interaction Experiments. *Advanced Engineering Materials*, 21(2):1800777, feb 2019.

[18] Fred Begay and David W Forslund. Acceleration of multi-species ions in CO_2 laser-produced plasmas: Experiments and theory. *The Physics of Fluids*, 25(9):1675–1685, 1982.

[19] Rustam Berezov, Olivier Delferriere, Jerome Fils, Yannick Gauthier, Ralph Hollinger, Klaus Knie, Carl Kleffner, and Olivier Tuske. Status of high intensity proton injector for Facility for Antiproton and Ion Research. *Review of Scientific Instruments*, 90(12):123309, 2019.

[20] Loïc Bertrand, Sebastian Schöeder, Demetrios Anglos, Mark BH Breese, Koen Janssens, Mehdi Moini, and Aliz Simon. Mitigation strategies for radiation damage in the analysis of ancient materials. *TrAC Trends in Analytical Chemistry*, 66:128–145, 2015.

[21] M Blanco, MT Flores-Arias, C Ruiz, and M Vranic. Table-top laser-based proton acceleration in nanostructured targets. *New Journal of Physics*, 19(3):033004, 2017.

[22] P.R. Bolton, M. Borghesi, C. Brenner, D.C. Carroll, C. De Martinis, F. Fiorini, A. Flacco, V. Floquet, J. Fuchs, P. Gallegos, D. Giove, J.S. Green, S. Green, B. Jones, D. Kirby, P. McKenna, D. Neely, F. Nuesslin, R. Prasad, S. Reinhardt, M. Roth, U. Schramm, G.G. Scott, S. Ter-Avetisyan, M. Tolley, G. Turchetti, and J.J. Wilkens. Instrumentation for diagnostics and control of laser-accelerated proton (ion) beams. *Physica Medica*, 30(3):255–270, may 2014.

[23] M Borghesi, A Bigongiari, S Kar, A Macchi, L Romagnani, P Audebert, J Fuchs, T Toncian, O Willi, SV Bulanov, et al. Laser-driven proton acceleration: source optimization and radiographic applications. *Plasma Physics and Controlled Fusion*, 50(12):124040, 2008.

[24] M Borghesi, AJ Mackinnon, D Hv Campbell, DG Hicks, S Kar, Pv K Patel, D Price, L Romagnani, A Schiavi, and O Willi. Multi-MeV proton source investigations in ultraintense laser-foil interactions. *Physical Review Letters*, 92(5):055003, 2004.

[25] Marco Borghesi. Laser-driven ion acceleration: State of the art and emerging mechanisms. *Nuclear Instruments and Methods in Physics Research Section A: Accelerators, Spectrometers, Detectors and Associated Equipment*, 740:6–9, 2014.

[26] Rimantas Budriūnas, Tomas Stanislauskas, Jonas Adamonis, Aidas Aleknavičius, Gediminas Veitas, Darius Gadonas, Stanislovas Balickas, Andrejus Michailovas, and Arūnas Varanavičius. 53 W average power CEP-stabilized OPCPA system delivering 5.5 TW few cycle pulses at 1 kHz repetition rate. *Optics express*, 25(5):5797–5806, 2017.

[27] R Bugoi, I Poll, Gh Mănucu-Adameşteanu, T Calligaro, L Pichon, and C Pacheco. PIXE–PIGE analyses of Byzantine glass bracelets (10th–13th centuries AD) from Isaccea, Romania. *Journal of Radioanalytical and Nuclear Chemistry*, 307(2):1021–1036, 2016.

[28] Stepan S. Bulanov, Valery Yu. Bychenkov, Vladimir Chvykov, Galina Kalinchenko, Dale William Litzenberg, Takeshi Matsuoka, Alexander G. R. Thomas, Louise Willingale, Victor Yanovsky, Karl Krushelnick, and Anatoly Maksimchuk. Generation of GeV protons from 1 PW laser interaction with near critical density targets. *Physics of Plasmas*, 17(4):043105, apr 2010.

[29] SV Bulanov, T Zh Esirkepov, Francesco Califano, Y Kato, TV Liseikina, K Mima, NM Naumova, K Nishihara, Francesco Pegoraro, H Ruhl, et al. Generation of collimated beams of relativistic ions in laser-plasma interactions. *Journal of Experimental and Theoretical Physics Letters*, 71(10):407–411, 2000.

[30] S.V Bulanov, T.Zh Esirkepov, V.S Khoroshkov, A.V Kuznetsov, and F Pegoraro. Oncological hadrontherapy with laser ion accelerators. *Physics Letters A*, 299(2-3):240–247, jul 2002.

[31] T Burris-Mog, K Harres, F Nürnberg, S Busold, M Bussmann, O Deppert, G Hoffmeister, M Joost, M Sobiella, A Tauschwitz, et al. Laser accelerated protons captured and transported by a pulse power solenoid. *Physical Review Special Topics-Accelerators and Beams*, 14(12):121301, 2011.

[32] S. Busold, D. Schumacher, O. Deppert, C. Brabetz, S. Frydrych, F. Kroll, M. Joost, H. Al-Omari, A. Blažević, B. Zielbauer, I. Hofmann, V. Bagnoud, T. E. Cowan, and M. Roth. Focusing and transport of high-intensity multi-MeV proton bunches from a compact laser-driven source. *Physical Review Special Topics - Accelerators and Beams*, 16(10):101302, oct 2013.

[33] S Busold, D Schumacher, O Deppert, C Brabetz, F Kroll, A Blažević, V Bagnoud, and M Roth. Commissioning of a compact laser-based proton beam line for high intensity bunches around 10 mev. *Physical Review Special Topics-Accelerators and Beams*, 17(3):031302, 2014.

[34] John Charles Butcher. *The numerical analysis of ordinary differential equations: Runge-Kutta and general linear methods*. Wiley-Interscience, 1987.

[35] T Calligaro, V Gonzalez, and L Pichon. PIXE analysis of historical paintings: is the gain worth the risk? *Nuclear Instruments and Methods in Physics Research Section B: Beam Interactions with Materials and Atoms*, 363:135–143, 2015.

[36] DC Carroll, P Brummitt, D Neely, Filip Lindau, Olle Lundh, C-G Wahlström, and P McKenna. A modified Thomson parabola spectrometer for high resolution multi-MeV ion measurements—Application to laser-driven ion acceleration. *Nuclear Instruments and Methods in Physics Research Section A: Accelerators, Spectrometers, Detectors and Associated Equipment*, 620(1):23–27, 2010.

[37] W Cayzac, A Frank, A Ortner, V Bagnoud, MM Basko, S Bedacht, C Bläser, A Blažević, S Busold, O Deppert, et al. Experimental discrimination of ion stopping models near the Bragg peak in highly ionized matter. *Nature communications*, 8(1):1–7, 2017.

[38] Francis F Chen et al. *Introduction to plasma physics and controlled fusion*, volume 1. Springer, 1984.

[39] Hui Chen, AU Hazi, R van Maren, SN Chen, J Fuchs, M Gauthier, S Le Pape, JR Rygg, and R Shepherd. An imaging proton spectrometer for short-pulse laser plasma experiments. *Review of Scientific instruments*, 81(10):10D314, 2010.

[40] S N Chen, M Gauthier, M Bazalova-Carter, S Bolanos, S Glenzer, R Riquier, G Revet, P Antici, A Morabito, A Propp, and J. Fuchs. Absolute dosimetric characterization of Gafchromic EBT3 and HDv2 films using commercial flat-bed scanners and evaluation of the scanner response function variability. *Review of Scientific Instruments*, 87(7):073301, 2016.

[41] S. N. Chen, M. Gauthier, D. P. Higginson, S. Dorard, F. Mangia, R. Riquier, S. Atzeni, J.-R. Marquès, and J. Fuchs. Monochromatic short pulse laser produced ion beam using a compact passive magnetic device. *Review of Scientific Instruments*, 85(4):043504, apr 2014.

[42] M Chiari. Fundamentals of the Particle Induced Gamma-ray Emission (PIGE) technique, experimental procedures and examples of PIGE analysis, Joint ICTP-IAEA Workshop on Nuclear Data for Analytical Applications, 2013. `http://indico.ictp.it/event/a12218/session/23/contribution/14/material/0/0.pdf`.

[43] M. Chiari, A. Migliori, and P.A. Mandò. Investigation of beam-induced damage to ancient ceramics in external-PIXE measurements. *Nuclear Instruments and Methods in Physics Research Section B: Beam Interactions with Materials and Atoms*, 188(1-4):151–155, apr 2002.

[44] Shivani Choudhary. *Study of Laser-driven Ion Acceleration Through Relativistic Self-Induced Transparency.* PhD thesis, BIRLA INSTITUTE OF TECHNOLOGY AND SCIENCE, PILANI, 2019.

[45] EL Clark, K Krushelnick, JR Davies, Matthew Zepf, M Tatarakis, FN Beg, A Machacek, PA Norreys, MIK Santala, I Watts, et al. Measurements of energetic proton transport through magnetized plasma from intense laser interactions with solids. *Physical Review Letters*, 84(4):670, 2000.

[46] A Climent-Font, A Muñoz-Martin, MD Ynsa, and A Zucchiatti. Quantification of sodium in ancient Roman glasses with ion beam analysis. *Nuclear Instruments and Methods in Physics Research Section B: Beam Interactions with Materials and Atoms*, 266(4):640–648, 2008.

[47] TE Cowan, J Fuchs, H Ruhl, A Kemp, P Audebert, M Roth, R Stephens, I Barton, A Blazevic, E Brambrink, et al. Ultralow emittance, multi-MeV proton beams from a laser virtual-cathode plasma accelerator. *Physical review letters*, 92(20):204801, 2004.

[48] K. R. Crandall and Rusthoi. TRACE3D LANL Report, LA-UR-97-886 (1997), 1997. url:https://laacg.lanl.gov/laacg/services/traceman.pdf.

[49] AS Cucoanes, DL Balabanski, F Canova, P Cuong, F Negoita, F Puicea, and KA Tanaka. On the potential of laser driven isotope generation at ELI-NP for positron emission tomography. In *Medical Applications of Laser-Generated Beams of Particles IV: Review of Progress and Strategies for the Future*, volume 10239, page 102390B. International Society for Optics and Photonics, 2017.

[50] Hiroyuki Daido, Mamiko Nishiuchi, and Alexander S Pirozhkov. Review of laser-driven ion sources and their applications. *Reports on progress in physics*, 75(5):056401, 2012.

[51] Colin N Danson, Constantin Haefner, Jake Bromage, Thomas Butcher, Jean-Christophe F Chanteloup, Enam A Chowdhury, Almantas Galvanauskas, Leonida A Gizzi, Joachim Hein, David I Hillier, et al. Petawatt and exawatt class lasers worldwide. *High Power Laser Science and Engineering*, 7, 2019.

[52] G Deconninck, G Demortier, and F Bodart. Prompt gamma-ray spectroscopy and its use in elemental analysis. *Some aspects of chemical methods in nuclear studies*, 1981.

[53] Slobodan Devic, Jan Seuntjens, Gyorgy Hegyi, Ervin B Podgorsak, Christopher G Soares, Assen S Kirov, Imad Ali, Jeffrey F Williamson, and Angel Elizondo. Dosimetric properties of improved GafChromic films for seven different digitizers. *Medical physics*, 31(9):2392–2401, 2004.

[54] Slobodan Devic, Nada Tomic, and David Lewis. Reference radiochromic film dosimetry: review of technical aspects. *Physica Medica*, 32(4):541–556, 2016.

[55] Jean-Claude Diels, W Rudolph, PF Liao, and P Kelley. Ultrashort laser pulse phenomena. Optics and Photonics, 1996.

[56] B. Dromey, M. Coughlan, L. Senje, M. Taylor, S. Kuschel, B. Villagomez-Bernabe, R. Stefanuik, G. Nersisyan, L. Stella, J. Kohanoff, M. Borghesi, F. Currell, D. Riley, D. Jung, C.-G. Wahlström, C.L.S. Lewis, and M. Zepf. Picosecond metrology of laser-driven proton bursts. *Nature Communications*, 7(1):10642, apr 2016.

[57] T. Eichner, F. Grüner, S. Becker, M. Fuchs, D. Habs, R. Weingartner, U. Schramm, H. Backe, P. Kunz, and W. Lauth. Miniature magnetic devices for laser-based, table-top free-electron lasers. *Physical Review Special Topics - Accelerators and Beams*, 10(8):082401, aug 2007.

[58] T Esirkepov, M Borghesi, SV Bulanov, G Mourou, and T Tajima. Highly efficient relativistic-ion generation in the laser-piston regime. *Physical review letters*, 92(17):175003, 2004.

[59] Timur Esirkepov, Katsunobu Nishihara, Sergei V Bulanov, and Francesco Pegoraro. Three-dimensional relativistic electromagnetic subcycle solitons. *Physical review letters*, 89(27):275002, 2002.

[60] Lyndon Evans and Philip Bryant. LHC machine. *Journal of instrumentation*, 3(08):S08001, 2008.

[61] GC Ezeh, IB Obioh, OI Asubiojo, M Chiari, S Nava, G Calzolai, F Lucarelli, and C Nuviadenu. The complementarity of PIXE and PIGE techniques: a case study of size segregated airborne particulates collected from a Nigeria city. *Applied Radiation and Isotopes*, 103:82–92, 2015.

[62] Frederico Fiúza, Anne Stockem, Elisabetta Boella, RA Fonseca, LO Silva, D Haberberger, Sergei Tochitsky, Chao Gong, Warren B Mori, and Chandrasekar Joshi. Laser-driven shock acceleration of monoenergetic ion beams. *Physical Review Letters*, 109(21):215001, 2012.

[63] RL Fleischer, PB Price, and RM Walker. Ion explosion spike mechanism for formation of charged-particle tracks in solids. *Journal of applied Physics*, 36(11):3645–3652, 1965.

[64] KA Flippo, J Workman, DC Gautier, S Letzring, RP Johnson, and T Shimada. Scaling laws for energetic ions from the commissioning of the new Los Alamos National Laboratory 200 TW Trident laser. *Review of Scientific Instruments*, 79(10):10E534, 2008.

[65] S. Fourmaux, S. Buffechoux, B. Albertazzi, D. Capelli, A. Lévy, S. Gnedyuk, L. Lecherbourg, P. Lassonde, S. Payeur, P. Antici, H. Pépin, R. S. Marjoribanks, J. Fuchs, and J. C. Kieffer. Investigation of laser-driven proton acceleration using ultra-short, ultra-intense laser pulses. *Physics of Plasmas*, 20(1):013110, jan 2013.

[66] J Fuchs, P Antici, E d'Humières, E Lefebvre, M Borghesi, E Brambrink, CA Cecchetti, Malte Kaluza, Victor Malka, M Manclossi, et al. Laser-driven proton scaling laws and new paths towards energy increase. *Nature physics*, 2(1):48–54, 2006.

[67] J Fuchs, Y Sentoku, E d'Humières, TE Cowan, J Cobble, P Audebert, A Kemp, A Nikroo, P Antici, E Brambrink, et al. Comparative spectra and efficiencies of ions laser-accelerated forward from the front and rear surfaces of thin solid foils. *Physics of plasmas*, 14(5):053105, 2007.

[68] J. Fuchs, Y. Sentoku, S. Karsch, J. Cobble, P. Audebert, A. Kemp, A. Nikroo, P. Antici, E. Brambrink, A. Blazevic, E. M. Campbell, J. C. Fernández, J.-C. Gauthier, M. Geissel, M. Hegelich, H. Pépin, H. Popescu, N. Renard-LeGalloudec, M. Roth, J. Schreiber, R. Stephens, and T. E. Cowan. Comparison of Laser Ion Acceleration from the Front and Rear Surfaces of Thin Foils. *Physical Review Letters*, 94(4):045004, feb 2005.

[69] S Gaillard, J Fuchs, N Renard-Le Galloudec, and TE Cowan. Study of saturation of CR39 nuclear track detectors at high ion fluence and of associated artifact patterns. *Review of scientific instruments*, 78(1):013304, 2007.

[70] M Gauthier, CB Curry, Sebastian Göde, F-E Brack, JB Kim, MJ MacDonald, J Metzkes, L Obst, M Rehwald, C Rödel, et al. High repetition rate, multi-MeV proton source from cryogenic hydrogen jets. *Applied Physics Letters*, 111(11):114102, 2017.

[71] Gesellschaft für Schwerionenforschung (GSI) website. Laser Ion Generation, Handling and Transport (LIGHT) at GSI. url:`https://www.gsi.de/work/forschung/appamml/plasmaphysikphelix/experimente/light.htm`.

[72] Paul Gibbon. *Short pulse laser interactions with matter: an introduction*. World Scientific, 2005.

[73] SJ Gitomer, RD Jones, F Begay, AW Ehler, JF Kephart, and R Kristal. Fast ions and hot electrons in the laser–plasma interaction. *The Physics of fluids*, 29(8):2679–2688, 1986.

[74] L Giuntini, M Massi, and S Calusi. The external scanning proton microprobe of Firenze: a comprehensive description. *Nuclear Instruments and Methods in Physics Research Section A: Accelerators, Spectrometers, Detectors and Associated Equipment*, 576(2-3):266–273, 2007.

[75] Leonida Antonio Gizzi, Ralph Assmann, Petra Koester, and Antonio Giulietti. *Laser-Driven Sources of High Energy Particles and Radiation: Lecture Notes of the" Capri" Advanced Summer School*, volume 231. Springer Nature, 2019.

[76] N. Grassi, A. Migliori, P. A. Mandò, and H. Calvo del Castillo. Differential PIXE measurements for the stratigraphic analysis of the painting Madonna dei fusi by Leonardo Da Vinci. *X-Ray Spectrometry*, 34(4):306–309, jul 2005.

[77] J. S. Green, A. P. L. Robinson, N. Booth, D. C. Carroll, R. J. Dance, R. J. Gray, D. A. MacLellan, P. McKenna, C. D. Murphy, D. Rusby, and L. Wilson. High efficiency proton beam generation through target thickness control in femtosecond laser-plasma interactions. *Applied Physics Letters*, 104(21):214101, may 2014.

[78] MM Günther, Alexander Britz, RJ Clarke, K Harres, G Hoffmeister, F Nürnberg, A Otten, A Pelka, M Roth, and K Vogt. Nais: Nuclear activation-based imaging spectroscopy. *Review of scientific instruments*, 84(7):073305, 2013.

[79] A Gurevich, D Anderson, and H Wilhelmsson. Ion acceleration in an expanding rarefied plasma with non-maxwellian electrons. *Physical Review Letters*, 42(12):769, 1979.

[80] AV Gurevich, LV Pariiskaya, and LP Pitaevskii. Self-similar motion of rarefied plasma. *Sov. Phys. JETP*, 22(2):449–454, 1966.

[81] D Gwynne, S Kar, D Doria, H Ahmed, M Cerchez, J Fernandez, RJ Gray, JS Green, F Hanton, DA MacLellan, et al. Modified Thomson spectrometer design for high energy, multi-species ion sources. *Review of Scientific Instruments*, 85(3):033304, 2014.

[82] Dan Haberberger, Sergei Tochitsky, Frederico Fiuza, Chao Gong, Ricardo A Fonseca, Luis O Silva, Warren B Mori, and Chan Joshi. Collisionless shocks in laser-produced plasma generate monoenergetic high-energy proton beams. *Nature Physics*, 8(1):95–99, 2012.

[83] Klaus Halbach. SUPERFISH?A COMPUTER PROGRAM FOR EVALUATION OF RF CAVITIES WITH CYLINDRICAL SYMMETRY, 1976. `https://escholarship.org/uc/item/1d26z7d0`.

[84] Klaus Halbach. Design of permanent multipole magnets with oriented rare earth cobalt material. *Nuclear instruments and methods*, 169(1):1–10, 1980.

[85] K Harres, M Schollmeier, E Brambrink, P Audebert, A Blažević, K Flippo, DC Gautier, M Geißel, BM Hegelich, F Nürnberg, et al. Development and calibration of a Thomson parabola with microchannel plate for the detection of laser-accelerated MeV ions. *Review of Scientific Instruments*, 79(9):093306, 2008.

[86] Stephen P Hatchett, Curtis G Brown, Thomas E Cowan, Eugene A Henry, Joy S Johnson, Michael H Key, Jeffrey A Koch, A Bruce Langdon, Barbara F Lasinski, Richard W Lee, et al. Electron, photon, and ion beams from the relativistic interaction of Petawatt laser pulses with solid targets. *Physics of Plasmas*, 7(5):2076–2082, 2000.

[87] Björn Manuel Hegelich, BJ Albright, J Cobble, K Flippo, S Letzring, M Paffett, H Ruhl, Jörg Schreiber, RK Schulze, and JC Fernández. Laser acceleration of quasi-monoenergetic MeV ion beams. *Nature*, 439(7075):441–444, 2006.

[88] M Hegelich, Stefan Karsch, Georg Pretzler, D Habs, Klaus Witte, W Guenther, M Allen, A Blazevic, J Fuchs, JC Gauthier, et al. MeV

ion jets from short-pulse-laser interaction with thin foils. *Physical review letters*, 89(8):085002, 2002.

[89] DS Hey, MH Key, AJ Mackinnon, AG MacPhee, PK Patel, RR Freeman, LD Van Woerkom, and CM Castaneda. Use of GafChromic film to diagnose laser generated proton beams. *Review of Scientific Instruments*, 79(5):053501, 2008.

[90] A Higginson, RJ Gray, M King, RJ Dance, SDR Williamson, NMH Butler, R Wilson, R Capdessus, C Armstrong, JS Green, et al. Near-100 MeV protons via a laser-driven transparency-enhanced hybrid acceleration scheme. *Nature communications*, 9(1):724, 2018.

[91] Stanley Humphries. *Charged particle beams*. Courier Corporation, 2013.

[92] John David Jackson. *Classical electrodynamics*. John Wiley & Sons, 2007.

[93] D Jahn, D Schumacher, C Brabetz, J Ding, S Weih, F Kroll, FE Brack, U Schramm, A Blažević, and M Roth. First application studies at the laser-driven LIGHT beamline: Improving proton beam homogeneity and imaging of a solid target. *Nuclear Instruments and Methods in Physics Research Section A: Accelerators, Spectrometers, Detectors and Associated Equipment*, 909:173–176, 2018.

[94] Tae Won Jeong, PK Singh, C Scullion, H Ahmed, P Hadjisolomou, C Jeon, H Yun, KF Kakolee, M Borghesi, and S Ter-Avetisyan. CR-39 track detector for multi-MeV ion spectroscopy. *Scientific Reports*, 7(1):1–8, 2017.

[95] Tae Won Jeong, PK Singh, C Scullion, H Ahmed, KF Kakolee, P Hadjisolomou, A Alejo, S Kar, M Borghesi, and S Ter-Avetisyan. Experimental evaluation of the response of micro-channel plate detector to ions with 10s of mev energies. *Review of Scientific Instruments*, 87(8):083301, 2016.

[96] Daniel Jung. *Ion acceleration from relativistic laser nano-target interaction*. PhD thesis, lmu, 2012.

[97] Daniel Jung, Rainer Hörlein, DC Gautier, S Letzring, Daniel Kiefer, K Allinger, BJ Albright, R Shah, S Palaniyappan, L Yin, et al. A novel high resolution ion wide angle spectrometer. *Review of Scientific Instruments*, 82(4):043301, 2011.

[98] Daniel Jung, Rainer Hörlein, Daniel Kiefer, S Letzring, DC Gautier, U Schramm, C Hübsch, R Öhm, BJ Albright, JC Fernandez, et al. Development of a high resolution and high dispersion Thomson parabola. *Review of Scientific Instruments*, 82(1):013306, 2011.

[99] Malte Kaluza, Jörg Schreiber, Marko IK Santala, George D Tsakiris, Klaus Eidmann, Jürgen Meyer-ter Vehn, and Klaus J Witte. Influence of the laser prepulse on proton acceleration in thin-foil experiments. *Physical review letters*, 93(4):045003, 2004.

[100] S Kar, M Borghesi, L Romagnani, S Takahashi, Anatoly Zayats, Victor Malka, S Fritzler, and A Schiavi. Analysis of latent tracks for MeV protons in CR-39. *Journal of applied physics*, 101(4):044510, 2007.

[101] S Kar, A Green, H Ahmed, A Alejo, APL Robinson, M Cerchez, R Clarke, D Doria, S Dorkings, J Fernandez, et al. Beamed neutron emission driven by laser accelerated light ions. *New Journal of Physics*, 18(5):053002, 2016.

[102] Satyabrata Kar, Hamad Ahmed, Rajendra Prasad, Mirela Cerchez, Stephanie Brauckmann, Bastian Aurand, Giada Cantono, Prokopis Hadjisolomou, Ciaran L. S. Lewis, Andrea Macchi, Gagik Nersisyan, Alexander P. L. Robinson, Anna M. Schroer, Marco Swantusch, Matt Zepf, Oswald Willi, and Marco Borghesi. Guided post-acceleration of laser-driven ions by a miniature modular structure. *Nature Communications*, 7(1):10792, dec 2016.

[103] Sadaoki Kojima, Shunsuke Inoue, Thanh Hung Dinh, Noboru Hasegawa, Michiaki Mori, Hironao Sakaki, Yoichi Yamamoto, Teru Sasaki, Keiichiro Shiokawa, Kotaro Kondo, et al. Compact Thomson parabola spectrometer with variability of energy range and measurability of angular distribution for low-energy laser-driven accelerated ions. *Review of Scientific Instruments*, 91(5):053305, 2020.

[104] Stephan D Kraft, Lieselotte Obst, Josefine Metzkes-Ng, Hans-Peter Schlenvoigt, Karl Zeil, Sylvain Michaux, Denis Chatain, Jean-Paul Perin, Sophia N Chen, Julien Fuchs, Maxence Gauthier, Thomas E Cowan, and Ulrich Schramm. First demonstration of multi-MeV proton acceleration from a cryogenic hydrogen ribbon target. *Plasma Physics and Controlled Fusion*, 60(4):044010, apr 2018.

[105] William Kruer. *The physics of laser plasma interactions*. CRC Press, 2019.

[106] WLl Kruer and Kent Estabrook. J× B heating by very intense laser light. *The Physics of fluids*, 28(1):430–432, 1985.

[107] K Krushelnick, EL Clark, M Zepf, JR Davies, FN Beg, A Machacek, MIK Santala, M Tatarakis, I Watts, PA Norreys, et al. Energetic proton production from relativistic laser interaction with high density plasmas. *Physics of Plasmas*, 7(5):2055–2061, 2000.

[108] AG Krygier, JT Morrison, S Kar, H Ahmed, A Alejo, R Clarke, J Fuchs, A Green, D Jung, A Kleinschmidt, et al. Selective deuterium ion acceleration using the Vulcan petawatt laser. *Physics of Plasmas*, 22(5):053102, 2015.

[109] Sergei Kühn, Mathieu Dumergue, Subhendu Kahaly, Sudipta Mondal, Miklós Füle, Tamás Csizmadia, Balázs Farkas, Balázs Major, Zoltán Várallyay, Eric Cormier, Mikhail Kalashnikov, Francesca Calegari, Michele Devetta, Fabio Frassetto, Erik Månsson, Luca Poletto, Salvatore Stagira, Caterina Vozzi, Mauro Nisoli, Piotr Rudawski, Sylvain Maclot, Filippo Campi, Hampus Wikmark, Cord L Arnold, Christoph M Heyl, Per Johnsson, Anne L'Huillier, Rodrigo Lopez-Martens, Stefan Haessler, Maïmona Bocoum, Frederik Boehle, Aline Vernier, Gregory Iaquaniello, Emmanuel Skantzakis, Nikos Papadakis, Constantinos Kalpouzos, Paraskevas Tzallas, Franck Lépine, Dimitris Charalambidis, Katalin Varjú, Károly Osvay, and Giuseppe Sansone. The ELI-ALPS facility: the next generation of attosecond sources. *Journal of Physics B: Atomic, Molecular and Optical Physics*, 50(13):132002, jul 2017.

[110] Gábor Szabó Károly Osvay. Neutron generation with few cycle lasers - the Hungarian project, 2019. `https://mta.hu/data/11_Osztaly/HIREK/Osvay_Transmut_USZ_191106.pdf`.

[111] L. M. Young. TSTEP. *LANL Report LA-UR-96-1835*, 1996.

[112] V. Lazic, M. Vadrucci, R. Fantoni, M. Chiari, A. Mazzinghi, and A. Gorghinian. Applications of laser-induced breakdown spectroscopy for cultural heritage: A comparison with X-ray Fluorescence and Particle Induced X-ray Emission techniques. *Spectrochimica Acta Part B: Atomic Spectroscopy*, 149:1–14, nov 2018.

[113] Andrea Macchi. A review of laser-plasma ion acceleration. *arXiv preprint arXiv:1712.06443*, 2017.

[114] Andrea Macchi, Marco Borghesi, and Matteo Passoni. Ion acceleration by superintense laser-plasma interaction. *Reviews of Modern Physics*, 85(2):751, 2013.

[115] Andrea Macchi, Silvia Veghini, Tatyana V Liseykina, and Francesco Pegoraro. Radiation pressure acceleration of ultrathin foils. *New Journal of Physics*, 12(4):045013, 2010.

[116] AJ Mackinnon, M Borghesi, S Hatchett, MH Key, PK Patel, H Campbell, A Schiavi, R Snavely, SC Wilks, and O Willi. Effect of plasma scale length on multi-MeV proton production by intense laser pulses. *Physical Review Letters*, 86(9):1769, 2001.

[117] AJ Mackinnon, PK Patel, RP Town, MJ Edwards, T Phillips, SC Lerner, DW Price, D Hicks, MH Key, S Hatchett, et al. Proton radiography as an electromagnetic field and density perturbation diagnostic. *Review of Scientific Instruments*, 75(10):3531–3536, 2004.

[118] Theodore H Maiman. Addendum 10: Reprint of TH Maiman,"Stimulated Optical Radiation in Ruby," Nature, 187, 493-494 (August 6, 1960). In *The Laser Inventor*, pages 299–301. Springer, 2018.

[119] Anatoly Maksimchuk, Shaoting Gu, Kirk Flippo, Donald Umstadter, and V Yu Bychenkov. Forward ion acceleration in thin films driven by a high-intensity laser. *Physical Review Letters*, 84(18):4108, 2000.

[120] Victor Malka, Sven Fritzler, Erik Lefebvre, Emmanuel D'Humières, Régis Ferrand, Georges Grillon, Claude Albaret, Samuel Meyroneinc, Jean-Paul Chambaret, Andre Antonetti, and Danièle Hulin. Practicability of proton therapy using compact laser systems. *Medical Physics*, 31(6):1587–1592, may 2004.

[121] A. Mancic, J. Robiche, P. Antici, P. Audebert, C. Blancard, P. Combis, F. Dorchies, G. Faussurier, S. Fourmaux, M. Harmand, R. Kodama, L. Lancia, S. Mazevet, M. Nakatsutsumi, O. Peyrusse, V. Recoules, P. Renaudin, R. Shepherd, and J. Fuchs. Isochoric heating of solids by laser-accelerated protons: Experimental characterization and self-consistent hydrodynamic modeling. *High Energy Density Physics*, 6(1):21–28, jan 2010.

[122] P. A. Mandò, M. E. Fedi, and N. Grassi. The present role of small particle accelerators for the study of Cultural Heritage. *The European Physical Journal Plus*, 126(4):41, apr 2011.

[123] D Margarone, O Klimo, IJ Kim, J Prokupek, J Limpouch, TM Jeong, T Mocek, J Pšikal, HT Kim, J Proška, et al. Laser-driven proton acceleration enhancement by nanostructured foils. *Physical review letters*, 109(23):234801, 2012.

[124] Daniele Margarone, G. Cirrone, Giacomo Cuttone, Antonio Amico, Lucio Andò, Marco Borghesi, Stepan Bulanov, Sergei Bulanov, Denis Chatain, Antonín Fajstavr, Lorenzo Giuffrida, Filip Grepl, Satyabrata Kar, Josef Krasa, Daniel Kramer, Giuseppina Larosa, Renata Leanza, Tadzio Levato, Mario Maggiore, Lorenzo Manti, Guliana Milluzzo, Boris Odlozilik, Veronika Olsovcova, Jean-Paul Perin, Jan Pipek, Jan Psikal, Giada Petringa, Jan Ridky, Francesco Romano, Bedřich Rus, Antonio Russo, Francesco Schillaci, Valentina Scuderi, Andriy Velyhan, Roberto Versaci, Tuomas Wiste, Martina Zakova, and Georg Korn. ELIMAIA: A Laser-Driven Ion Accelerator for Multidisciplinary Applications. *Quantum Beam Science*, 2(2):8, apr 2018.

[125] F. Marteau, A. Ghaith, P. N'Gotta, C. Benabderrahmane, M. Valléau, C. Kitegi, A. Loulergue, J. Vétéran, M. Sebdaoui, T. André, G. Le Bec, J. Chavanne, C. Vallerand, D. Oumbarek, O. Cosson, F. Forest, P. Jivkov, J. L. Lancelot, and M. E. Couprie. Variable high gradient permanent magnet quadrupole (QUAPEVA). *Applied Physics Letters*, 111(25):253503, dec 2017.

[126] U. Masood, M. Bussmann, T. E. Cowan, W. Enghardt, L. Karsch, F. Kroll, U. Schramm, and J. Pawelke. A compact solution for ion beam therapy with laser accelerated protons. *Applied Physics B*, 117(1):41–52, oct 2014.

[127] Jason E Matney, Brent C Parker, Daniel W Neck, Greg Henkelmann, and Isaac I Rosen. Evaluation of a commercial flatbed document scanner and radiographic film scanner for radiochromic EBT film dosimetry. *Journal of applied clinical medical physics*, 11(2):198–208, 2010.

[128] Aodhan McIlvenny, Domenico Doria, Lorenzo Romagnani, Hamad Ahmed, Philip Martin, SDR Williamson, EJ Ditter, O Ettlinger, GS Hicks, P McKenna, et al. Absolute calibration of microchannel plate detector for carbon ions up to 250 MeV. *Journal of Instrumentation*, 14(04):C04002, 2019.

[129] P McKenna, KWD Ledingham, I Spencer, T McCany, RP Singhal, C Ziener, PS Foster, EJ Divall, CJ Hooker, D Neely, et al. Characteri-

zation of multiterawatt laser-solid interactions for proton acceleration. *Review of scientific instruments*, 73(12):4176–4184, 2002.

[130] M. Menu, T. Calligaro, J. Salomon, G. Amsel, and J. Moulin. The dedicated accelerator-based IBA facility AGLAE at the Louvre. *Nuclear Instruments and Methods in Physics Research Section B: Beam Interactions with Materials and Atoms*, 45(1-4):610–614, jan 1990.

[131] G Milluzzo, V Scuderi, A Alejo, AG Amico, N Booth, M Borghesi, GAP Cirrone, G Cuttone, D Doria, J Green, et al. A new energy spectrum reconstruction method for time-of-flight diagnostics of high-energy laser-driven protons. *Review of Scientific Instruments*, 90(8):083303, 2019.

[132] G Milluzzo, V Scuderi, AG Amico, M Borghesi, GAP Cirrone, G Cuttone, M De Napoli, D Doria, J Dostal, G Larosa, et al. Laser-accelerated ion beam diagnostics with TOF detectors for the ELIMED beamline. *Journal of Instrumentation*, 12(02):C02025, 2017.

[133] F Mirani, A Maffini, F Casamichiela, A Pazzaglia, A Formenti, D Dellasega, V Russo, D Vavassori, D Bortot, M Huault, et al. Integrated quantitative PIXE analysis and EDX spectroscopy using a laser-driven particle source. *Science Advances*, 7(3):eabc8660, 2020.

[134] Junji Miyahara, Kenji Takahashi, Yoshiyuki Amemiya, Nobuo Kamiya, and Yoshinori Satow. A new type of X-ray area detector utilizing laser stimulated luminescence. *Nuclear Instruments and Methods in Physics Research Section A: Accelerators, Spectrometers, Detectors and Associated Equipment*, 246(1-3):572–578, 1986.

[135] Sudipta Mondal, Mojtaba Shirozhan, Naveed Ahmed, Maïmouna Bocoum, Frederik Boehle, Aline Vernier, Stefan Haessler, Rodrigo Lopez-Martens, François Sylla, Cedric Sire, Fabien Quéré, Kwinten Nelissen, Katalin Varjú, Dimitris Charalambidis, and Subhendu Kahaly. Surface plasma attosource beamlines at ELI-ALPS. *Journal of the Optical Society of America B*, 35(5):A93, may 2018.

[136] Patrick Mora. Plasma expansion into a vacuum. *Physical Review Letters*, 90(18):185002, 2003.

[137] A Morabito, M Scisciò, S Veltri, M Migliorati, and P Antici. Design and optimization of a laser-PIXE beamline for material science applications. *Laser and Particle Beams*, 37(4):354–363, 2019.

[138] John T Morrison, Scott Feister, Kyle D Frische, Drake R Austin, Gregory K Ngirmang, Neil R Murphy, Chris Orban, Enam A Chowdhury, and WM Roquemore. Corrigendum: MeV proton acceleration at kHz repetition rate from ultra-intense laser liquid interaction (2018 New J. Phys. 20 022001). *New Journal of Physics*, 20(6):069501, 2018.

[139] JT Morrison, C Willis, RR Freeman, and L Van Woerkom. Design of and data reduction from compact Thomson parabola spectrometers. *Review of Scientific Instruments*, 82(3):033506, 2011.

[140] Gerard A Mourou, Toshiki Tajima, and Sergei V Bulanov. Optics in the relativistic regime. *Reviews of modern physics*, 78(2):309, 2006.

[141] Yoshihiro Murakami, Yoneyoshi Kitagawa, Yasuhiko Sentoku, Michiaki Mori, Ryosuke Kodama, Kazuo A Tanaka, Kunioki Mima, and Tatsuhiko Yamanaka. Observation of proton rear emission and possible gigagauss scale magnetic fields from ultra-intense laser illuminated plastic target. *Physics of Plasmas*, 8(9):4138–4143, 2001.

[142] Shu Nakamura, Masahiro Ikegami, Yoshihisa Iwashita, Toshiyuki Shirai, Hiromu Tongu, Hikaru Souda, Hiroyuki Daido, Michiaki Mori, Masataka Kado, Akito Sagisaka, Koichi Ogura, Mamiko Nishiuchi, Satoshi Orimo, Yukio Hayashi, Akifumi Yogo, Alexander S. Pirozhkov, Sergei V. Bulanov, Timur Esirkepov, Akira Nagashima, Toyoaki Kimura, Toshiki Tajima, Takeshi Takeuchi, Atsushi Fukumi, Zhong Li, and Akira Noda. High-Quality Laser-Produced Proton Beam Realized by the Application of a Synchronous RF Electric Field. *Japanese Journal of Applied Physics*, 46(No. 29):L717–L720, jul 2007.

[143] Tatsufumi Nakamura, Sergei V Bulanov, Timur Zh Esirkepov, and Masaki Kando. High-energy ions from near-critical density plasmas via magnetic vortex acceleration. *Physical review letters*, 105(13):135002, 2010.

[144] K Nemoto, Anatoly Maksimchuk, Sudeep Banerjee, K Flippo, G Mourou, D Umstadter, and V Yu Bychenkov. Laser-triggered ion acceleration and table top isotope production. *Applied Physics Letters*, 78(5):595–597, 2001.

[145] M Nirkko, S Braccini, A Ereditato, I Kreslo, P Scampoli, and M Weber. An adjustable focusing system for a 2 MeV H^- ion beam line based on permanent magnet quadrupoles. *Journal of Instrumentation*, 8(02):P02001–P02001, feb 2013.

[146] Azam Niroomand-Rad, Charles Robert Blackwell, Bert M Coursey, Kenneth P Gall, James M Galvin, William L McLaughlin, Ali S Meigooni, Ravinder Nath, James E Rodgers, and Christopher G Soares. Radiochromic film dosimetry: recommendations of AAPM radiation therapy committee task group 55. *Medical physics*, 25(11):2093–2115, 1998.

[147] M. Nishiuchi, I. Daito, M. Ikegami, H. Daido, M. Mori, S. Orimo, K. Ogura, A. Sagisaka, A. Yogo, A. S. Pirozhkov, H. Sugiyama, H. Kiriyama, H. Okada, S. Kanazawa, S. Kondo, T. Shimomura, M. Tanoue, Y. Nakai, H. Sasao, D. Wakai, H. Sakaki, P. Bolton, I. W. Choi, J. H. Sung, J. Lee, Y. Oishi, T. Fujii, K. Nemoto, H. Souda, A. Noda, Y. Iseki, and T. Yoshiyuki. Focusing and spectral enhancement of a repetition-rated, laser-driven, divergent multi-MeV proton beam using permanent quadrupole magnets. *Applied Physics Letters*, 94(6):061107, feb 2009.

[148] M Nishiuchi, H Sakaki, T Hori, PR Bolton, K Ogura, A Sagisaka, A Yogo, M Mori, S Orimo, AS Pirozhkov, et al. Measured and simulated transport of 1.9 MeV laser-accelerated proton bunches through an integrated test beam line at 1 Hz. *Physical Review Special Topics-Accelerators and Beams*, 13(7):071304, 2010.

[149] Muhammad Noaman-ul Haq, Hamad Ahmed, Thomas Sokollik, Lule Yu, Zezhou Liu, Xiaohui Yuan, Fang Yuan, Mohammad Mirzaie, Xulei Ge, Liming Chen, et al. Statistical analysis of laser driven protons using a high-repetition-rate tape drive target system. *Physical Review Accelerators and Beams*, 20(4):041301, 2017.

[150] F Nürnberg, M Schollmeier, E Brambrink, A Blažević, DC Carroll, K Flippo, DC Gautier, M Geissel, K Harres, BM Hegelich, et al. Radiochromic film imaging spectroscopy of laser-accelerated proton beams. *Review of scientific instruments*, 80(3):033301, 2009.

[151] Frank Nürnberg. *Laser-accelerated proton beams as a new particle source*. PhD thesis, Technische Universität, 2010.

[152] Claire Pacheco, Quentin Lemasson, Brice Moignard, Laurent Pichon, Marie Radepont, and Didier Gourier. The accelerator under the Louvre the New AGLAE. url:`https://indico.cern.ch/event/594290/`.

[153] Charlotte AJ Palmer, NP Dover, I Pogorelsky, M Babzien, GI Dudnikova, M Ispiriyan, MN Polyanskiy, Jörg Schreiber, P Shkolnikov,

V Yakimenko, et al. Monoenergetic proton beams accelerated by a radiation pressure driven shock. *Physical review letters*, 106(1):014801, 2011.

[154] Matteo Passoni, Luca Fedeli, and Francesco Mirani. Superintense laser-driven ion beam analysis. *Scientific reports*, 9(1):1–11, 2019.

[155] Matteo Passoni, A Sgattoni, Irene Prencipe, Luca Fedeli, David Dellasega, Lorenzo Cialfi, Il Woo Choi, I Jong Kim, Karol Adam Janulewicz, Hwang Woon Lee, et al. Toward high-energy laser-driven ion beams: Nanostructured double-layer targets. *Physical Review Accelerators and Beams*, 19(6):061301, 2016.

[156] P. Patel, A. Mackinnon, M. Key, T. Cowan, M. Foord, M. Allen, D. Price, H. Ruhl, P. Springer, and R. Stephens. Isochoric Heating of Solid-Density Matter with an Ultrafast Proton Beam. *Physical Review Letters*, 91(12):125004, sep 2003.

[157] Claudio Perego. *Target Normal Sheath Acceleration for Laser-Driven Ion Generation: Advances in Theoretical Modeling*. PhD thesis, Università degli Studi di Milano-Bicocca, 2013.

[158] L. Pichon, T. Calligaro, Q. Lemasson, B. Moignard, and C. Pacheco. Programs for visualization, handling and quantification of PIXE maps at the AGLAE facility. *Nuclear Instruments and Methods in Physics Research Section B: Beam Interactions with Materials and Atoms*, 363:48–54, nov 2015.

[159] Haydn W Powell. *Ion acceleration in ultra-thin foils undergoing relativistically induced transparency*. PhD thesis, University of Strathclyde, 2015.

[160] R Prasad, F Abicht, M Borghesi, J Braenzel, PV Nickles, G Priebe, M Schnürer, and S Ter-Avetisyan. Thomson spectrometer–microchannel plate assembly calibration for MeV-range positive and negative ions, and neutral atoms. *Review of Scientific Instruments*, 84(5):053302, 2013.

[161] Michael A Purvis, Vyacheslav N Shlyaptsev, Reed Hollinger, Clayton Bargsten, Alexander Pukhov, Amy Prieto, Yong Wang, Bradley M Luther, Liang Yin, Shoujun Wang, et al. Relativistic plasma nanophotonics for ultrahigh energy density physics. *Nature Photonics*, 7(10):796, 2013.

[162] B Qiao, M Zepf, M Borghesi, and M Geissler. Stable GeV ion-beam acceleration from thin foils by circularly polarized laser pulses. *Physical review letters*, 102(14):145002, 2009.

[163] M. Radepont, Q. Lemasson, L. Pichon, B. Moignard, and C. Pacheco. Towards a sharpest interpretation of analytical results by assessing the uncertainty of PIXE/RBS data at the AGLAE facility. *Measurement*, 114:501–507, jan 2018.

[164] Alessandro Re, Debora Angelici, Alessandro Lo Giudice, Jacopo Corsi, Silvia Allegretti, Alessia Fabiola Biondi, Gianluca Gariani, Silvia Calusi, Nicla Gelli, Lorenzo Giuntini, Mirko Massi, Francesco Taccetti, Leonardo La Torre, Valentino Rigato, and Giovanni Pratesi. Ion Beam Analysis for the provenance attribution of lapis lazuli used in glyptic art: The case of the "Collezione Medicea". *Nuclear Instruments and Methods in Physics Research Section B: Beam Interactions with Materials and Atoms*, 348:278–284, apr 2015.

[165] Martin Reiser and Patrick O'Shea. *Theory and design of charged particle beams*, volume 312. Wiley Online Library, 1994.

[166] MJ Rhee, RF Schneider, and DJ Weidman. Simple time-resolving Thomson spectrometer. *Review of scientific instruments*, 58(2):240–244, 1987.

[167] APL Robinson, Paul Gibbon, M Zepf, S Kar, RG Evans, and C Bellei. Relativistically correct hole-boring and ion acceleration by circularly polarized laser pulses. *Plasma Physics and Controlled Fusion*, 51(2):024004, 2009.

[168] Lorenzo Romagnani, Julien Fuchs, M Borghesi, Patrizio Antici, P Audebert, F Ceccherini, T Cowan, T Grismayer, S Kar, A Macchi, et al. Dynamics of electric fields driving the laser acceleration of multi-MeV protons. *Physical review letters*, 95(19):195001, 2005.

[169] F. Romano, F. Schillaci, G.A.P. Cirrone, G. Cuttone, V. Scuderi, L. Allegra, A. Amato, A. Amico, G. Candiano, G. De Luca, G. Gallo, S. Giordanengo, L. Fanola Guarachi, G. Korn, G. Larosa, R. Leanza, R. Manna, V. Marchese, F. Marchetto, D. Margarone, G. Milluzzo, G. Petringa, J. Pipek, S. Pulvirenti, D. Rizzo, R. Sacchi, S. Salamone, M. Sedita, and A. Vignati. The ELIMED transport and dosimetry beamline for laser-driven ion beams. *Nuclear Instruments and Methods*

in Physics Research Section A: Accelerators, Spectrometers, Detectors and Associated Equipment, 829:153–158, sep 2016.

[170] Luis Roso. High repetition rate Petawatt lasers. *EPJ Web of Conferences*, 167:01001, jan 2018.

[171] M Roth, E Brambrink, P Audebert, A Blazevic, R Clarke, J Cobble, TE Cowan, J Fernandez, J Fuchs, M Geissel, et al. Laser accelerated ions and electron transport in ultra-intense laser matter interaction. *Laser and Particle Beams*, 23(1):95, 2005.

[172] M Roth, TE Cowan, MH Key, SP Hatchett, C Brown, W Fountain, J Johnson, DM Pennington, RA Snavely, SC Wilks, et al. Fast ignition by intense laser-accelerated proton beams. *Physical Review Letters*, 86(3):436, 2001.

[173] Hellen Cristine Santos, Claudia Caliri, Lighea Pappalardo, Roberto Catalano, Andrea Orlando, Francesca Rizzo, and Francesco Paolo Romano. Identification of forgeries in historical enamels by combining the non-destructive scanning XRF imaging and alpha-PIXE portable techniques. *Microchemical Journal*, 124:241–246, jan 2016.

[174] M. Schollmeier, S. Becker, M. Geißel, K. A. Flippo, A. Blažević, S. A. Gaillard, D. C. Gautier, F. Grüner, K. Harres, M. Kimmel, F. Nürnberg, P. Rambo, U. Schramm, J. Schreiber, J. Schütrumpf, J. Schwarz, N. A. Tahir, B. Atherton, D. Habs, B. M. Hegelich, and M. Roth. Controlled Transport and Focusing of Laser-Accelerated Protons with Miniature Magnetic Devices. *Physical Review Letters*, 101(5):055004, aug 2008.

[175] Jörg Schreiber. *Ion acceleration driven by high-intensity laser pulses.* PhD thesis, lmu, 2006.

[176] Jörg Schreiber, PR Bolton, and K Parodi. Invited Review Article:"Hands-on" laser-driven ion acceleration: A primer for laser-driven source development and potential applications. *Review of Scientific Instruments*, 87(7):071101, 2016.

[177] Jörg Schreiber, Malte Kaluza, F Grüner, U Schramm, BM Hegelich, J Cobble, Michael Geissler, E Brambrink, J Fuchs, P Audebert, et al. Source-size measurements and charge distributions of ions accelerated from thin foils irradiated by high-intensity laser pulses. *Applied Physics B*, 79(8):1041–1045, 2004.

[178] Manfred Schreiner, Michael Melcher, and Katharina Uhlir. Scanning electron microscopy and energy dispersive analysis: applications in the field of cultural heritage. *Analytical and Bioanalytical Chemistry*, 387(3):737–747, jan 2007.

[179] M. Scisciò, M. Migliorati, L. Palumbo, and P. Antici. Design and optimization of a compact laser-driven proton beamline. *Scientific Reports*, 8(1):6299, dec 2018.

[180] Massimiliano Scisciò. *Study and implementation of beam lines and devices for the acceleration, transport and manipulation of laser-accelerated particle beams*. PhD thesis, University of Rome, Sapienza; Université du Québec, Institut national de la recherche scientifique., 2017.

[181] V. Scuderi, S. Bijan Jia, M. Carpinelli, G.A.P. Cirrone, G. Cuttone, G. Korn, T. Licciardello, M. Maggiore, D. Margarone, P. Pisciotta, F. Romano, F. Schillaci, C. Stancampiano, and A. Tramontana. Development of an energy selector system for laser-driven proton beam applications. *Nuclear Instruments and Methods in Physics Research Section A: Accelerators, Spectrometers, Detectors and Associated Equipment*, 740:87–93, mar 2014.

[182] V Scuderi, G Milluzzo, D Doria, A Alejo, AG Amico, N Booth, G Cuttone, JS Green, S Kar, G Korn, et al. TOF diagnosis of laser accelerated, high-energy protons. *Nuclear Instruments and Methods in Physics Research Section A: Accelerators, Spectrometers, Detectors and Associated Equipment*, 978:164364, 2020.

[183] A Sharma, Z Tibai, J Hebling, and JA Fülöp. Quasi-monoenergetic proton acceleration from cryogenic hydrogen microjet by ultrashort ultraintense laser pulses. *Physics of Plasmas*, 25(3):033111, 2018.

[184] Ashutosh Sharma. High Energy electron and proton acceleration by circularly polarized laser pulse from near critical density hydrogen gas target. *Scientific Reports*, 8(1):2191, dec 2018.

[185] Ashutosh Sharma and Alexander Andreev. Effective laser driven proton acceleration from near critical density hydrogen plasma. *Laser and Particle Beams*, 34(2):219–229, 2016.

[186] Luís O Silva, Michael Marti, Jonathan R Davies, Ricardo A Fonseca, Chuang Ren, Frank S Tsung, and Warren B Mori. Proton

shock acceleration in laser-plasma interactions. *Physical Review Letters*, 92(1):015002, 2004.

[187] Prashant Kumar Singh, KF Kakolee, Tae Won Jeong, and Sargis Ter-Avetisyan. A diagnostic for micrometer sensitive positioning of solid targets in intense laser-matter interaction. *Nuclear Instruments and Methods in Physics Research Section A: Accelerators, Spectrometers, Detectors and Associated Equipment*, 829:363–366, 2016.

[188] RA Snavely, MH Key, SP Hatchett, TE Cowan, Markus Roth, TW Phillips, MA Stoyer, EA Henry, TC Sangster, MS Singh, et al. Intense high-energy proton beams from petawatt-laser irradiation of solids. *Physical review letters*, 85(14):2945, 2000.

[189] S. Sorieul, Ph. Alfaurt, L. Daudin, L. Serani, and Ph. Moretto. AIFIRA: An ion beam facility for multidisciplinary research. *Nuclear Instruments and Methods in Physics Research Section B: Beam Interactions with Materials and Atoms*, 332:68–73, aug 2014.

[190] Tomas Stanislauskas, Rimantas Budriūnas, Gediminas Veitas, Darius Gadonas, Jonas Adamonis, Aidas Aleknavičius, Gžegož Masian, Zenonas Kuprionis, Dominik Hoff, Gerhard G Paulus, et al. Performance tests of the 5 TW, 1 kHz, passively CEP-stabilized ELI-ALPS SYLOS few-cycle laser system (Conference Presentation). In *High-Power, High-Energy, and High-Intensity Laser Technology III*, volume 10238, page 102380S. International Society for Optics and Photonics, 2017.

[191] Donna Strickland and Gerard Mourou. Compression of amplified chirped optical pulses. *Optics communications*, 55(6):447–449, 1985.

[192] HA Sumeruk, S Kneip, DR Symes, IV Churina, AV Belolipetski, Gilliss Dyer, J Landry, G Bansal, A Bernstein, Thomas D Donnelly, et al. Hot electron and X-ray production from intense laser irradiation of wavelength-scale polystyrene spheres. *Physics of plasmas*, 14(6):062704, 2007.

[193] T Tajima and G Mourou. Zettawatt-exawatt lasers and their applications in ultrastrong-field physics. *Physical Review Special Topics-Accelerators and Beams*, 5(3):031301, 2002.

[194] J Teng, SK He, ZG Deng, B Zhang, W Hong, ZM Zhang, B Zhu, and YQ Gu. A compact high resolution Thomson parabola spectrometer

based on Halbach dipole magnets. *Nuclear Instruments and Methods in Physics Research Section A: Accelerators, Spectrometers, Detectors and Associated Equipment*, 935:30–34, 2019.

[195] S Ter-Avetisyan, L Romagnani, M Borghesi, M Schnürer, and PV Nickles. Ion diagnostics for laser plasma experiments. *Nuclear Instruments and Methods in Physics Research Section A: Accelerators, Spectrometers, Detectors and Associated Equipment*, 623(2):709–711, 2010.

[196] S Ter-Avetisyan, M Schnürer, PV Nickles, W Sandner, T Nakamura, and K Mima. Correlation of spectral, spatial, and angular characteristics of an ultrashort laser driven proton source. *Physics of Plasmas*, 16(4):043108, 2009.

[197] S. Ter-Avetisyan, M. Schnürer, R. Polster, P.V. Nickles, and W. Sandner. First demonstration of collimation and monochromatisation of a laser accelerated proton burst. *Laser and Particle Beams*, 26(4):637–642, dec 2008.

[198] Joseph John Thomson. XXVI. Rays of positive electricity. *The London, Edinburgh, and Dublin Philosophical Magazine and Journal of Science*, 21(122):225–249, 1911.

[199] Toma Toncian, Marco Borghesi, Julien Fuchs, Emmanuel d'Humières, Patrizio Antici, Patrick Audebert, Erik Brambrink, Carlo Alberto Cecchetti, Ariane Pipahl, Lorenzo Romagnani, et al. Ultrafast laser-driven microlens to focus and energy-select mega-electron volt protons. *Science*, 312(5772):410–413, 2006.

[200] L Torrisi and G Costa. Compact Thomson parabola spectrometer for fast diagnostics of different intensity laser-generated plasmas. *Physical Review Accelerators and Beams*, 22(4):042902, 2019.

[201] L Torrisi, M Cutroneo, L Andò, and J Ullschmied. Thomson parabola spectrometry for gold laser-generated plasmas. *Physics of Plasmas*, 20(2):023106, 2013.

[202] Sz Toth, T Stanislauskas, I Balciunas, R Budriunas, J Adamonis, R Danilevicius, K Viskontas, D Lengvinas, G Veitas, D Gadonas, et al. SYLOS lasers–the frontier of few-cycle, multi-TW, kHz lasers for ultrafast applications at extreme light infrastructure attosecond light pulse source. *Journal of Physics: Photonics*, 2(4):045003, 2020.

[203] Olivier Tresca. *Optimisation and control of high intensity laser accelerated ion beams*. PhD thesis, University of Strathclyde, 2012.

[204] Pilar Puyuelo Valdes. *Laser-driven ion acceleration with high-density gas-jet targets and application to elemental analysis.* PhD thesis, Université de Bordeaux; Institut national de la recherche scientifique (Québec,province), 2020.

[205] Simon Vallières, Antonia Morabito, Simona Veltri, Massimiliano Scisciò, Marianna Barberio, and Patrizio Antici. Laser-driven proton acceleration with nanostructured targets. In *Laser Acceleration of Electrons, Protons, and Ions IV*, volume 10240, page 1024009. International Society for Optics and Photonics, 2017.

[206] Simon Vallières, Pilar Puyuelo Valdés, Martina Salvadori, Charles Bienvenue, Stéphane Payeur, Emmanuel D'Humières, and Patrizio Antici. The laser-driven ion acceleration beamline on the ALLS 200 TW for testing nanowire targets. In Eric Esarey, Carl B. Schroeder, and Jörg Schreiber, editors, *Laser Acceleration of Electrons, Protons, and Ions V*, page 2. SPIE, apr 2019.

[207] Jeroen A Van Bokhoven and Carlo Lamberti. *X-ray absorption and X-ray emission spectroscopy: theory and applications*, volume 1. John Wiley & Sons, 2016.

[208] Simona Veltri. *Nano materials and innovative laser-based accelerators for cultural heritage*. PhD thesis, UNICAL 'Università della Calabria, Arcavacata di Rende, Italy; Université du Québec, Institut national de la recherche scientifique., 2017.

[209] F Wagner, O Deppert, C Brabetz, P Fiala, A Kleinschmidt, P Poth, VA Schanz, A Tebartz, B Zielbauer, M Roth, et al. Maximum proton energy above 85 MeV from the relativistic interaction of laser pulses with micrometer thick CH_2 targets. *Physical review letters*, 116(20):205002, 2016.

[210] AVT Manta website. AVT Manta. url:`https://www.1stvision.com/cameras/models/Allied-Vision/Manta$%$20G-146$%$20B/C`.

[211] CERN website. The Large Hadron Collider (LHC). url:`https://home.cern/science/accelerators/large-hadron-collider`.

[212] ELI-ALPS website. Extreme Light infrastructure Attosecond Light Pulse Source (ELI-ALPS). url:`https://www.eli-alps.hu/`.

[213] Photonis website. Microchanel plates. url:`https://www.photonis.com/products/microchannel-plates`.

[214] Helmut Wiedemann et al. *Particle accelerator physics*, volume 314. Springer Berlin, 2007.

[215] Wikipedia. Chirped Pulse Amplification (CPA) — Wikipedia, the free encyclopedia, 2021. `https://en.wikipedia.org/wiki/Chirped_pulse_amplification`.

[216] S. C. Wilks, W. L. Kruer, M. Tabak, and A. B. Langdon. Absorption of ultra-intense laser pulses. *Physical Review Letters*, 69(9):1383–1386, Aug 1992.

[217] Scott C Wilks and William L Kruer. Absorption of ultrashort, ultra-intense laser light by solids and overdense plasmas. *IEEE Journal of Quantum Electronics*, 33(11):1954–1968, 1997.

[218] O Willi, T Toncian, M Borghesi, J Fuchs, E D'humieres, P Antici, P Audebert, E Brambrink, C Cecchetti, A Pipahl, et al. Laser triggered micro-lens for focusing and energy selection of MeV protons. *Laser and Particle Beams*, 25(1):71–77, 2007.

[219] L Yin, BJ Albright, KJ Bowers, D Jung, JC Fernández, and BM Hegelich. Three-dimensional dynamics of breakout afterburner ion acceleration using high-contrast short-pulse laser and nanoscale targets. *Physical review letters*, 107(4):045003, 2011.

[220] Tae Jun Yu, Seong Ku Lee, Jae Hee Sung, Jin Woo Yoon, Tae Moon Jeong, and Jongmin Lee. Generation of high-contrast, 30 fs, 1.5 PW laser pulses from chirped-pulse amplification Ti:Sapphire laser. *Optics express*, 20(10):10807–10815, 2012.

[221] Karl Zeil. Laser Plasma Summer School (LaPlaSS) "Diagnostic techniques for laser-plasma experiments @ HRR", Salamanca (Spain): Charge particle diagnostics in high power laser driven plasmas, 2018. `https://www.laserlab-europe.eu/events-1/laserlab-events/2018/LaPlass`.

[222] ML Zhou, XQ Yan, G Mourou, JA Wheeler, JH Bin, J Schreiber, and T Tajima. Proton acceleration by single-cycle laser pulses offers a novel monoenergetic and stable operating regime. *Physics of Plasmas*, 23(4):043112, 2016.

[223] JF Ziegler. SRIM software 2013. url:`http://www.srim.org`.

[224] Alessandro Zucchiatti and Fernando Agulló-Lopez. Potential consequences of ion beam analysis on objects from our cultural heritage: an appraisal. *Nuclear Instruments and Methods in Physics Research Section B: Beam Interactions with Materials and Atoms*, 278:106–114, 2012.

[225] Alessandro Zucchiatti and Andrés Redondo-Cubero. Ion beam analysis: New trends and challenges. *Nuclear Instruments and Methods in Physics Research, Section B: Beam Interactions with Materials and Atoms*, 331:48–54, 2014.